PONTIFÍCIA UNIVERSIDADE CATÓLICA
DO RIO DE JANEIRO

Matheus Silva de Menezes

Ferrocene-derived *N*-acylhydrazonic ligands as metallophores and electrochemical probes in the context of Alzheimer's disease

Dissertação de Mestrado

Dissertation presented to the *Programa de Pós-Graduação em Química* of PUC-Rio in partial fulfilment of the requirements for the degree of *Mestre em Química*.

Advisor: Prof. Dr. Nicolás A. Rey

Rio de Janeiro
August 2024

PONTIFÍCIA UNIVERSIDADE CATÓLICA
DO RIO DE JANEIRO

Matheus Silva de Menezes

Ferrocene-derived *N*-acylhydrazonic ligands as metallophores and electrochemical probes in the context of Alzheimer's disease

Dissertation presented to the *Programa de Pós-Graduação em Química* of PUC-Rio in partial fulfilment of the requirements for the degree of *Mestre em Química*. Approved by the Examination Committee:

Prof. Dr. Nicolás A. Rey
Advisor
Departamento de Química – PUC-Rio

Prof. Dr. Ana Cecilia González Baró
Universidad Nacional de La Plata

Prof. Dr. Maurício Lanznaster
Universidade Federal Fluminense

Prof. Dr. Renan Lira de Farias
Departamento de Química – PUC-Rio

Rio de Janeiro, August 28th, 2024

Matheus Silva de Menezes

Graduated in Chemistry at the Universidade Federal Rural do Rio de Janeiro (UFRRJ) in 2021. Received CAPES scholarship from 2023 to 2024.

Bibliographic data

Menezes, Matheus Silva de

Ferrocene-derived *N*-acylhydrazonic ligands as metallophores and electrochemical probes in the context of Alzheimer's disease / Matheus Silva de Menezes ; advisor: Nicolás A. Rey. – 2024.
148 f. : il. color. ; 30 cm

Dissertação (mestrado)–Pontifícia Universidade Católica do Rio de Janeiro, Departamento de Química, 2024.
Inclui bibliografia

1. Química – Teses. 2. Metalóforos. 3. Sonda eletroquímica. 4. Alzheimer. 5. N-acil-hidrazonas. I. Rey, Nicolás A. II. Pontifícia Universidade Católica do Rio de Janeiro. Departamento de Química. III. Título.

CDD: 540

Acknowledgements

Gostaria de expressar minha sincera gratidão ao professor Dr. Nicolás A. Rey que, antes de sua constante orientação, me aceitou como aluno do LABSO-Bio e me deu a chance de conhecer meu caminho e de mostrar do que posso ser capaz.

Gostaria de agradecer à PUC-Rio, o Departamento de Química, e todos os professores que me lecionaram, assistiram ou apoiaram. O presente trabalho foi realizado com apoio da Coordenação de Aperfeiçoamento de Pessoal de Nível Superior - Brasil (CAPES) - Código de Financiamento 001. Agradeço também às agências de fomento CNPq e FAPERJ pelo apoio à pesquisa e financiamento à ciência. Meus agradecimentos à Central Analítica "Pe. Leopoldo Hainberger" do departamento de Química da PUC-Rio pelo acesso a diversos equipamentos essenciais neste trabalho. Obrigado à Profa. Renata Diniz pelas análises de DRX realizadas. Obrigado, ainda, à banca avaliadora, composta pela profa. Ana Cecilia, prof. Maurício Lanznaster e prof. Renan Lira, pelo aceite de avaliação e contribuição no presente trabalho.

Agradeço profundamente às minhas armas secretas durante o mestrado: Daphne Cukierman, Barbara Marinho e Fagner Moura, obrigado pelas discussões, desafios, ajuda e amizade.

Um agradecimento especial a Eduardo Lucas, Fábio Filho, Frederico Viviés, e Samantha Marques, vocês foram mais que um abrigo, mostraram o mais puro significado da amizade nesse período.

Minha eterna gratidão para minha mãe, Cristina Angélica, que me fez enxergar o que significa "amor incondicional". Me reaproximar de você foi um dos grandes frutos dessa jornada. Agradeço ainda, ao meu pai, Kilimandjaro Filho, por

ter, sempre de bom grado, custeado minha educação, até meu ingresso no ensino médio.

Ao meu irmão, Leonardo Baêta, pelas mágicas palavras de encorajamento e sabedoria que fizeram desse momento o menos tribuloso possível. A Vitória Pina, por estar ao meu lado em todos os momentos mais difíceis, obrigado pela sua dedicação e amizade. A Isabel Peres e Luiz Paulo, por terem me ajudado e abrigado quando eu mais precisava e à Yasmin Peres, pelo acolhimento fraterno.

A Ana Paula Leite, por sua caridade e paciência, obrigado por ser meu cantil na travessia do deserto seco e árido. A Leonardo Rezende, obrigado pelo financiamento integral do notebook que eu uso para trabalhar e que escrevi por inteiro essa dissertação. A Giulia Romancini, por toda ajuda e paciência como minha IC neste último semestre turbulento.

Aos meus amigos de longa-data e aos mais recentes: Maurício Mancini, Gabriela Sales, Lorenna e Lohanna Antunes, Lucas Machado, Bernardo Almeida, Wylmar e Yago Perezynski, Sam Bernal, Cindy Cruz. Vocês são as estrelas do meu céu.

Aos meus demais amigos que tive o enorme prazer de conhecer durante este período: Boris Leon, Beatriz Bastos, Henrique Hollauer, Carol Stellet, Roberta Lamosa, Daniele Cabral, Ygor Sobrinho, Anna Julia e Elisa Tardem. A ajuda e companhia de vocês foi indispensável. Todos vocês tornaram essa jornada mais fácil.

Definitivamente não sou hoje a mesma pessoa de dois anos atrás e todos vocês têm uma parte nisso. Vocês merecem uma parte dos louros deste trabalho, obrigado por serem minhas pedras angulares, minhas pilastras e sustentações.

"O verdadeiro mestrado são os amigos que
fizemos e mantivemos pelo caminho"

Muito obrigado a todos!

Abstract

Menezes, Matheus Silva de; Rey, Nicolás Adrián (Advisor). **Ferrocene-derived *N*-acylhydrazonic ligands as metallophores and electrochemical probes in the context of Alzheimer's disease.** Rio de Janeiro, 2024. 148p. Dissertação de Mestrado - Departamento de Química, Pontifícia Universidade Católica do Rio de Janeiro.

Alzheimer's Disease (AD) is the leading cause of dementia, with around 50 million patients worldwide in 2020, and this number is projected to triple by 2050, with an estimated cost of US$1 trillion annually. Biometals such as copper and zinc in their ionic forms can interact with the disease-related β-amyloid peptide (Aβ), making it more susceptible to aggregation, in addition to contributing to increased oxidative stress in the body. In this context, ligands known as metallophores have been developed to sequester metal ions bound to the peptide in order to reduce Aβ oligomerization and/or metal-induced oxidative stress. Instead of binding and systematically removing any metals from tissues, metallophores aim to act by restoring physiological metal homeostasis through specific binding with copper and/or zinc, attenuating their abnormal interactions with the peptide. In this scenario, two *N*-acylhydrazone ligands, with an electroactive fraction containing ferrocene, named **Feizone** and **Ferfurone,** were synthesized and characterized using techniques such as FTIR, ^{1}H NMR, TGA, UV-Vis, and XRD. The complexation of these ligands towards Cu^{2+} and Zn^{2+}, as well as their amide deprotonation, were studied by cyclic voltammetry. The hydrolytic and photolytic stabilities were also assessed through electronic spectroscopy. Their radical scavenging potential was studied towards electrochemically generated superoxide ions and their suitability as electrochemical probes was estimated through interaction with the $A\beta_{1-40}$ peptide by square-wave voltammetry. Both ligands demonstrated satisfactory stability compared to other molecules of the same class, also showing radical scavenging potential with statistically significant differences in the anodic waves of superoxide species. Additionally, experiments involving the full-length $A\beta_{1-40}$ showed current changes in the voltammogram, suggesting their interaction with this peptide. Since plaques formed by Aβ are one of the main hallmarks of AD, these ligands show potential as electrochemical probes in the context of the disease.

Keywords:

metallophores, electrochemical probe, Alzheimer, *N*-acylhydrazones

Resumo

Menezes, Matheus Silva de; Rey, Nicolás Adrián (Advisor). **Ligantes *N*-acil-hidrazônicos derivados do ferroceno como metalóforos e sondas eletroquímicas no contexto da doença de Alzheimer.** Rio de Janeiro, 2024. 148p. Dissertação de Mestrado - Departamento de Química, Pontifícia Universidade Católica do Rio de Janeiro.

A Doença de Alzheimer (DA) é a maior causa de demência, com cerca de 50 milhões de pacientes em todo mundo em 2020, e este número é projetado para triplicar até 2050, com o custo estimado de US$1 trilhão anualmente. Biometais como cobre e zinco em sua forma iônica são capazes de interagir com o peptídeo β-amiloide (Aβ), relacionado à doença, deixando-o mais suscetível a agregação, além de contribuírem para o aumento do estresse oxidativo no organismo.

A perturbação na homeostase metálica no cérebro, especialmente de cobre e zinco, aumenta o estresse oxidativo no cérebro, gerando espécies reativas de oxigênio (ERO) e nitrogênio (ERN) principalmente através de reações de Fenton e Haber-Weiss. Adicionalmente, cobre e zinco aceleram a agregação de Aβ ao se ligarem em certos resíduos deste peptídeo.

Neste contexto, ligantes conhecidos como metalóforos vêm sido desenvolvidos com objetivo de sequestrar os íons metálicos ligados ao peptídeo ou proteína na finalidade de reduzir os oligômeros de Aβ e/ou estresse oxidativo induzido por metais. Invés de ligar e sistematicamente remover quaisquer metais dos tecidos, os metalóforos agem a fim de restaurar a homeostase metálica fisiológica através da ligação específica com cobre e/ou zinco, atenuando suas interações anormais com o peptídeo, assim prevenindo a oligomerização.

Neste sentido, dois ligantes *N*-acil-hidrazônicos, com fração eletroativa contendo ferroceno, denominados **Feizona** e **Ferfurona**, foram sintetizados e caracterizados com técnicas como FTIR, ^{1}H NMR, TGA, UV-Vis e XRD. A complexação desses ligantes com Cu^{2+} e Zn^{2+}, bem como sua desprotonação amídica, foram estudadas por voltametria cíclica. Estes ligantes apresentaram capacidade satisfatória em coordenar íons de Cu^{2+} em solução em temperatura ambiente, porém necessitam de um meio fortemente básico para coordenarem espécies de Zn^{2+}. Esta característica indica uma seletividade para íons de Cu^{2+} em meio fisiológico.

Estudos de estabilidade hidrolítica foram avaliados por espectroscopia eletrônica, mostrando excelente estabilidade configurada pela conjugação eletrônica na estrutura dos compostos. Adicionalmente, a estabilidade fotolítica também foi avaliada por diferentes técnicas, mostrando-se dependente do solvente.

O estudo de complexação por voltametria cíclica destes ligantes comprova a dependência de um meio básico para coordenação efetiva de zinco, apresentando perfis sigmoidais duplos para ambos os metais, apontando para diferentes possibilidades na estequiometria de formação destes complexos.

Parâmetros farmacológicos calculados foram avaliados utilizando ferramentas disponíveis, apresentando bons resultados teóricos para atravessar barreiras biológicas. As propriedades de potencial eliminação de radicais foram estudadas com radicais superóxidos gerados eletroquimicamente, mostrando eliminação destes radicais com diferenças estatisticamente significativas nas ondas anódicas das espécies de superóxido estudadas.

A interação destes ligantes com o peptídeo $A\beta_{1-40}$ foi estimado através de experimentos por voltametria de onda quadrada, mostrando mudanças na corrente do voltamograma, sugerindo uma interação com este peptídeo. O comportamento assintótico da variação de corrente ao longo da adição do peptídeo $A\beta_{1-40}$ indica a saturação na interação dos ligantes com o peptídeo. Como as placas de Aβ constitui um dos mais importantes marcadores da DA, os sinais eletroquímicos gerados a partir da interação dos ligantes com este marcador demostra o potencial destes compostos como sondas eletroquímicas no contexto dessa doença.

Palavras chave:

metalóforos, sonda eletroquímica, Alzheimer, *N*-acil-hidrazonas

Table of Contents

List of Acronyms and Abbreviations

1D	One-dimension
^{1}H NMR	Hydrogen-1 Nuclear Magnetic Resonance
AD	Alzheimer's Disease
AICD	Amyloid precursor protein intracelullar domain
AMPA	α-amino-3-hydroxy-5-methyl-4-isoxazolepropionic acid
APP	Amyloid precursor protein
APPsα	Soluble amyloid precursor protein-alpha
APPsβ	Soluble amyloid precursor protein-beta
Aβ	Amyloid-beta peptide
BBB	Blood-brain barrier
cLog P	Calculated octanol-water partition coefficient
cLog S	Calculated water solubility
Cp	Ciclopentadienyl
CQ	Clioquinol
CV	Cyclic voltammetry
DMF	*N*,*N*-Dimethylformamide
DMSO	Dimethylsulfoxide
DMSO-d_6	Deuterated dimethylsulfoxide
DNA	Deoxyribonucleic acid
E^0	Standard electric potential
$E_{½}$	Average of couple redox potentials
E_p, E_{peak}	Peak electric potential
E_{pa}	Anodic peak electric potential
E_{pc}	Cathodic peak electric potential
FDA	U.S. Food and Drug Administration
FTIR	Fourier-transform infrared spectroscopy
HEPES	4-(2-hydroxyethyl)-1-piperazineethanesulfonic acid
ICER	Incremental cost-effectiveness ratio
ICP-OES	Inductively coupled plasma optical emission spectroscopy
i_{pa}	Anodic current peak
i_{pc}	Cathodic current peak
i_{peak}	Current peak
k^0	Standard electrochemical rate constant
MeOH	Methanol
MT	Metallothionein
m_T	Rate of mass transport
MW	Molecular weight
NADPH	Nicotinamide adenine dinucleotide phosphate
NMDA	N-methyl-D-Aspartate

NMR	Nuclear Magnetic Resonance
p*K*a	Acid dissociation constant
PP2A	Protein phosphatase 2
QALY	Quality-adjusted life-years
RNS	Radical nitrogen species
ROS	Radical Oxygen species
SHE	Standard hydrogen electrode
SoC	Standard of care
TBAPF6	Tetrabutylammonium hexafluorophosphate
TGA	Thermogravimmetry Analysis
TPSA	Topological polar surface área
TRIS	Tris(hydroxymethyl)aminoomethane
UV-vis	Ultraviolet-visible
XRD	X-ray diffraction
αCTF	Alpha C-terminal fragment
βCTF	Beta C-terminal fragmente
ΔE_{pp}	Electric potential peak-to-peak difference

List of Equations

List of Figures

List of Tables

List of Appendix Figures

List of Appendix Tables

1. Introduction

1.1. Alzheimer's Disease

Alzheimer's Disease (AD) is a neurodegenerative disorder, first described by the German psychiatrist and neuropathologist Alois Alzheimer, who reported the symptoms of memory loss, behavioral and language problems, and paranoia. Also, by *post-mortem* observations, he reported an atrophied brain and neurons with signs of anomalous protein deposition, which were later called neurofibrillary tangles and senile plaques Alzheimer *et al.* (1995).

AD is the most common cause of dementia, with around 50 million patients worldwide in 2020 and this number is projected to triple by 2050, with estimated global costs of US$1 trillion annually (Breijyeh & Karaman, 2020). The principal risk factor for both dementia and AD as a whole is aging, mainly committing the population over 65 years old (Knopman *et al.*, 2021). Although currently there is no cure or effective therapies for AD, there are symptomatic treatments available: inhibitors of cholinesterase and a non-competitive inhibitor of NMDA-receptor, affecting the glutamatergic transmission (Yiannopoulou & Papageorgiou, 2020).

There are positive and negative features of neuropathological changes in the brain of AD bearers. The classical positive lesions consist of abundant extracellular amyloid plaques and intracellular neurofibrillary tangles, neuropil threads, and dystrophic neurites containing hyperphosphorylated tau protein (Serrano-Pozo *et al.*, 2011). Although the presence of these alterations in the brain of healthy elderly people is possible, especially the amyloid plaques, the symptoms are not observed altogether or with the same intensity as in patients afflicted with AD (Smith, 1999). Several negative biochemical signals are observed in AD, for example, widespread oxidative stress in the brain, neuroinflammation, calcium dysregulation, deficit and altered mitochondrial distribution, oligomerization of Aβ peptide, synaptic toxicity, and problems in metal homeostasis (De Falco *et al.*, 2016).

The amyloid plaques are localized, in the AD brain, mainly in the cerebellar tonsils, the hippocampus, and the entorhinal cortex of the temporal lobe, while the parietal and frontal portions of the associative cortex are considerably less affected (Serrano-Pozo *et al.*, 2011).

Different etiological hypotheses for AD have been developed and gradually modified alongside several technological advances.

The cholinergic hypothesis correlates AD with a decrease in the concentration of choline acetyltransferase, the enzyme responsible for acetylcholine synthesis, in the cortex and hippocampus, as well as a reduction in cholinergic neurons localized in the nucleus basalis of Meynert (Davies & Maloney, 1976; Kása *et al.*, 1997). A positive association between these two depletions and the cognitive deficit severity of the patient in life (Kása *et al.*, 1997; Wilcock *et al.*, 1982) was observed. Later studies found that the administration of cholinomimetic substances reduces the mnemonic impairment present in patients with AD (Christie *et al.*, 1981; Drachman & Sahakian, 1980), which explains the subsequent development of drugs to inhibit the cholinesterase enzyme as anti-AD therapies.

The glutamatergic hypothesis' premise is that in specific conditions, such as the alteration in cellular energy metabolism, occurs an excessive activation of Glu NMDA receptors, leading to a possible alteration in calcium homeostasis, raising intracellular concentrations of this metal, capable of starting the neuronal apoptosis process (Danysz *et al.*, 2000; Parsons *et al.*, 2007). Thus, this glutamate-dependent excitotoxicity can constitute one of the pathogenic mechanisms necessary for the maintenance and amplification of the neurodegenerative process (Greenamyre & Young, 1989). This whole activity is key to understand the therapeutic use of a non-competitive NMDA inhibitor for the treatment of AD, as cited before.

All the symptomatic treatments previously mentioned are based solemnly on the cholinergic and the glutamatergic hypotheses that emerged in the '80s (De Falco *et al.*, 2016), and consisted of the only FDA-approved, small molecule-based, drugs for AD until 2020 (Yiannopoulou & Papageorgiou, 2020). Nevertheless, a growing number of preliminary studies on treatments for symptoms, such as cognitive enhancers and medications for alleviating behavioral and psychological symptoms of dementia, are being carried out (Huang *et al.*, 2023).

More recently, the FDA has approved Aducanumab and Lecanemab (Dhillon, 2021; Vitek *et al.*, 2023), both monoclonal antibodies, either human or humanized, that exhibit strong binding to Aβ, facilitating the removal of both soluble and insoluble Aβ through Fc receptor-mediated phagocytosis (Chowdhury, 2023).

However, many clinical trials mostly resulted in negative outcomes, unable to show significant effects in patients with clinically evident or prodromal dementia (Chowdhury, 2023). Additionally, these treatments are tremendously costly (over US$26,500 per year), surpassing the standard of care (SoC), presenting an estimated incremental cost-effectiveness ratio (ICER) per quality adjusted life year (QALY) of US$185,822.92 (Haile & Lee, 2024).

The amyloid cascade is a more recent approach to the matter, along with some conjectures that can be considered extensions of this hypothesis: the oligomeric and metal hypothesis. These etiological hypotheses are more prone to explain the formation of the principal positive lesion observed in the AD brain: the senile plaques. Each hypothesis will be further discussed in the following paragraphs.

The first work about the amyloid cascade hypothesis was published in the ’90s and postulates that the Aβ peptide and/or the products of its precursor protein, an integral glycoprotein named amyloid precursor protein (APP), are neurotoxic and can lead to the formation of the senile plaques, resulting in neuronal death (Hardy & Higgins, 1992). The successive cleavage of APP by α-secretase leads to the formation of APPsα and αCTF, which is then cleaved by γ-secretase to yield the p3 peptide and AICD fragment (Thinakaran & Koo, 2008). On the other hand, the cleavage of APP by β-secretases and γ-secretases, leading to the production of Aβ, which is secreted into the extracellular space in the form of monomers, is known as the amyloidogenic pathway (Holtzman *et al.*, 2011). In this mechanisms, APP is first cleaved into APPsβ and βCTF, subsequently cleaved by γ-secretase into AICD and the amyloid peptide Aβ (Thinakaran & Koo, 2008). These pathways for APP cleavage and Aβ secretion are illustrated in Figure 1.

The γ-secretase enzyme can cleave the APP in different regions, leading to several Aβ fragments, mainly $A\beta_{1-40}$ and $A\beta_{1-42}$, with 40 and 42 amino acid residues, respectively (Soreghan *et al.*, 1994). Although both fragments are capable of aggregation, $A\beta_{1-42}$ aggregates more rapidly, hence its more hydrophobic nature, configured by its C-terminal alanine and isoleucine residues, therefore forming stable oligomers earlier. The enhanced production of the $A\beta_{1-42}$ results in an increase in the $A\beta_{1-42}/A\beta_{1-40}$ ratio, starting the initial microscopic deposition of $A\beta_{1-42}$ in the form of early plaques in AD brains (Haass & Selkoe, 2007).

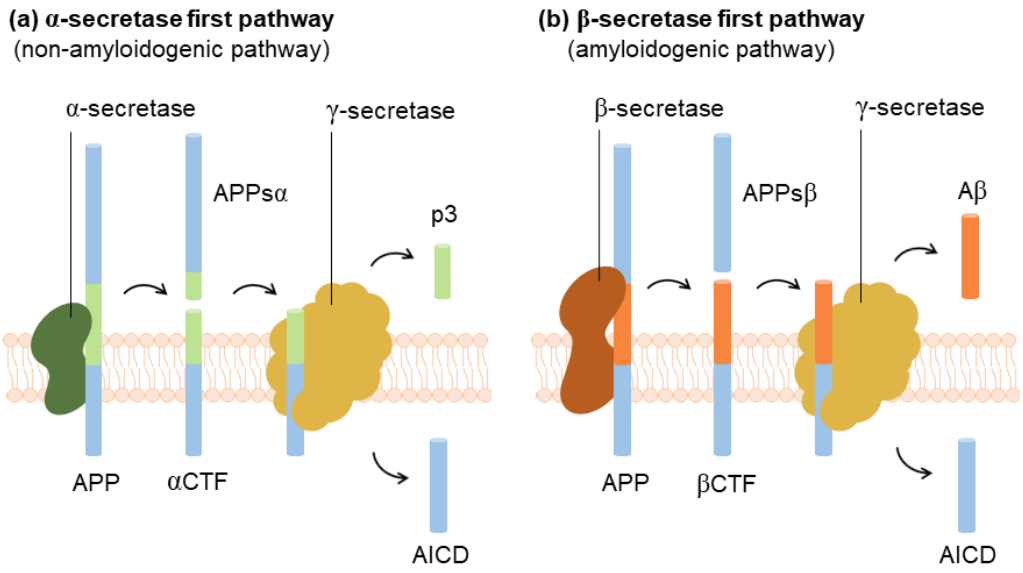

Figure 1. Non-amyloidogenic (a) and amyloidogenic (b) APP cleavage pathways. Adapted from Knopman *et al.* (2021).

A study published in 1998 showed that Aβ immediately damages the neural synapses when forced to maintain its oligomeric form, leading to cellular death, even though the same does not occur with Aβ fibrils (Lambert *et al.*, 1998). This is base for the oligomeric hypothesis, with several studies showing evidence that the oligomer form better explains the Aβ neurotoxicity either *in vitro* or using animal models (Ferreira & Klein, 2011; Koffie *et al.*, 2011; Puzzo *et al.*, 2008; Selkoe, 2008). Furthermore, other studies show that Aβ oligomers rapidly induct failure in the synaptic plasticity (Bieschke *et al.*, 2011; Walsh *et al.*, 2002). The toxicity of the Aβ peptide is observed especially in its oligomeric form, which is pointed to interact with metabotropic glutamate receptor 5 and NMDA receptors (Benarroch, 2018; Spires-Jones & Hyman, 2014), and also seems to interact with some insulin and α7 nicotinic acetylcholine receptors. Moreover, Aβ also seems to cause pathological changes in dendritic spines and synaptic efficiency (Rice *et al.*, 2019).

The main function of the tau protein is the stabilization of microtubules (Eftekharzadeh *et al.*, 2018; Pooler *et al.*, 2014). It is normally present in the cytoplasm of axons (Gallardo & Holtzman, 2019) and also found associated with the nuclear membrane (Eftekharzadeh *et al.*, 2018; Pooler *et al.*, 2014). Tau may accumulate in a hyperphosphorylated form in cell bodies and dendrites and can be

released into the extracellular space by synaptic activity (Wu *et al.*, 2016; Yamada *et al.*, 2014), being taken up in postsynaptic neurons and glia (de Calignon *et al.*, 2012). As already mentioned, aggregated tau appears intracellular as neurofibrillary tangles, as neuropil threads and dystrophic neurites surrounding Aβ plaques (Braak & Braak, 1991; Delacourte *et al.*, 1999), and these post-translational modifications of tau affect the rate of AD progression (Dujardin *et al.*, 2020). Several studies indicate that aggregation of the Aβ peptide may be the activation event for tau hyperphosphorylation, even though its trigger mechanisms are still not well clarified (Annamalai *et al.*, 2015; Selkoe, 1996; Stancu *et al.*, 2014).

In recent years, the amyloid cascade hypothesis has garnered significant attention, with increasing evidence indicating that endogenous metal ions, particularly those with redox activity like copper(I/II) and iron(II/III), as well as non-redox-active ions such as zinc(II), may play a role in the progression of neurodegenerative diseases by enhancing Aβ aggregation and its toxicity (Hane & Leonenko, 2014; Hane *et al.*, 2013). The 'metal hypothesis' suggests that the problem lies not in toxicological exposure to these metals, but in the failure of the body's regulatory mechanisms. This failure leads to a functional deficit in some cellular compartments as well as to a toxic surplus in others (Sensi *et al.*, 2018). Consequently, this hypothesis presumes that amyloid plaques are not only the cause of the disease but also contribute to the disruption of metal homeostasis at synapses (Adlard *et al.*, 2010; Lee *et al.*, 2002).

1.2 Metals and protein aggregation

Essential endogenous metals encompass chromium, cobalt, copper, iron, lithium, magnesium, manganese, nickel, selenium, and zinc. Typically, these trace metals serve as enzyme cofactors, aiding in the regulation of cellular activities. For instance, elements iron, copper, and zinc are integral to a variety of physiological processes, including electron and oxygen transport, neurotransmitter synthesis, protein modification, redox reactions, immune responses, cell adhesion, and protein / carbohydrate metabolism (Chen *et al.*, 2016).

While transition metals are crucial for animals and plants, they are typically needed only in trace amounts. However, excessive metal levels can accumulate in

various organs, including the brain. High concentrations of metals like copper and zinc are found in cortical tissue and are released in free ionic forms during neural activity (Sensi *et al.*, 2018). Disrupted homeostasis of these metals triggers several harmful intracellular events, including oxidative stress, mitochondrial dysfunction, DNA fragmentation, protein misfolding, endoplasmic reticulum stress, autophagy dysregulation, and apoptosis activation (Chen *et al.*, 2016). These effects can impair neurotransmission and lead to neurodegeneration, resulting in cognitive issues, movement disorders, and learning and memory deficits. In this context, metal-induced neurotoxicity has been linked to several neurological diseases in humans, including AD (Chen *et al.*, 2016).

Zinc exists in the central nervous system in two forms: structural and labile. Structural zinc is tightly bound to proteins and peptides, playing a vital role in proper protein folding and serving as a catalytic or co-catalytic component for numerous enzymes (McCall *et al.*, 2000). On the other hand, labile, or free, zinc is either stored within intracellular organelles or bound to metallothioneins (MTs) and pH-sensitive metal-binding proteins (Maret, 1994). Normally, element's cytosolic concentrations are maintained in the picomolar to low nanomolar range (Outten & O'Halloran, 2001). The release of this free zinc functions as a second messenger in intracellular signaling. However, an increase in zinc levels to the nanomolar range can lead to neurotoxicity (Sensi *et al.*, 2009).

Changes in Zn levels are observed in AD and influence both amyloid-related and unrelated mechanisms which are crucial for the disease's progression (Roberts *et al.*, 2012). Studies of *post-mortem* AD brains have revealed variations in the levels of proteins and transporters that regulate zinc balance (Lyubartseva *et al.*, 2010). These changes are associated with the progression of the disease and the severity of cognitive decline (Whitfield *et al.*, 2014). Research indicates that zinc, which is released at the glutamatergic synapse and is essential for both memory and cognition, has its transporter ZnT3 expressed more abundantly in areas affected by amyloid pathology. In transgenic rats, the absence of ZnT3, which prevents zinc transport in synaptic vesicles, leads to cognitive decline (Cole *et al.*, 1999).

More recent research has shown that Zn may influence tau pathology through a pathway that does not involve phosphorylation (Huang *et al.*, 2014). In this pathway, the metal directly binds to the tau protein, promoting its aggregation.

Additionally, increases in both intra- and extra-neuronal zinc levels can lead to abnormal tau phosphorylation by inhibiting protein-phosphatase 2A (PP2A) (Sun *et al.*, 2012) and activating kinases that phosphorylate tau (Boom *et al.*, 2009; Kim *et al.*, 2011). These mechanisms result in a net increase in phospho-tau adducts, which can worsen tau pathology in Alzheimer's disease (Sensi *et al.*, 2018).

Copper is an essential transition metal that serves as a catalyst in numerous biological processes (Gaggelli *et al.*, 2006). Absorption, distribution, and storage of Cu in mammals are carefully regulated, and any disruption in these processes can be the cause of significant harmful effects (Uauy *et al.*, 1998). Imbalances in dietary or acquired copper can lead to severe neurological issues, with the liver playing a crucial role in maintaining Cu balance. The proper management of this bioelement involves two types of proteins: cuproenzymes, which use Cu as a cofactor, and Cu trafficking proteins, which transport the metal (Sensi *et al.*, 2018).

The neurobiological role of Cu is intricate. When cells accumulate an excess of it, the metal builds up in mitochondria (Beers *et al.*, 1997), which contributes to neurodegenerative processes and apoptotic signaling (Kalita *et al.*, 2018; Swerdlow, 2009). Elevated copper levels have also been detected in lysosomes, which are key organelles in autophagy (Kalita *et al.*, 2018). In AD, the impairment of autophagy and lysosome pathways leads to the harmful accumulation of Aβ and tau aggregates (Orr & Oddo, 2013). Additionally, copper is involved in glial apoptosis, and its dysregulation at synapses causes memory and learning impairments (Kalita *et al.*, 2018). Cu affects synaptic functions by being released from Cu-containing vesicles at excitatory synapses (Dodani *et al.*, 2014). Once released, the metal acts as a high-affinity blocker of the NMDA receptor, influencing its functions and the activity of the glutamatergic AMPA receptor, which significantly inhibits glutamate-mediated neurotransmission (Dodani *et al.*, 2014).

Beyond its catalytic roles, copper participates in redox cycles (Cu^{2+}/Cu^{+}), increasing oxidative stress in the brain by generating reactive oxygen species (ROS) through Fenon-like reaction, which can also be generated through Haber-Weiss reaction (Ornelas & Astruc, 2023). Both ROS-generating reactions are displayed in Figure 2. Unlike Cu, Zn is not a redox-active metal but can indirectly induce oxidative stress by activating enzymes that generate ROS and radical nitrogen species (RNS), such as 12-lipoxygenase, NADPH oxidase, and the neuronal

isoform of nitric oxide synthase (Sensi *et al.*, 2009). These pathways lead to the formation of neurotoxic peroxynitrite ($ONOO^-$) from superoxide ($O_2^{\bullet -}$) and nitric oxide ($NO^{\bullet}$). Zn-induced ROS and RNS production further releases zinc from intracellular redox-sensitive stores, likely MTs, exacerbating Zn imbalance in a self-perpetuating loop-like process (Sensi *et al.*, 2009). A broader perspective suggests that this oxidative stress contributes to amyloid-beta secretion and deposition, as well as plaque aggregation (Su *et al.*, 2008).

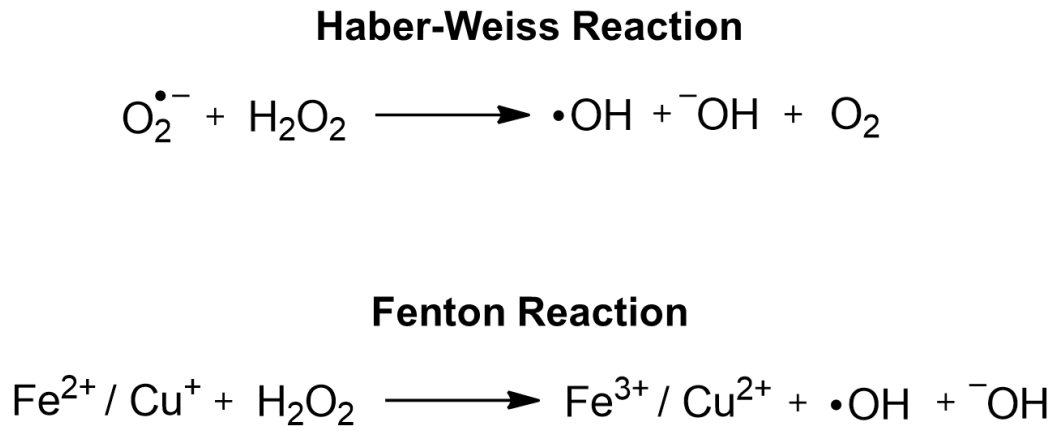

Figure 2. Haber-Weiss and Fenton reactions. Adapted from De Falco *et al.* (2016).

Both copper and zinc accelerate the aggregation of synthetic Aβ peptides in aqueous solutions by binding to histidine residues (Bush *et al.*, 1994). Zn and Cu compete for the same Aβ residues, with zinc promoting quick peptide aggregation and copper causing structural changes (Hoernke *et al.*, 2010). In AD patients, these metals are irregularly distributed, especially in the hippocampus, amygdala, nuclei, and around the senile plaques (De Falco *et al.*, 2016). These altered distributions lead to significant cellular damage, including RNA abnormalities, decreased protein synthesis, and harm to DNA, proteins, and membrane lipids, creating new sites for free radical formation (De Falco *et al.*, 2016).

Copper has a significant impact on the amyloid cascade, interacting with the amyloid precursor protein (APP) via a Cu-binding domain (Multhaup *et al.*, 1996). Higher copper levels are found in Aβ and neurofibrillary tangles, influencing APP expression (Sensi *et al.*, 2018). The interaction between Aβ peptides and Cu, along

with other metals, is believed to enhance Aβ neurotoxicity (Roberts *et al.*, 2012). Aβ glycation produces free radical superoxide anions ($O_2^{\bullet -}$), which react with copper to produce hydroxyl radicals ($^{\bullet}OH$), which constitute very energetic and reactive species, representing the most dangerous ROS in AD-related oxidative stress (Fica-Contreras *et al.*, 2017).

Thus, copper and zinc not only have primary biological functions in the brain but appear involved in several pathological mechanisms related to AD too. Metal dyshomeostasis immensely affects the progression of AD, being a centerpiece in the molecular basis of one of the main etiological hypotheses for this disease: the metal hypothesis. This underscores the importance of determining metal levels in biological samples obtained from AD patients and highlights the importance of research in chelation therapies.

1.3 Metallophores and *N*-acylhydrazones

Given the metal hypothesis, chelating agents have been developed to reduce Aβ oligomerization by removing metal ions bound to the peptide (Lu *et al.*, 2013). However, instead of indiscriminately binding and removing metals from tissues, a class of coordinating compounds called metallophores aims to restore physiological metal homeostasis. They do this by specifically binding and redistributing copper and/or zinc, thereby reducing abnormal interaction with amyloidogenic proteins or peptides and thus preventing oligomerization (Scott & Orvig, 2009). An important feature of these compounds is their moderate affinity and specificity for certain metal ions (Kharkar & Dutta, 2008). A moderate affinity is crucial because it allows the sequestration of metal ions from the peptide domain without forming permanent bonds, enabling their return to transport and storage enzymes (Kharkar & Dutta, 2008). Another goal is to reduce oxidative stress by inhibiting the production of reactive oxygen species mediated by redox-active metal ions, as discussed in the previous section, which are linked to proteins through Fenton and pseudo-Fenton reactions (Barnham & Bush, 2008; Cherny *et al.*, 2001).

However, the prolonged use of chelators usually results in serious side effects, and most chelating agents lack the properties necessary to cross the Blood-Brain Barrier (BBB) (Pardridge, 2009). In this context, clioquinol (CQ), a small lipophilic

chelator, emerged as a potential drug candidate for AD therapy due to its affinity for Zn^{2+} and Cu^{2+} (Bareggi & Cornelli, 2012). Clioquinol, initially produced as a topical antiseptic and marketed as an oral intestinal amebicide in 1934, was used to treat a variety of intestinal diseases (Bareggi & Cornelli, 2012). This compound, which contains the 8-hydroxyquinoline group in its structure, showed promising results in a study using a transgenic model of AD, reducing the presence of amyloid plaques in the brain (Mancino *et al.*, 2009). However, in the early 70s, clioquinol was withdrawn from the market as an oral agent due to its association with subacute myelo-optic neuropathy, a syndrome causing sensory and motor disturbances in the lower limbs and visual changes (Bareggi & Cornelli, 2012).

The positive results obtained with clioquinol prompted the search for other similar metallophores to avoid the side effects of the predecessor. Consequently, compounds derived from the 8-hydroxyquinoline group, such as PBT2, 8-H2QS, and INHHQ (Adlard *et al.*, 2008; de Freitas *et al.*, 2013; Gomes *et al.*, 2014), have been developed and proposed as potential treatments in the context of neurodegenerative diseases (De Falco *et al.*, 2016). Each of these compounds has demonstrated efficacy in redistributing physiological metal ions in the brains of disease-model rats (De Falco *et al.*, 2016).

Our group has been developing and testing metallophores for over a decade, pioneering research on the chemical class of *N*-acylhydrazones as promising agents for the management of metal-enhanced aggregopathies (Cukierman *et al.*, 2018). These ligands have shown satisfactory results, demonstrating efficacy in crossing the BBB, sequestering Zn^{2+} and Cu^{2+} from Aβ, affecting protein aggregation, and reducing the production of ROS *in vitro* (Carvalho *et al.*, 2023; Cukierman *et al.*, 2018; De Falco *et al.*, 2020; Hauser-Davis *et al.*, 2015).

One of such *N*-acylhydrazones developed by our group, namely, INHHQ, has shown potential in competing with both Aβ (Hauser-Davis *et al.*, 2015) and alpha-synuclein, a protein associated with Parkinson's disease (Cukierman *et al.*, 2017), for metal ion binding. This aroylhydrazone has been patented in the United States (US 10.189.811 B2 and US 10.316.019 B2). Our research group has demonstrated the efficacy of INHHQ as a protective agent in an animal model of sporadic AD: the *N*-acylhydrazone prevented both short- and long-term memory impairments

induced by the intracerebroventricular (i.c.v.) infusion of Aβ oligomers in mice at a low, single dose of 1 mg kg^{-1} (De Falco *et al.*, 2020).

N-acylhydrazones coordinate transition metal ions through the oxygen atom of the carbonyl group and the azomethine nitrogen atom (Selvam *et al.*, 2019). Besides this considerable coordinating capability, the –HC=N–NH–CO– group also possesses an electrophilic carbon (HC=N), a nucleophilic imine nitrogen (HC=N:), and an amide nitrogen atom with acidic properties (–NH–CO–) (Lawrence *et al.*, 2019). *N*-acylhydrazones can form intermolecular H bonds through the hydrogen atom bound to the amide nitrogen (–NH–CO–) and the carbonyl oxygen atom of another molecule, as well as using the azomethine nitrogen atom (HC=N:) as an H-acceptor (Socea *et al.*, 2022). Additionally, this class of compounds can exhibit amido-iminol tautomerism (Purandara *et al.*, 2019). The amide nitrogen, as stated above, is acidic and can be deprotonated in basic media or by coordinating metal ions, undergoing iminolization due to electron delocalization. The electrochemical reduction capability of *N*-acylhydrazones can lead to radical scavenging properties and radical stabilization through significant electron delocalization, depending on the substituent's structure (Lawrence *et al.*, 2019).

The *N*-acylhydrazones also exhibit geometric isomerism due to the imine group (–N=CH–). As a result, they can exist as the *E* and *Z* isomers, or a mixture of both, with the *E* isomer being generally more predominant due to its greater stability (Gamov *et al.*, 2019; Morjan *et al.*, 2014). *Z* isomers are more common when the hydrazonic structure allows for possible intramolecular hydrogen bonds in this configuration (Socea *et al.*, 2022). In addition to amido-iminol tautomerism, these compounds can have up to eight isomers: two geometric isomers (*E*/*Z*) from the C=N double bond and two conformers (*syn*/*anti*) from the amide –NH–CO– bond for each amido or iminol tautomer (Lawrence *et al.*, 2019; Ţînţaş *et al.*, 2014). The structures of the possible forms discussed are shown in Figure 3.

N-Acylhydrazones are highly valuable in the pharmaceutical industry due to their wide range of biological properties and therapeutic uses. Research on *N*-acylhydrazone compounds has reported various actions, including antitumor, cytotoxic, antibacterial, antifungal, antiviral, antiparasitic, anti-inflammatory, analgesic, immunomodulatory, enzyme inhibition, antidiabetic, anticonvulsant, antioxidant, and cardiovascular effects (Socea *et al.*, 2022).

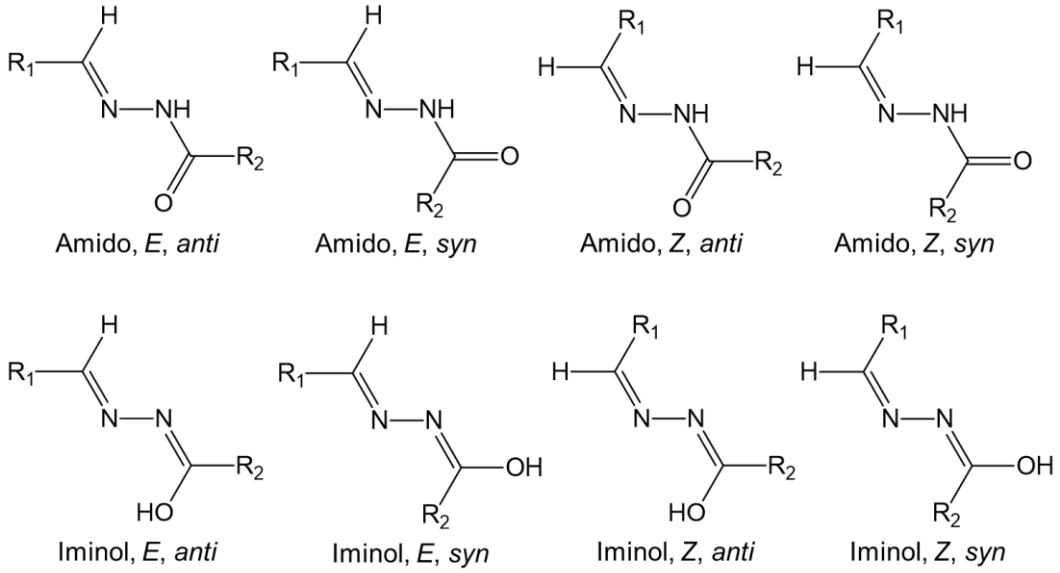

Figure 3. Isomers of *N*-acylhydrazone derivatives. Adapted from Socea *et al.* (2022).

1.4 Ferrocene-derived drugs and electrochemical sensors

In the 1940s, process technicians at Union Carbide noticed an orange sludge forming in pipes used for manufacturing cyclopentadiene (Astruc, 2017). This new compound, years later, would captivate the entire chemistry community. The initial publications in 1951 ignored Langmuir's and Sidgwick's 18-electron rule (Astruc, 2017), representing the compound as $[Fe(\eta^1\text{-}C_5H_5)_2]$, with a pair of monohapto-cyclopentadienyl ligands (Kealy & Pauson, 1951). However, in 1952, the correct sandwich structure, $[Fe(\eta^5\text{-}C_5H_5)_2]$, was revealed and published by Wilkinson, Rosenblum, Whiting and Woodward at Harvard, and by Fischer and Pfab in Munich (Fischer & Pfab, 1952; Wilkinson *et al.*, 1952). It has a D_{5h} (eclipsed) or D_{5d} (staggered) conformation and a very small rotation energy barrier of 4 kJ mol^{-1} (Astruc, 2017), displayed in Figure 4. Woodward and Whiting coined the name "ferrocene" in the 1950s (Woodward *et al.*, 1952), and its unique structure quickly fascinated chemists, standing out from any other known compound at the time (Astruc, 2017).

Ferrocene boasts exceptional properties, such as stability in air and water, reactivity as an aromatic electrophile, altogether with a mild, reversible oxidation

at approximately +0.56 V vs. SHE (Astruc, 2017) (Figure 4). These attributes, combined with its solubility in common organic solvents and the vast number of ferrocene derivatives and ferrocene-containing materials synthesized over the last 65 years, have made ferrocene an icon in organometallic chemistry (Astruc, 2017).

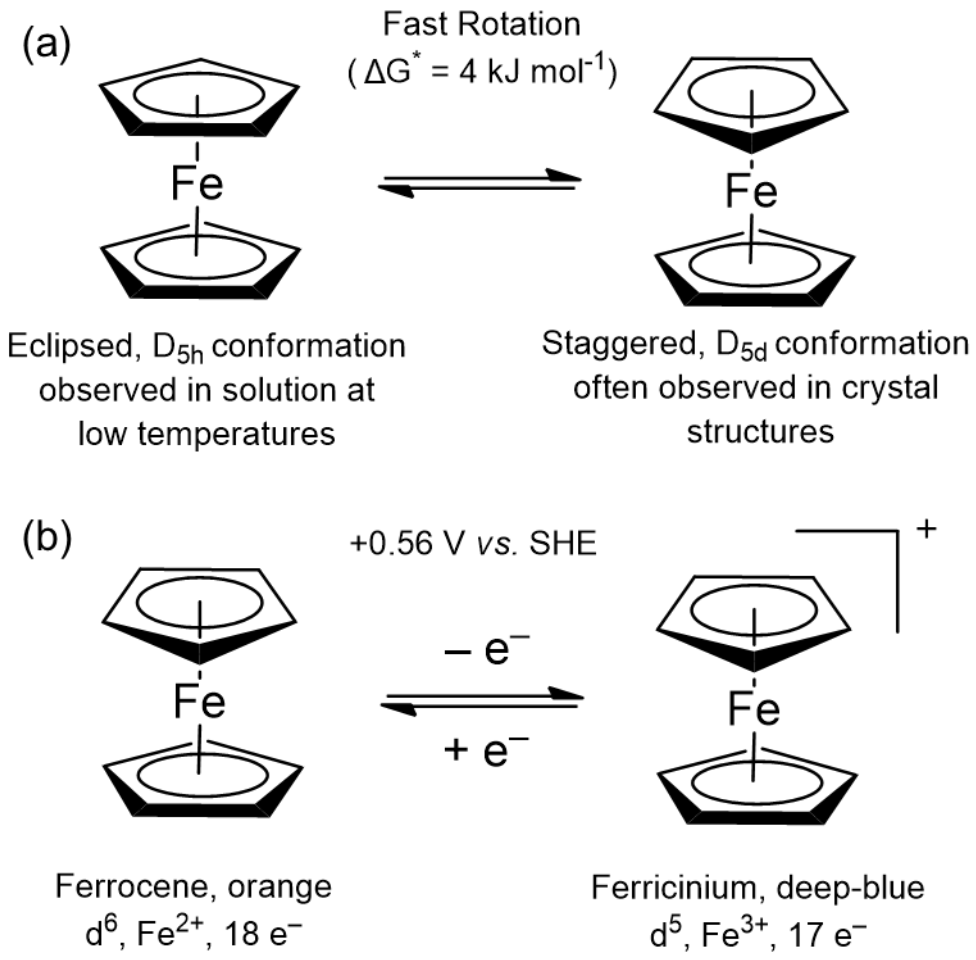

Figure 4. Ferrocene conformational equilibrium (a) and redox couple reaction (b). Adapted from Astruc (2017).

Regarding ferrocene's medicinal history, it is important to note that ferrocene itself is not very toxic. A 1969 study in dogs found that daily oral administration of 300 mg kg^{-1} of ferrocene for six months or 1000 mg kg^{-1} for three months led to haemosiderosis, an unusually high, dose-related accumulation of iron (Yeary, 1969). However, no latent adverse effects were observed in dogs kept for 12–26 months after the six-month treatment period (Yeary, 1969).

Among ferrocene derivatives, ferrocerone was used to treat anemia in the former USSR during the 1970s, reportedly being the first and perhaps only ferrocenyl drug approved for medical use, though it is no longer available (Patra & Gasser, 2017). The lipophilicity of ferrocenyl groups allows ferrocerone to be administered orally, making it useful for treating gum diseases, unlike simple Fe^{2+} salts (Patra & Gasser, 2017). The incorporation of a ferrocenyl group into known drugs was first reported in the 1960s. Initially, these new ferrocenyl conjugates, such as ferrocenyl amphetamine and diphenylhydantoin, showed no biological activity (Loev & Flores, 1961). More success was found with studies on ferrocenyl-containing penicillin and cephalosporin derivatives, which exhibited moderate antibacterial activity (Edwards *et al.*, 1975; Edwards *et al.*, 1976). However, the real breakthroughs in modern medicinal organometallic chemistry came in 1996 and 1997 with independent discoveries of the anticancer drug candidate ferrocifen (Top *et al.*, 1996) and the antimalarial drug candidate ferroquine (Biot *et al.*, 1997). Several ferrocifens, which are ferrocene analogs of tamoxifen (a chemotherapeutic for hormone-dependent breast cancer), are now in preclinical evaluation (Ornelas & Astruc, 2023). Meanwhile, the compound ferroquine, in combination with artefenomel, completed phase IIb clinical evaluation in 2019 and was found to be effective against both chloroquine-sensitive and chloroquine-resistant strains of *Plasmodium falciparum* (Ornelas & Astruc, 2023).

A plethora of studies have been published regarding ferrocenyl-containing pharmacophores to treat infectious diseases, including parasitic, bacterial, fungal, and viral infections. However, unlike ferrocifens and ferroquines, the relationship between structure and biological activity has been scarcely demonstrated (Ornelas & Astruc, 2023). In many ferrocene-containing drugs, the production of reactive oxygen species (ROS) through Fenton-like reactions with ferrocene plays a key role (Chaudhary & Poonia, 2021; Ludwig *et al.*, 2019). There are significant differences between the oxidation of free Fe^{2+} and ferrocene, including solubility, coordination sphere, and the potential associated. Fe^{2+} salts are typically water-soluble, whereas ferrocene is highly lipophilic. Another key difference is that in ferrocene and its derivatives, Fe^{2+} is coordinatively saturated (a stable 18-electron organometallic), preventing radicals from binding to the iron center. This contrasts with hydrated Fe^{2+}, where the H_2O ligands are easily deprotonated or even displaced. The redox

potential directly influences the rate of Fe^{2+} oxidation, with ferrocene being oxidized slightly more easily than aqueous Fe^{2+} ions (Ornelas & Astruc, 2023). Additionally, ring substituents affect this redox potential. Specifically, when the ferrocenyl group has carbonyl or aromatic groups on the rings, oxidation becomes more difficult (Connelly & Geiger, 1996). It has been reported that the cytotoxicity of ferrocene derivatives and ROS-activated prodrugs increases with lower redox potential (Věžník *et al.*, 2021).

The ferrocene moiety, with its chemical stability, versatile functionalization, and redox reversibility, is an ideal unit for designing electrochemical sensors (Fabbrizzi, 2020). The well-established synthetic routes for ferrocene enhance its utility in constructing molecular receptors, which frequently incorporate ferrocene functionalities as signaling or reporter groups, with their redox responses being affected upon binding selected guest molecules (Torriero & Mruthunjaya, 2023). In addition, this group can serve as a structural component, allowing precise control over the topology of the guest binding site (Torriero & Mruthunjaya, 2023). This dual functionality enables ferrocene-based receptors to exhibit diverse capabilities beyond those of purely organic architectures (Torriero & Mruthunjaya, 2023).

The rich reactivity of ferrocene has led to the synthesis of widely utilized compounds. Functionalizing ferrocene, for instance by the electrophilic addition of an aldehyde, generates precursors such as ferrocenecarboxaldehyde (which is crucial to this work) for the synthesis of many ferrocene-derived compounds, enabling the exploration of the remarkable electrochemical properties of the ferrocenyl group.

2. Work Proposal and Justification

AD is a devastating neurodegenerative disorder that profoundly impacts individuals, their families, and healthcare systems. Characterized by progressive cognitive decline, memory loss, and behavioral changes, this disease significantly diminishes the quality of life of affected individuals and places a considerable burden on caregivers. Despite extensive research, there is currently no cure for AD, and available treatments only offer limited symptomatic relief (Yiannopoulou & Papageorgiou, 2020). The urgent need to develop effective therapeutic interventions is underscored by the increasing prevalence of AD, driven by an aging global population (Prince *et al.*, 2016).

Moreover, AD lacks a definitive and reliable diagnostic method, posing significant challenges for early detection and intervention. Currently, AD diagnosis relies heavily on clinical evaluation, cognitive testing, and neuroimaging, which can be subjective and inconsistent (Weiner *et al.*, 2015). Biomarkers such as amyloid-beta and tau proteins, identified through cerebrospinal fluid analysis or positron emission tomography (PET) scans, offer some promise but are not universally accessible and can be invasive and expensive (Blennow *et al.*, 2015).

In this sense, the absence of either a proper treatment or a reliable and non-invasive diagnostic tool highlights the need for ongoing research to develop more accurate and accessible methods for managing AD at its earliest stages.

From this perspective, this work proposes the synthesis and evaluation of ferrocene-derived *N*-acylhydrazone ligands in two branches: as metallophores, in order to progress with assessments in AD treatment by chelating agents; and as electrochemical probes, in order to exploit ferrocene's reversible nature and well-defined voltammetric properties to develop frontiers in the AD diagnosis.

The ferrocenyl-*N*-acylhydrazonic structure will be maintained through both ligands, **Feizone** and **Ferfurone**, synthesized in the present work (Figure 5). As previously mentioned, *N*-acylhydrazones have shown outstanding results as a new class of metallophores for the management of neurodegenerative disorders (Carvalho *et al.*, 2023; Cukierman *et al.*, 2018; Cukierman & Rey, 2022; De Falco *et al.*, 2020; Hauser-Davis *et al.*, 2015).

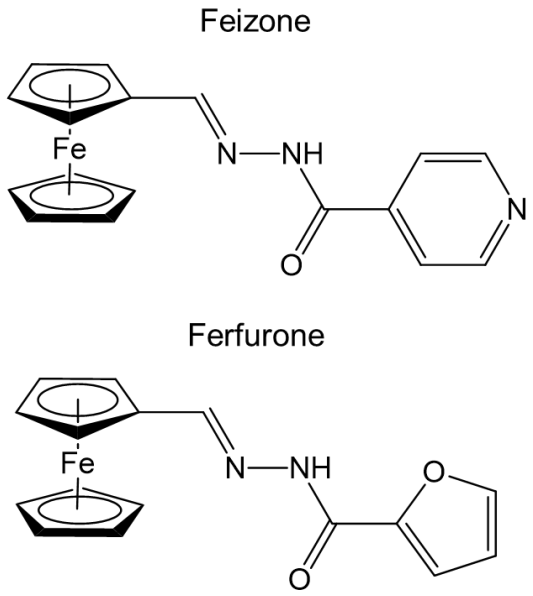

Figure 5. Chemical structure of **Feizone** and **Ferfurone** ligands.

Besides the electrochemical properties to be explored, ferrocene's lipophilicity may assist in locating and binding the insoluble Aβ aggregates, playing a double role in these compounds. *N*-acylhydrazones are usually prepared by a simple condensation reaction between an aldehyde and *N*-acylhydrazide. The hydrazides chosen in here have a pyridine and a furan group for **Feizone** and **Ferfurone**, respectively. These groups were carefully selected due to their biocompatibility and satisfactory pharmacologic results in other hydrazones studied by our group.

Ferrocene in biological applications is known for its ROS-generating capability on Fenton-like reactions (Ornelas & Astruc, 2023). However, as already mentioned, this ability is mildly attenuated due to ferrocene properties, compared to free aqueous Fe^{2+}. Additionally, *N*-acylhydrazones, especially the ones with great electron delocalization, have remarkable radical scavenging properties, hopefully inhibiting the possible formation of radicals.

Moreover, studies show evidence that copper levels abnormalities serve as a biomarker for a subgroup of AD and have a role in its progression (Squitti *et al.*, 2017). This fact expands the possibilities as electrochemical probes for the ligands proposed in the present work. Either signaling AD biomarkers by binding to Aβ peptides or binding abnormous metal ions such as Cu^{2+}.

3. Objectives

3.1 General Objective

The present work aims to evaluate the use of *N*-acylhydrazones containing a ferrocene portion as possible metallophores for the management of Alzheimer's disease (AD) in biologically relevant systems, as well as to assess their potential as electrochemical probes for the identification of beta-amyloid (Aβ) peptide plaques. To fulfill this goal, two biocompatible *N*-acylhydrazones and their respective Cu^{2+} and Zn^{2+} complexes will be prepared. These systems will be broadly characterized, in addition to stability studies, and determination of parameters such as p*K*a and the stoichiometry of complex formation through cyclic voltammetry. In order to assess the ligand's relevance as electrochemical probes in the context of AD, a preliminary voltammetric study of their interactions with the Aβ peptide will be included.

3.2 Specific Objectives

- To synthesize **Feizone** and **Ferfurone**, ferrocene-derived *N*-acylhydrazonic ligands of interest;
- To characterize structurally and electrochemically the prepared ligands;
- To synthesize and characterize the respective Cu^{2+} and Zn^{2+} mononuclear complexes of the synthesized ligands in solid state;
- To estimate the apparent p*K*a of the ligands through cyclic voltammetry;
- To evaluate the solution hydrolytic and photolytic stability of the hydrazones;
- To describe the interactions of such ligands with Cu^{2+} and Zn^{2+} ions by the electrochemical behavior of the ferrocenyl moiety;
- To assess the theoretical pharmacological data using *in silico* techniques;
- To estimate the capability of the *N*-acylhydrazones ligands as scavengers of electrochemically-generated superoxide radicals;
- To study the ligands' interaction with the $A\beta_{1-40}$ (full-length) peptide through square-wave voltammetry.

4. Methodology

All reagents and solvents used in this work were purchased from commercial sources with the highest purity available and employed without further purification unless specifically mentioned below. Water was either ultra-pure or bi-distilled.

4.1. Pharmacological Analysis

The descriptor parameters Molecular Weight, cLog P, cLog S, PSA, Druglikeness and Drug-score were calculated using the program Osiris Property Explorer: DataWarrior™, a software freely available for download at http://www.organic-chemistry.org/prog/peo/, accessed on 09/05/2024.

4.2. Syntheses

4.2.1. Syntheses of the Ligands

The ligands **Feizone** and **Ferfurone** were synthesized as displayed in Figure 6. A solution of the respective *N*-acylhydrazide in 20 mL of methanol was added dropwise with stirring to a round-bottom reaction flask containing a MeOH (5 mL) solution of ferrocenecarboxaldehyde (~1.0 mmol). Pyridine-4-carbohydrazide or furan-2-carbohydrazide (1.0 mmol) were used to prepare **Feizone** and **Ferfurone**, respectively. The reaction mixture was heated in reflux at 80-85ºC during 4 h. Both reactions resulted in a red clear solution and did not need to be filtered. After resting at the bench, protected from light, single crystals suitable for analysis by X-ray diffraction (XRD) were obtained. Yield: 68% (**Feizone**) and 73% (**Ferfurone**).

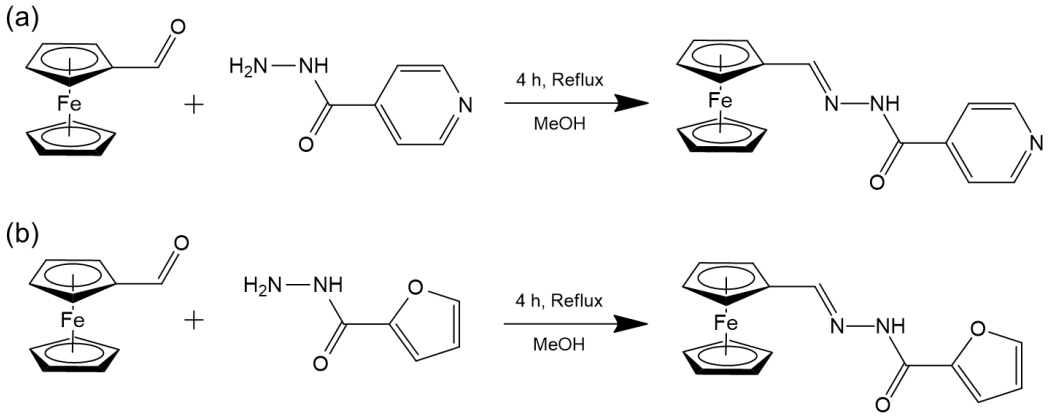

Figure 6. Reaction schemes for ligands **Feizone** (a) and **Ferfurone** (b).

4.2.2. Syntheses of the Zinc(II) Complexes

The zinc coordination compounds were systematically named **Feizone-Zn** and **Ferfurone-Zn** (Figure 7). A solution of the ligand (0.50 mmol) in methanol (15 mL) was added dropwise with stirring to a solution of $ZnCl_2$ (0.25 mmol) in methanol (5 mL) in order to work with a 1:2 metal:ligand stoichiometry. Afterward, a methanol solution (5 mL) of NaOH (0.50 mmol) was gently added dropwise. The reaction mixture was heated under reflux at 80 ºC for 4 h. After resting, the mixtures showed precipitates, which were filtered and characterized. Yield: 43% (**Feizone-Zn**). **Ferfurone-Zn**, on the other hand, was not obtained as an isolatable product, resulting in a thin powder residue that could not be properly characterized. Yet, it apparently reacted due to its change in color for a bright red solution.

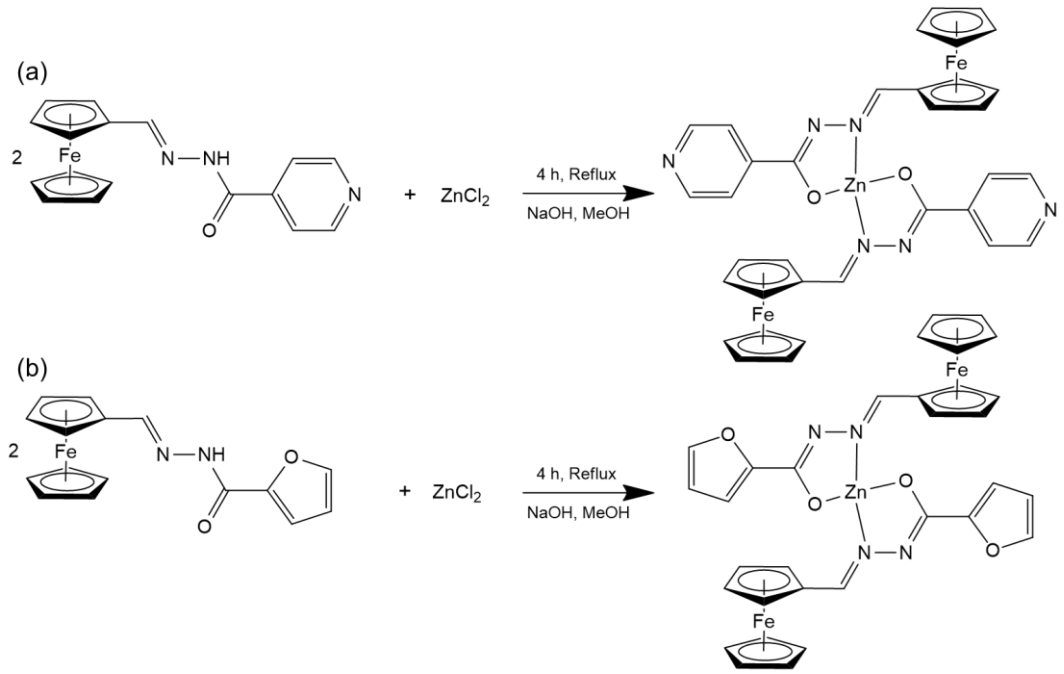

Figure 7. Reaction schemes for complexes **Feizone-Zn** (a) and **Ferfurone-Zn** (b).

4.2.3. Syntheses of the Copper(II) Complexes

Similar to zinc, the copper compounds were systematically named **Feizone-Cu** and **Ferfurone-Cu**. Note that, in this case, the reaction didn't need the addition of base (Figure 8). A solution of the ligand (0.50 mmol) in MeOH (15 mL) was added dropwise with stirring to a solution of $Cu(NO_3)_2 \cdot 3H_2O$ (0.25 mmol) in methanol (5 mL), aiming to produce the 1:2 metal:ligand complexes. The reaction mixture didn't need to be heated, and the whole reaction went at room temperature. After two hours, the **Feizone-Cu** mixture presented a purple residue, meanwhile, **Ferfurone-Cu** ended in a red clear solution. After resting protected from light, the mixtures showed precipitates, which were filtered and characterized. **Ferfurone-Cu** presented red single crystals, which were submitted to XRD characterization. Yield: 37% (**Feizone-Cu**) and 9% (**Ferfurone-Cu**).

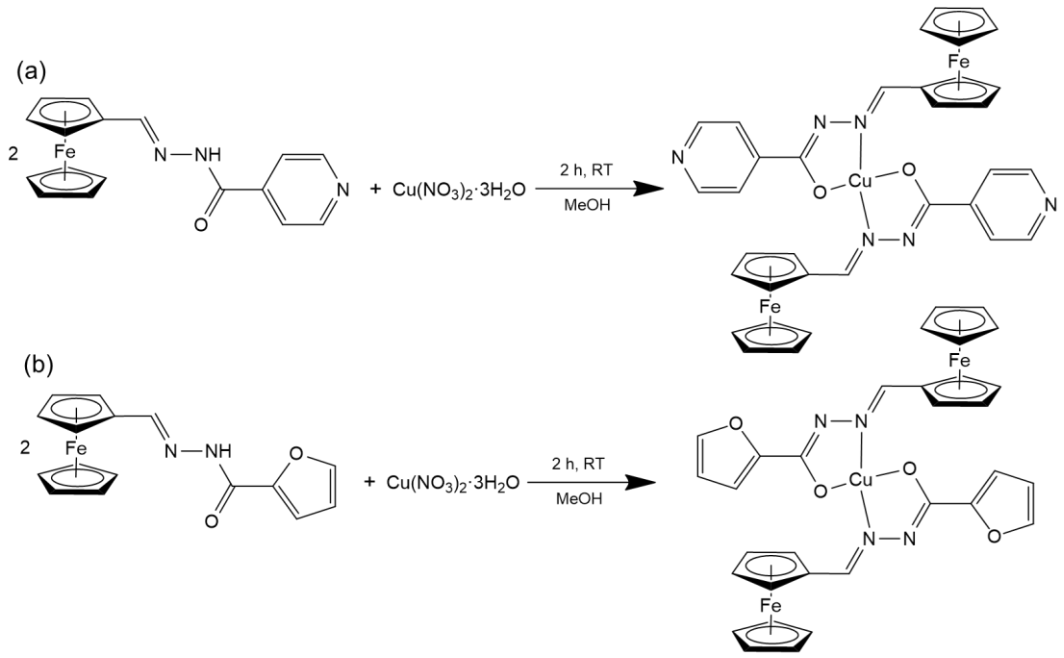

Figure 8. Reaction schemes for complexes **Feizone-Cu** (a) and **Ferfurone-Cu** (b).

4.3. General Characterization

4.3.1. X-ray Diffraction Crystallography

Single crystal XRD data were collected by Prof. Renata Diniz (UFMG) in a Rigaku Synergy diffractometer using CuKα (λ= 1.54184 Å) radiation at room temperature (299 K). Data collection and reduction, as well as cell refinement, were performed using the CRYSALISPRO software (Rigaku, 2015). The structures were resolved and refined by SHELX (Sheldrick, 2015) using OLEX2 system (Dolomanov *et al.*, 2009), and all non-hydrogen atoms were refined with anisotropic thermal parameters. H atoms connected to carbon were placed in idealized positions and treated by a rigid model, with Uiso(H) = 1.2 Ueq for aromatic rings and CH groups. The figures were drawn using ORTEP-3 for Windows (Farrugia, 2012) and Mercury (Macrae *et al.*, 2008) softwares.

4.3.2. Infrared Vibrational Spectroscopy

Mid-infrared vibrational spectra were acquired on a Perkin-Elmer Spectrum 100 FTIR spectrophotometer, sampling: KBr pellets, in the 4000–400 cm^{-1} range with a resolution of 4 cm^{-1}, at room temperature.

4.3.3. Nuclear Magnetic Resonance (NMR)

Both ligands were characterized by ^{1}H NMR spectroscopy. The spectrum was recorded on a Bruker Avance III HD-400 spectrometer, operating at 400 MHz and 298 K. The samples were solubilized in 0.5 mL of deuterated dimethylsulfoxide (DMSO-d_6). Calibration was made based on the residual solvent signal: a quintet at 2.50 ppm for the H nucleus. This analysis was performed at the Analytical Facilities "Pe. Leopoldo Hainberger" of the Department of Chemistry at PUC-Rio.

For the photolytic stability study, NMR spectra of ferrocenecarboxaldehyde, **Feizone,** and **Ferfurone** were taken of the same solutions used for characterization after 24 h and rested beside the laboratory's window receiving natural sunlight exposure.

4.3.4. Conductimetry Study

The conductivity measurements were performed at room temperature in an electrical conductivity Metrohm 650 MA Analyser for ferrocenecarboxaldehyde, **Feizone,** and **Ferfurone** in a concentration of 1.0 mmol L^{-1} in DMSO and MeOH. Measurements were taken in fresh solutions and after 24 h of sunlight exposure.

4.3.5. Thermogravimetric Analysis (TGA)

Thermogravimetric curves were acquired in a Thermogravimetric Analyzer Perkin Elmer, Pyris 1 TGA. The scans were performed from 50 to 900 ºC at 10 ºC

min^{-1} under a nitrogen atmosphere. All samples used in this analysis were crystals, when applicable. For the **Feizone** complexes, the reaction's precipitates were used.

4.3.6. Emission Spectroscopy

Around 1 mg of the prepared ligands and complexes was digested with 1 mL of nitric acid and filled with distilled water to 50 mL in a centrifuge tube. This solution was then analyzed with three recordings by Inductively Coupled Plasma Optical Emission Spectrometry (ICP-OES), in a model Optima 7300DV (Perkin-Elmer Instruments) equipment, previously calibrated to Iron, Copper, and Zinc. The external calibration of the equipment was done from the appropriate dilutions of the multi-element standard (Merck IV). This assay was performed at the Analytical Facilities "Pe. Leopoldo Hainberger" of the Department of Chemistry at PUC-Rio.

4.4 Molecular Absorption Spectroscopy

UV-Vis spectra, over the wavelength range 200–800 nm, were recorded in an Agilent spectrophotometer Cary 100 using 10 mm quartz cuvettes. These assays were also performed at the Analytical Facilities "Pe. Leopoldo Hainberger" of the Chemistry Department at PUC-Rio.

4.4.1. Hydrolytic Stability Studies

The ligands were prepared in a mixture of 1% DMSO/TRIS buffer solution (10 mmol L^{-1}), pH 7.4, at the concentration of 50 μmol L^{-1}. The first reading was made shortly after the preparation of the solutions, which were then left for resting on the cuvette, sheltered from light. Successive hour by hour readings were made for 12 h. Additional readings of 24 and 48 hours were also performed. The reaction precursors were read only once in the same concentration.

4.4.2. Photolytic Stability *via* UV-Vis Spectroscopy

To study the susceptibility of decomposition reactions mediated by light for ferrocenecarboxaldehyde and ligands **Feizone** and **Ferfurone** in DMSO solution (denominated photolytic stability), two sets of 1 mmol L^{-1} solutions in DMSO were prepared for each compound. One set was exposed to sunlight, while the other set was stored protected from light sources. In this way, the UV-Vis spectra of these sets were taken at 1-hour intervals each during 4 h.

4.5. Voltammetry Assays

Cyclic and square wave voltammetry experiments were performed at room temperature in a BASi Epsilon™EC potentiostat/galvanostat. Experiments were carried out under nitrogen atmosphere at 25 ºC, in a three-electrode cell. A 3.0 mm diameter Glassy Carbon Electrode was employed as the working electrode. The BASi MF-2052 Ag/AgCl (3 mol L^{-1} KCl) electrode was used as the reference, while the counter-electrode consisted of a platinum wire.

4.5.1. Cyclic Voltammetry Characterization

The voltammetric behavior of the ligands was characterized at 1.0 mmol L^{-1} in 5.0 mL of a methanol/water 1:1 mixture, with NaCl 0.1 mol L^{-1} as the supporting electrolyte, at different scan rates. The potential limits for the voltammetry were carefully chosen to fit the voltammetric range of the ferrocenyl group. For these ligands, the voltammogram was taken from 0.1 to 0.8 V, starting at 0.2 V. The direction was planned to show the oxidation of the ferrocene into ferrocenium first and, therefore, its reduction back to ferrocene. In this way, these compounds were characterized at scan rates of 5, 50, 75, 100, 150, 200, 300, 400, 500, 600, 800, 1000, 1493, 2000, 3030, 4000, 5000, 5882, 5900, 7143, 8333, 9091, 10000, 12500, 14286, 20000, and 25000 mV s^{-1}. Meanwhile, the prepared complexes could not be properly dissolved in a methanol/water mixture, so for the characterization of these complexes, a solution of 1.0 mmol L^{-1} in DMSO (5.0 mL) with $TBAPF_6$ 0.1 mol L^{-1} as the supporting electrolyte was used at the scan rate of 100 mV s^{-1}.

The same scan direction was employed, although the potential limits needed to be shifted because of the solvent used. In this case, we went from 0.3 V to 1.0 V, starting at 0.4 V.

4.5.2. Square-Wave Voltammetry

For these studies, 2.00 mL of a 10 μmol L^{-1} solution of each ligand and the precursor ferrocenecarboxaldehyde were prepared in a 1% DMSO/HEPES buffer solution (10 mmol L^{-1}), pH 7.4, with 0.1 mol L^{-1} NaCl as the supporting electrolyte. These are the same conditions of the interaction study with $A\beta_{1-40}$ involving ligands **Feizone** and **Ferfurone**. Thereafter, the solutions were scanned using square wave voltammetry, with a 1.0 mV step, in both anodic and cathodic scanning directions, from 0.2 V to 0.8 V at 100 mV s^{-1} scan rate.

4.5.3. Apparent p*K*a through Cyclic Voltammetry

The p*K*a of both ligands were estimated through cyclic voltammetry using a 10.0 mL methanol/water 1:1 solution containing 0.1 mol L^{-1} NaCl and the ligands at 1.0 mmol L^{-1}. The scanning direction and the potential limits were the same as used in the characterization and the scan rate was 100 mV s^{-1}. The pH was adjusted to 4.0 by the addition of small quantities (2 μL / addition) of aqueous 1.0 mol L^{-1} HCl solution. Afterward, the pH was adjusted using NaOH 1.0 mol L^{-1}, reading at every 0.5 points of pH until pH 10, and then at every 0.2 points of pH until pH 12.

4.5.4. Photolytic Stability Cyclic Voltammetry Study

To study the behaviour of ligands and ferrocenecarboxaldehyde before and after the exposure to sunlight, DMSO and MeOH solutions of these compounds were prepared at 500 μmol L^{-1} with $TBAPF_6$ 0.1 mol L^{-1} as supporting electrolyte. Cyclic voltammograms were taken from 0.3 to 1.0 V, starting at 0.2 V at the scan

rate of 100 mV s^{-1}, at time 0 (fresh solutions) and after 24 h with these compounds receiving natural sunlight exposure after resting beside the window in the laboratory.

4.5.5. Zinc Complexation Study through Cyclic Voltammetry

Firstly, to 5.0 mL of a 1.0 mmol L^{-1} solution of each ligand in methanol/water 1:1 containing 0.1 mol L^{-1} NaCl as the supporting electrolyte, 10 µL aliquots (i.e., 0.2 molar equivalents) of a 0.1 mol L^{-1} $ZnCl_2$ solution were successively added until reach a three-fold excess of metal over ligand. After each addition, a voltammogram was registered at the scan rate of 100 mV s^{-1}. The scan direction and potential limits were the same as in the methanol/water mixture used for characterization. As we observed during the syntheses that both ligands needed a basic medium for the zinc complexation reaction to occur, a supplementary assay was performed. This time, before starting the titration with zinc(II), we added an amount of NaOH solution enough to reach a hydroxide concentration of 1.0 mmol L^{-1}. Then, we initiated the successive additions of $ZnCl_2$ solution, as described in the preceding experiment. All the voltammetry parameters were also set as previously mentioned.

4.5.6. Copper Complexation Study through Cyclic Voltammetry

Similar to the zinc complexation study, for the copper(II) coordination assays, 10 µL (0.2 equivalents) of a 0.1 mol L^{-1} $CuCl_2 \cdot 2H_2O$ solution were added successively to 5.0 mL of the respective ligand solution in MeOH/water 1:1 with 0.1 mol L^{-1} NaCl until reach a three-fold excess of metal over ligand. Different from the case of zinc, however, a strong base was not added to the ligand before the titration. After each addition, a cyclic voltammogram was registered. The scan rate was adjusted at the value of 100 mV s^{-1}, as in previous experiments.

4.5.7. Superoxide Radical Scavenging Activity

To generate *in situ* the superoxide radicals, 5.0 mL of DMF was taken to the potentiostat and vigorously stirred, without the usual dinitrogen infusion, in order to properly solubilize the dioxygen present in the air into the DMF. Thereafter, the scanning was set to start at −1.2 V to −0.5 V, and back to −1.2 V, completing one cycle. In this way, four cycles were recorded, discarding the first one, as on the first scanning the electrode was still reaching equilibrium. A separate scan with N_2 atmosphere was also recorded for the sake of comparison. In this stage, a ligand solution in DMF was successively added, reaching concentrations of 100, 200, 300, 400, and 500 μmol L^{-1} for **Feizone,** and an extra reading at 800 μmol L^{-1} for **Ferfurone**. The cycles were compared and statistically treated.

4.5.8. Preliminary Study of the Interaction with $A\beta_{1-40}$ Peptide

In this assay, 2.00 mL of a 10.0 μmol L^{-1} solution of each ligand was prepared in a 1% DMSO/HEPES buffer solution (10 mmol L^{-1}), pH 7.4, with 0.1 mol L^{-1} NaCl as the supporting electrolyte. Afterward, 10.0 μL aliquots of a 500 μmol L^{-1} basic solution of $A\beta_{1-40}$ was successively added until the peptide concentration in the cell reached 20 μmol L^{-1} (2.0 equivalents). After each Aβ addition, a square wave voltammogram was got from 0.8 to 0.2 V (cathodic scan), with 1.0 mV step.

5. Results and Discussion Part I – Syntheses and Characterization

5.1 Ligands' Precursors

All precursors for the syntheses were bought in high purity (>98%) from trusted suppliers and characterized only to evaluate their purity and for comparison with the respective products. The characterization of the ferrocenecarboxaldehyde precursor is discussed below to assist the understanding of subsequent studies.

5.1.1. Ferrocenecarboxaldehyde

On the IR spectrum (Figure 9), the strongest band at 1680 cm^{-1} is attributed to the C=O carbonyl stretch, as expected due to the polarized nature of this bond (Silverstein *et al.*, 2014). When compared to the ν(C=O) band of aliphatic aldehydes (1740-1720 cm^{-1}), a lower wavenumber value is observed for our precursor due to the orbitals in the aromatic ring which overlap with the carbonyl orbitals, allowing some of the electron density from the carbonyl double bond to be pulled off into the aromatic ring in a phenomenon known as conjugation (Silverstein *et al.*, 2014). The aldehyde group can also be characterized by the ν(C-H) bands at 2764 cm^{-1} and 2833 cm^{-1}. Other noticeable absorptions are related to the ferrocenyl-derived modes $\nu(C\text{-}H)_{Cp}$ at 3090 cm^{-1} and $\nu(C\text{-}C)_{Cp}$ at 1106 and 1411 cm^{-1} (Nakamoto, 2009).

The bands assigned to vibrations of the cyclopentadienyl (Cp) rings are localized above 600 cm^{-1} and metal-ligand vibrations, below 500 cm^{-1}, making it possible to discuss the ligand and skeletal modes separately (Garkusha *et al.*, 1998). Although far-IR spectra weren't recorded in this work, mid-IR spectra start at 400 cm^{-1}, contemplating two noticeable bands between 400-500 cm^{-1}: ν(Fe-Cp) and

Ring Tilt ($\delta_{assym.}$). As a reference, the wavenumber values for these bands for ferrocene itself are 478 cm^{-1} and 492 cm^{-1}, respectively (Nakamoto, 2009). For the precursor ferrocenecarboxaldehyde, 458 cm^{-1} was assigned for ν(Fe-Cp) and at 499 cm^{-1}, the Ring Tilt by direct comparison with similar molecules in the literature (Appel *et al.*, 2014; Diana *et al.*, 1997; Phillips *et al.*, 1988). However, without a focused study on this matter or theoretical models, it is intricate to attribute bands in the IR spectrum. Thus, the assigned bands inside this range should be taken merely as a proposition in order to discuss the subject.

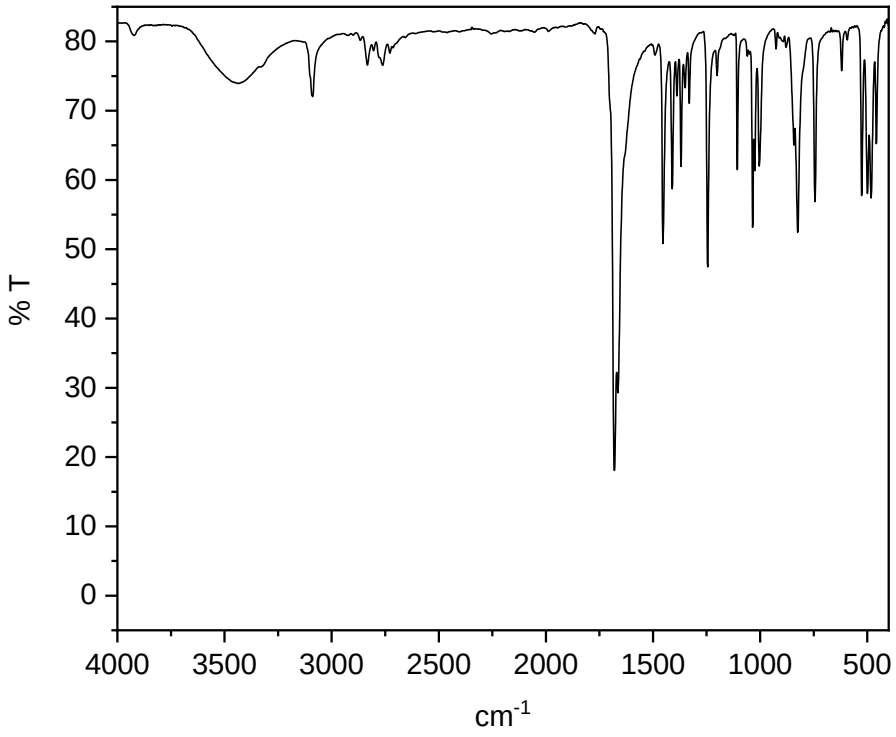

Figure 9. Mid-IR spectrum of the synthetic, commercial precursor ferrocenecarboxaldehyde in KBr disc, at room temperature.

On the other hand, the ^{1}H NMR spectrum of this precursor is presented in Figure 10 along with its complete assignment, showing a group of four signals, corresponding to the ten hydrogen nuclei in this molecule. The hydrogen from the aldehyde group appears as a singlet in 9.89 ppm, as the most de-shielded signal. Two triplets are found in 4.82 and 4.68 ppm, corresponding to the types B and C hydrogen atoms localized at the substituted ring, being more de-shielded the ones that are closer (type B) to the aldehyde bond. The lower field signal in 4.31 ppm integrates for 5 H, corresponding to the five hydrogens at the unsubstituted ring.

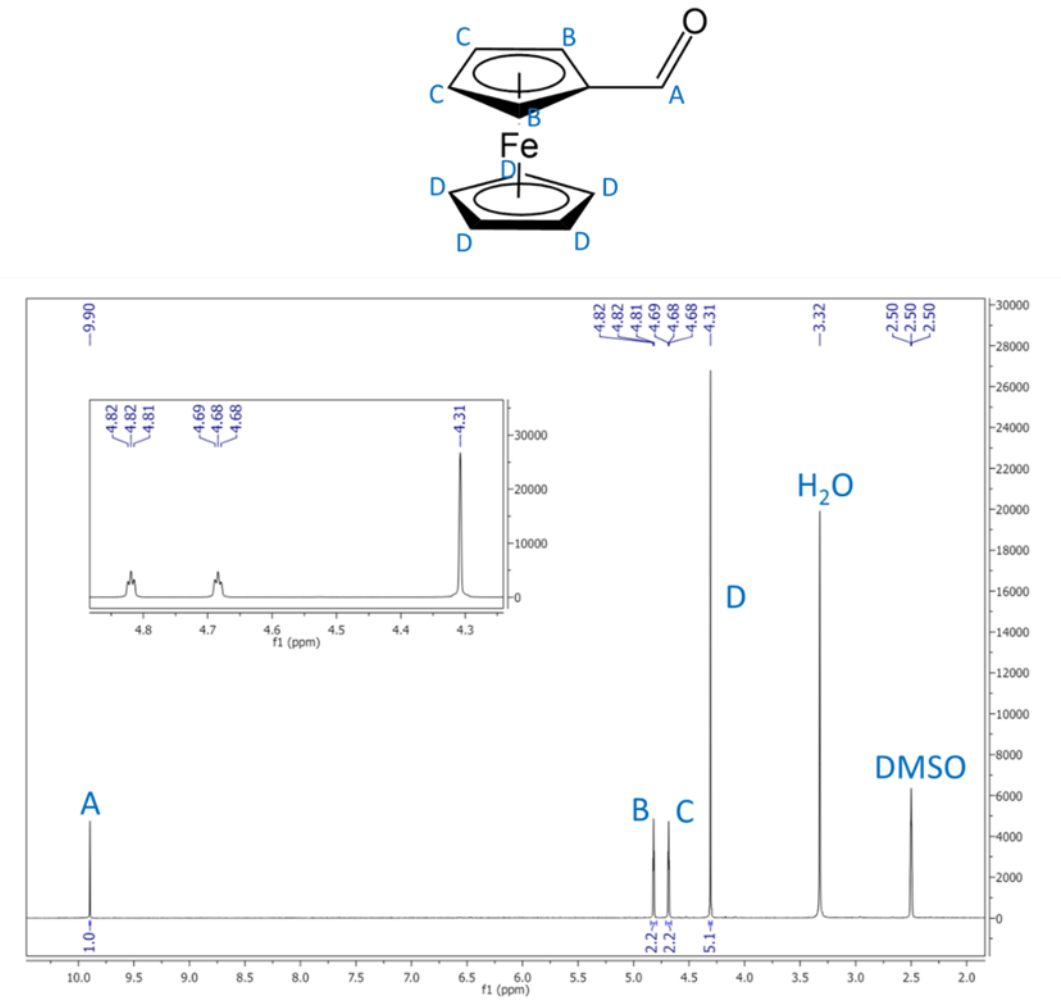

Figure 10. ^{1}H NMR (400 MHz) spectrum of the synthetic precursor ferrocenecarboxaldehyde, in DMSO-d_6, at room temperature.

5.2 Syntheses and Characterization of the Ligands

Both ligands were synthesized in methanol and were soluble at the end of the reaction time. Both resulted in red clear solutions that, after resting protected from light for crystallization, produced monocrystals that were filtered and characterized, with yields of 68% and 73% for **Feizone** and **Ferfurone**, respectively.

Feizone and **Ferfurone** are not new compounds, both being described along with crystal data recently by Ravindran *et al.* (2023) as ligands for ruthenium complexes synthesized to investigate their catalytic activity toward acceptorless dehydrogenative coupling reactions. However, these systems have not been reported in a study as metallophores or electrochemical probes for use in the context

of human neuropathologies; moreover, literature lacks a detailed study of **Feizone**/**Ferfurone** complexation *via* voltammetric assays. Both ligands are usually reported as being synthesized in ethanol and then recrystallized using another solvent or mixture (Gupta *et al.*, 2014; Krishnamoorthy *et al.*, 2012; Patil *et al.*, 1982; Ravindran *et al.*, 2023). This work, instead, describes these syntheses in MeOH, which produces soluble products easily crystallizable within its own solvent.

5.2.1. Crystallographic Analysis

The crystallographic information of both ligands can be found in Table 1. The single crystal XRD for **Feizone** (Figure 11a) showed hydrazone molecules in *anti*-conformation, regarding the amide bond, and in the form of (*E*)-isomers toward C=N, which crystallized in the orthorhombic system, space group $P2_12_12_1$ with two molecules *per* unit cell ($Z = 2$). Moreover, the lattice is stabilized by moderate to strong (Steiner, 2002) hydrogen bonds between the hydrazone and the nitrogen from the pyridine group of a neighbor molecule [N2–H12···N3^a 2.854(1) Å], generating linear 1D chains that run parallel to the crystallographic axis *b*. The H-bonding information is presented in Table 2. The structure also present π–π stacking interactions between the pyridine ring and the unsubstituted cyclopentadienyl ring from the ferrocene group (centroid-centroid distance of 3.626 Å). These intermolecular interactions for **Feizone** are displayed in Figure 12.

Although synthesized using another solvent, the **Feizone** crystal data recently reported by Ravindran *et al.* (2023) fit into the same crystal system and space group. The cell size and bond distances present only slightly different values from the experimental data reported in the present work. Those differences, however, are not significant and the structures can be considered virtually the same.

Table 1. Experimental crystallographic details for **Feizone** and **Ferfurone**.

Crystal	Feizone	Ferfurone
Chemical formula	$C_{17}H_{15}ON_3Fe$	$(C_{16}H_{14}O_2N_2Fe{\cdot}CH_4O)_2$
***M*r (g mol^{-1})**	333.17	708.37
Crystal system, space	Orthorhombic, $P2_1\ 2_1\ 2_1$	Orthorhombic, $Pna2_1$
Temperature (K)	299	299
***a*, *b*, *c* (Å)**	6.6863(1), 10.6806(1), 20.8280(2)	13.4446(1), 6.3240(1), 39.1635(4)
***V* (Å^3)**	1487.40(3)	3329.82(7)
Z	2	4
Radiation type	Cu *K*α	Cu *K*α
μ (mm^{-1})	4.08	7.40
Crystal size (mm)	0.24 × 0.18 × 0.05	0.34 × 0.16 × 0.09

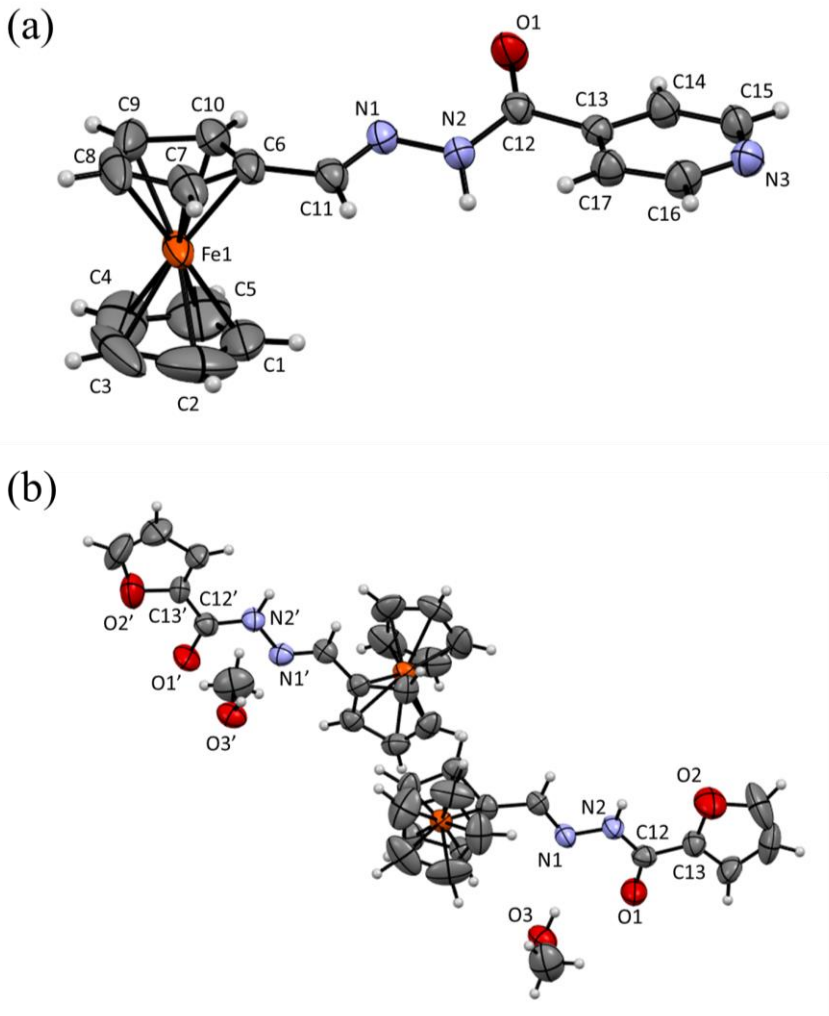

Figure 11. ORTEP representation of **Feizone** (a) and **Ferfurone** (b). The ellipsoids were drawn at the 50% probability level.

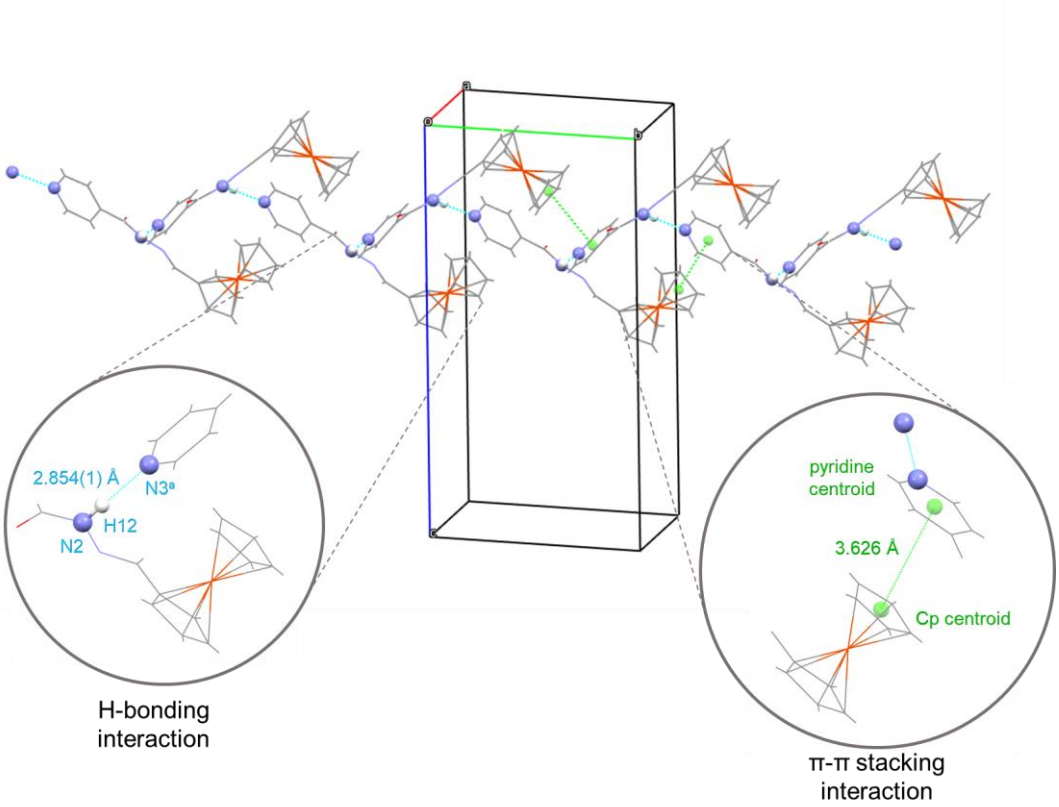

Figure 12. Unit cell packing and intermolecular interactions of **Feizone**. A complete row underneath the linear chain was excluded for the sake of simplification.

For **Ferfurone** (Figure 11b), XRD data show a molecule of methanol (used as solvent in the synthesis) crystallized *per* ligand unit. Free rotation around the C12-C13 and C12'-C13' bonds gives rise to two crystallographic distinct species. However, these structures are just conformers that differ in the relative orientation of the heteroatom of the furan group in relation to the carbonyl oxygen atom and are indistinguishable once the compound is dissolved. Thus, every crystallographic parameter for this ligand is doubled. **Ferfurone** molecules are also in the form of (*E*)-isomers and *anti*-conformations and belong to the orthorhombic system. This time, however, $Z = 4$. The methanol molecules held the structure of both conformers in the same way, with their hydroxyl group (O3–H13 and O3'–H13') acting as a bifurcated H-bonding donor with carbonyls' O1 and O1' and imines' N1 and N1' [O3–H13···O1^{c} 2.913(2) Å, O3'–H13'···O1'^{e} 2.931(2) Å, O3–H13···N1^{c} 3.089(1) Å and O3'–H13'···N1'^{e} 3.077(2) Å]. This hydroxyl group also acts as a H-bonding acceptor for the amines' N2–H12 and N2'–H12' [N2–H12···O3^{b} 2.843(3) Å and N2'–H12'···O3'^{d} 2.848(1) Å]. Simply put, the methanol molecule forms moderate non-conventional bifurcated hydrogen bonds (Steiner, 2002),

acting as donor and acceptor, holding the lattice between the **Ferfurone** molecules by forming two antiparallel linear 1D chains that run across the crystallographic axis *b*. Figure 13 displays the whole panorama of intermolecular interactions in the lattice of **Ferfurone**, and the H-bonding parameters for **Ferfurone** are presented in Table 2.

The only two other papers that cover crystallographic data for **Ferfurone** report the *N*-acylhydrazone syntheses use ethanol as the solvent, recrystallizing it either in a dichloromethane/hexane mixture (Ravindran *et al.*, 2023), or methanol (Gupta *et al.*, 2014). Neither of these works describes any solvent in the crystal structure, even with recrystallization in methanol. Thus, methanol, when employed directly in the synthesis, affected the nature of the crystallization itself, generating a crystal structure unprecedented in the literature. This fact leads to entirely new cell parameters, crystal system and space group compared to those already reported, although the main bond distances and angles do not differ significantly from those in literature (Ravindran *et al.*, 2023). Interestingly, neither one of the two published papers describes the conformation duplicity caused by the rotation on the C12-C13 and C12'-C13' bonds, and they do not appear as two distinct structures, suggesting that the crystallized methanol induces this duplicity in the crystallographic data.

Table 2. H-bonding parameters for **Feizone** and **Ferfurone** ligands.

Feizone				
D–H···A	D–H (Å)	H···A (Å)	D···A (Å)	D–H···A (º)
N2-H12···N3[a]	0.911(1)	1.966(3)	2.854(1)	158.79
Ferfurone				
D–H···A	D–H (Å)	H···A (Å)	D···A (Å)	D–H···A (º)
N2–H12···O3[b]	0.860(1)	2.041(2)	2.843(3)	154.81
O3–H13···O1[c]	0.820(1)	2.332(3)	2.913(3)	128.39
O3–H13···N1[c]	0.820(1)	2.313(3)	3.089(1)	158.14
N2'–H12'···O3'[d]	0.915(1)	1.961(1)	2.848(1)	162.82
O3'–H13'···O1'[e]	0.821(4)	2.428(2)	2.913(2)	120.54
O3'–H13'···N1'[e]	0.821(4)	2.282(4)	3.077(2)	163.38

Symmetry code: a: –x, –½ + y, ½ – z ; b: x, y, z ; c: x, 1 + y, z ; d: x, y, z ; e: x, –1 + y, z

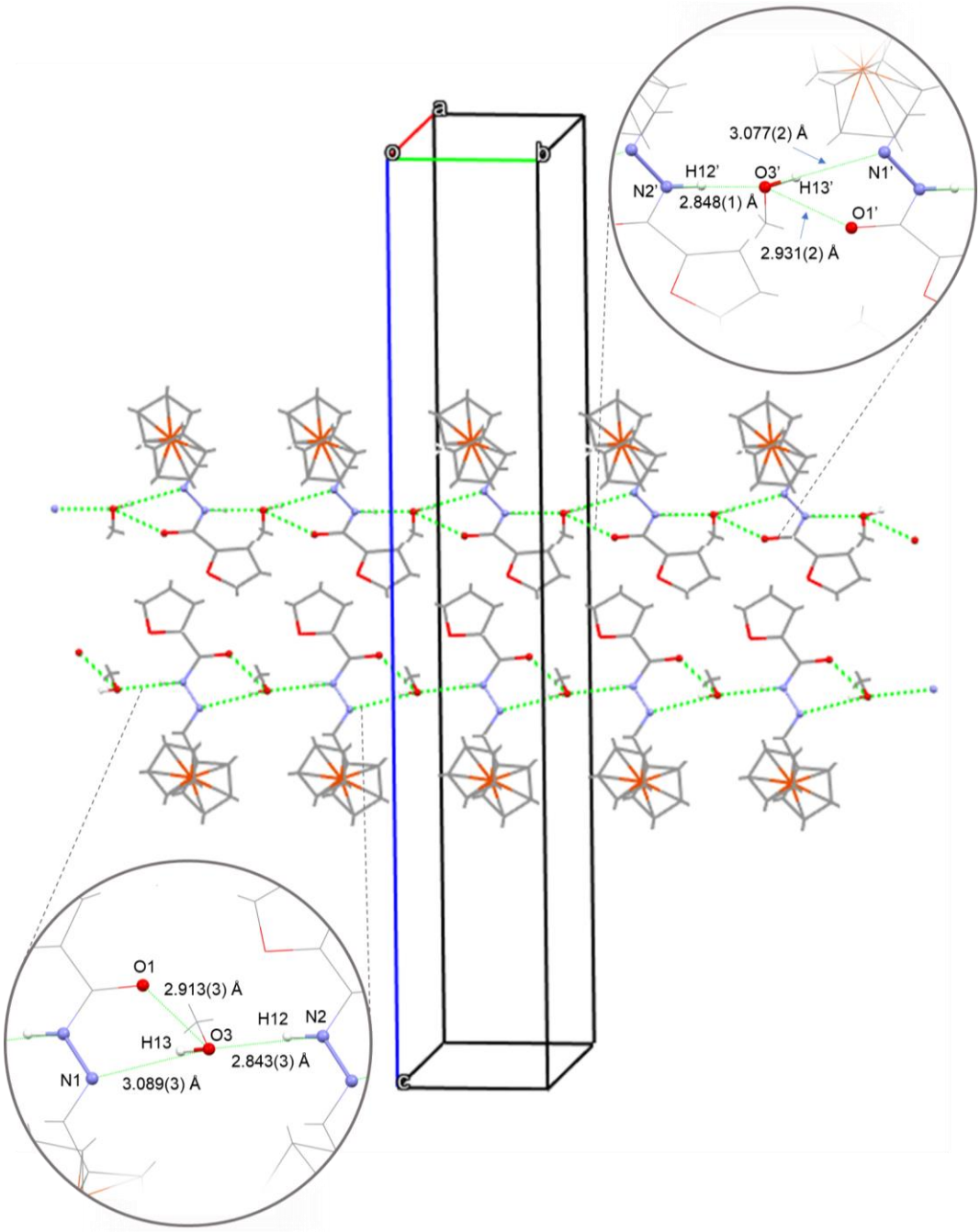

Figure 13. Unit cell packing and intermolecular interactions of **Ferfurone**. The rows above and underneath the two antiparallel linear chains were excluded for the sake of simplification.

5.2.2. Vibrational Spectroscopy

The mid-IR spectra for **Feizone** and **Ferfurone** are shown in Figure 14a and 14b, respectively. The main bands with their assignments between 4000-400 cm^{-1} are given in Table 3. Absorptions were assigned using either the same or very similar molecules for reference on both **Feizone** (Cukierman *et al.*, 2021; dos Santos Filho & de Souza Castro, 2022; Galić *et al.*, 2001) and **Ferfurone** (Gupta *et al.*, 2014; Moura *et al.*, 2023; Ramesh Babu *et al.*, 2014).

Table 3. Assignments for **Feizone** and **Ferfurone** ligands between 4000-600 cm^{-1} in KBr disc at room temperature.

Feizone		**Ferfurone**	
Vibration mode	**Wavenumber**	**Vibration mode**	**Wavenumber**
ν(N–H)	3147 cm^{-1} (w)	ν(N–H)	3207 cm^{-1} (w)
$\nu(C–H)_{azomethine}$	3060 cm^{-1} (w)	$\nu(C–H)_{azomethine}$	3059 cm^{-1} (w)
ν(C=O)	1671 cm^{-1} (s)	ν(C=O)	1652 cm^{-1} (s)
$\nu(C=N)_{azomethine}$	1604 cm^{-1} (m)	$\nu(C=N)_{azomethine}$	1608 cm^{-1} (s)
β(H–N–N) + $\beta(H–C=N)_{azomethine}$	1562 cm^{-1} (m)	β(H–N–N) + $\beta(H–C=N)_{azomethine}$	1571 cm^{-1} (m)
$\nu(C=C)_{pyridine}$ + $\beta(H–C=C)_{pyridine}$	1552 cm^{-1} (m)	$\nu(C=C)_{furan}$	1549 cm^{-1}(m)
$\nu(C=N)_{pyridine}$ + $\nu(C=C)_{pyridine}$	1294 cm^{-1} (s)	$\nu(C–O)_{furan}$	1252 cm^{-1} (m)
$\nu(N–N)_{hydrazone}$	896 cm^{-1} (w)	$\delta(O–C–H)_{furan}$	1186 cm^{-1} (w)
$\nu(C=N)_{pyridine}$	682 cm^{-1} (w)	$\nu(N–N)_{hydrazone}$	930 cm^{-1} (w)

Band intensity: w: weak; **m:** medium; **s:** strong.

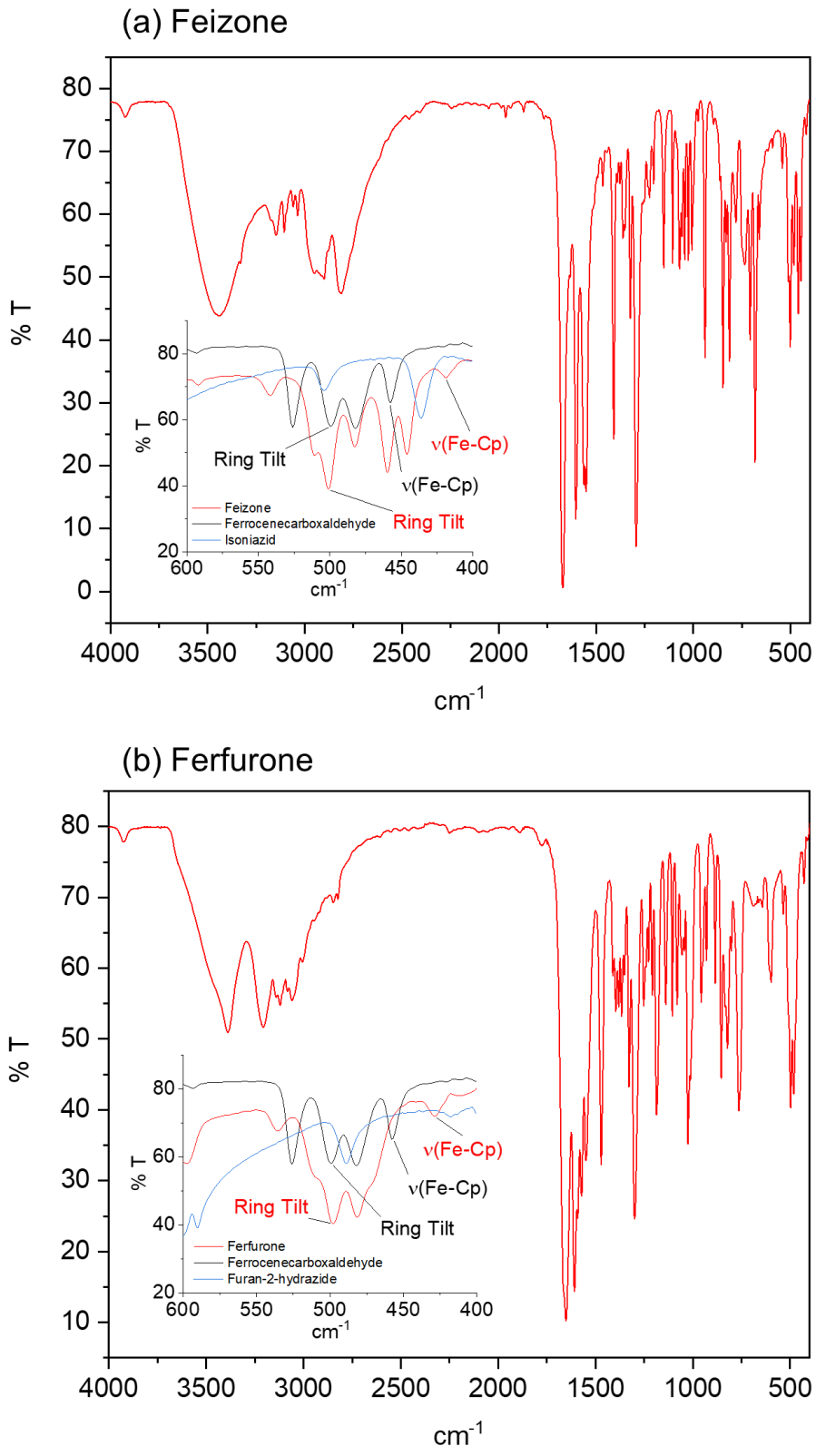

Figure 14. Mid-IR spectra of **Feizone** (a) and **Ferfurone** (b) in KBr pellets at room temperature are shown in red. *Inset*: magnification of the 600-400 cm^{-1} region and selected band attribution. The spectra of the precursors isoniazid (blue in a), furan-2-carbohydrazide (blue in b), and ferrocenecarboxaldehyde (black) were included for the sake of comparison.

The N–H bands are very characteristic, often broad bands in usual amine systems (Silverstein *et al.*, 2014). However, in *N*-acylhydrazones they appear as thinner bands on both spectra, at 3147 cm^{-1} and 3207 cm^{-1} for **Feizone** and **Ferfurone**, respectively. Another very characteristic band is the ν(C=O) which usually is the most noticeable band in the spectrum, appearing in the range of 1800-1600 cm^{-1} (Silverstein *et al.*, 2014). This bond has a distinguishably higher dipole momentum than other usual bonds in organic chemistry, explaining its classic intense absorption (Silverstein *et al.*, 2014). As expected, both ligands show ν(C=O) as the strongest band in their respective spectra, at 1671 cm^{-1} for **Feizone** and 1652 cm^{-1} for **Ferfurone**. This band is slightly less energetic for the ligand **Ferfurone**, probably due to stronger electron withdrawal effects from the furan group.

The respective ν(C=N) bands of the azomethine group indicate the successful attainment of the product, appearing with less intensity and both very close to each other (1604 cm^{-1} for **Feizone** and 1608 cm^{-1} for **Ferfurone**), which was expected due to the chemical environment similarity. Other individual bands for these ligands are the pyridine vibration modes [ν(C=C) at 1552 cm^{-1}; ν(C=N) at 1294 cm^{-1}; ν(C=N) at 682 cm^{-1}] for **Feizone** and the furan vibration modes [ν(C=C) at 1549 cm^{-1}; ν(C–O) at 1252 cm^{-1}] for **Ferfurone**.

As mentioned before, the metal-ligand bands for the ferrocene fraction can be studied apart from the rest. These bands are found in the 600-400 cm^{-1} range, as contemplated in these spectra. As such, some additional assignments were made aiming to enrich the discussion on the nature of metal-ligand bonding. The *insets* in Figure 14 contain a cutout in this range for both ligands, superposed with the spectra of their respective precursors for comparison. To make the assignments, full comparisons were made with ferrocene-substituted IR spectra (Appel *et al.*, 2014; Diana *et al.*, 1997; Phillips *et al.*, 1988). Looking at ferrocenecarboxaldehyde and the ligands, the Ring Tilt band stays practically unchanged in both cases, whilst the ν(Fe-Cp) absorption is shifted to lesser frequencies in the hydrazones. This phenomenon was evidenced by the direct impact of the substituent's weight on this band in different ferrocene-containing structures found in the literature (Phillips *et al.*, 1988): the heavier the substitute, the lesser the frequency of this stretch.

5.2.3. Thermogravimetry

Thermal decomposition of the ligands, evaluated by the thermogravimetric technique, was performed to confirm if the characteristics seen in crystallographic analyses extend to the bulk product. This is useful mainly for studying the behavior of compounds below 200 ºC, as thermal decompositions in this temperature range are related to the presence of solvent in the crystal network. Moreover, since the ligands in this work are already iron complexes, a stable residue at the end of the TG curve is associated with the quantities of metal present in the samples. Both thermogravimetric curves are shown in Figure 15.

There are three main weight losses for **Feizone**, being the second and the third ones probably multistep processes, all attributed to organic decompositions, which start at 237 ºC and end in a stable residue from 612 ºC on, with 23.1% of the original mass. For a molecular weight of 333.17 g mol^{-1}, as evaluated in crystallography, the calculated percentage for a residue constituted of FeO is 21.6%, and for Fe_2O_3, 24.0%, suggesting a mixture of both oxides as the final degradation product.

For **Ferfurone**, there are also three main weight losses attributed to organic decompositions, which start at 214 ºC and end in a stable residue from 481 ºC on, with 23.6% weight. This indicates that this hydrazone is a little bit thermically less stable than **Feizone**. For a predicted monomer molecular weight of 354.18 g mol^{-1}, the calculated percentage for a residue of FeO is 22.3%, and for Fe_2O_3 is 24.8%, suggesting again a mixture of both oxides. The absence of decomposition in both curves below 200 ºC may suggest that both compounds do not present any solvent crystallized within their structures. However, the single crystal XRD analysis of **Ferfurone** clearly shows a methanol molecule *per* ligand within its solid packing. This solvent also appears in the ^1H NMR spectrum (shown below), indicating that the methanol is probably released during the first or second decomposition step.

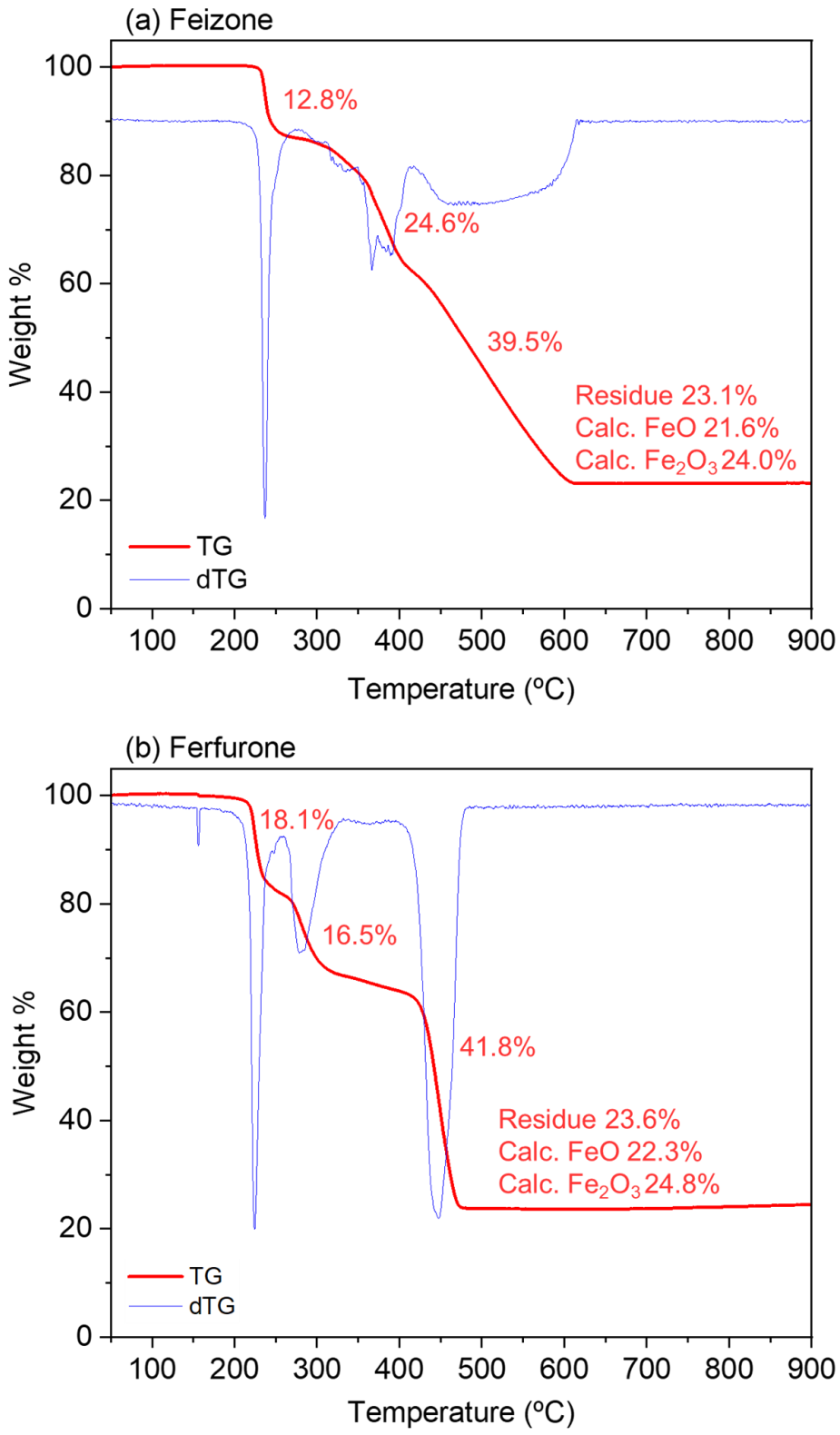

Figure 15. Thermogravimetric curves of **Feizone** (a) and **Ferfurone** (b) ligands between 50-900 ºC, under N_2 flux and heat rate of 10 ºC min^{-1} (red) and their first derivative (blue). The weight percentage variation was added in red and, at the end, the weight percentage of the final stable residue along with its theoretical calculated value.

5.2.4. Emission Spectroscopy

This assay consists of elemental percentage quantification of iron through inductively coupled plasma optical emission spectroscopy (ICP-OES), with the aim of further confirm the bulk characteristics seen in XRD, as well as of compare the Fe percentage values obtained with the ones calculated from the proposed formulae of the complexes. The assays resulted in a percentage of Fe of 17.0% for **Feizone** (calculated: 16.8%) and 17.8% for **Ferfurone** (calculated: 17.3%). These results are going to be further explored and discussed along with the emission spectroscopy results from the complexes of these ligands.

5.2.5. Hydrogen Nuclear Magnetic Resonance (^{1}H NMR)

Figure 16 displays the ^{1}H NMR spectra for both ligands, highlighting the assigned atoms in each structure, and Table 4 shows more complete NMR data (chemical shifts, signal multiplicity, integration and coupling constants).

Although free iron(II) ions are paramagnetic, which would heavily interfere with and incapacitate a proper ^{1}H NMR analysis (Hore, 2015), by considering the molecular orbital diagram of ferrocene (Bhatt, 2016), one can see that its electrons are in a diamagnetic, low-spin d^6 configuration, making it possible to register and analyze the ^{1}H NMR spectra perfectly.

A relevant signal for both compounds is the azomethine hydrogen, confirming the obtention of these ligands. Their chemical shifts are 8.31 ppm for **Feizone** and 8.27 ppm for **Ferfurone**. Azomethine shifts values in this range indicate the (*E*)-isomer as the one present in solution, as was observed in the crystallographic data. Otherwise, the (*Z*)-isomer should be observed at a lower field due to an increased electron density related to the HC=N double bond (Fernández-Palacios *et al.*, 2023). Another relevant signal for these ligands is the heavily de-shielded amide hydrogen, assigned in 11.74 and 11.50 ppm for **Feizone** and **Ferfurone**, respectively. This unmistakable signal was used in both cases to calibrate integration, due to its well-defined, secluded position in the spectra.

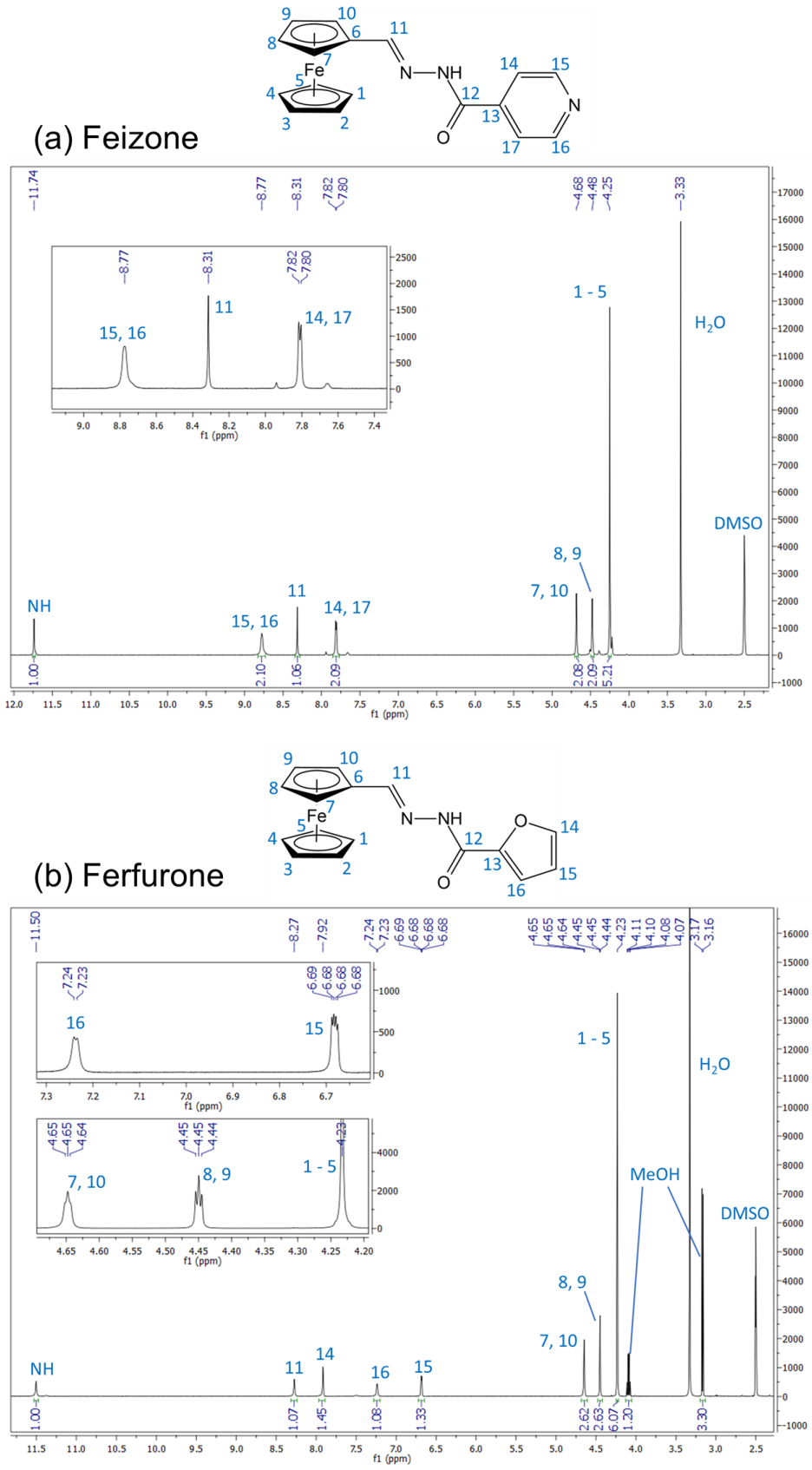

Figure 16. ^{1}H NMR (400 MHz) spectrum of **Feizone** (a) and **Ferfurone** (b), in DMSO-d_6, at room temperature. Above each spectrum, the structure of these ligands is shown with their respective hydrogen numeration.

Table 4. ^{1}H NMR data for **Feizone** and **Ferfurone** in DMSO-d_6 at room temperature.

Feizone		**Ferfurone**	
^{1}H	**δ (ppm)**	**^{1}H**	**δ (ppm)**
N–H	11.74 (s, 1H)	N–H	11.50 (s, 1H)
15, 16	8.77 (s, 2H)	11	8.27 (s, 1H)
11	8.31 (s, 1H)	14	7.92 (s, 1H)
14, 17	7.81 (d, 2H, ^{3}J = 8.0 Hz)	16	7.24 (d, 1H, ^{3}J = 4.0 Hz)
7, 10	4.68 (s, 2H)	15	6.68 (dd, 1H, ^{3}J = 3.6 Hz, ^{5}J = 1.6 Hz)
8, 9	4.48 (s, 2H)	7, 10	4.65 (t, 2H, ^{3}J = 1.6 Hz)
1 - 5	4.25 (s, 5H)	8, 9	4.45 (t, 2H, ^{3}J = 2.0 Hz)
–	–	1 - 5	4.23 (s, 5H)
		MeOH	4.09 (q, 1H, ^{3}J = 5.2 Hz) 3.17 (d, 3H, ^{3}J = 5.2 Hz)

s: singlet, d: doublet, dd: doublet of doublets, t: triplet, q: quartet.

For **Feizone**, the pyridine-related signals appear as a broad singlet centered at 8.77 ppm and a doublet in 7.81 ppm. For this ligand, the signals in 4.68 ppm and 4.48 ppm correspond to the four hydrogens on the substituted ring of the ferrocene group, appearing more upfield those hydrogens closer to azomethine. The signal corresponding to the unsubstituted cyclopentadienyl ring hydrogens is at 4.25 ppm. Meanwhile, for the **Ferfurone** ligand, the substituted ring hydrogens are found in 4.65 ppm (2H) and 4.45 ppm (2H), also being more upfield the hydrogens closer to azomethine. Hydrogen atoms on the unsubstituted cyclopentadienyl ring appear all together at 4.23 ppm. Regarding the furan group on **Ferfurone**, the signal of the hydrogen closest to the oxygen appears as a singlet at 7.92 ppm, the intermediate one as a doublet of doublets at 6.68 ppm, and the most distant one as a doublet at 7.24 ppm. The disorder around the furan group gives rise to a different multiplicity of signals for this ligand, such as the triplets for the upper ring on ferrocenyl, and more importantly, the doublet of doublets in 6.68 ppm. Still regarding **Ferfurone**, two signals, a quadruplet at 4.10 ppm and a doublet at 3.17 ppm are found on the spectrum, which were compared to the literature and

attributed to the residual signal of methanol in DMSO-d_6 (Babij *et al.*, 2016). This methanol molecule is present within the **Ferfurone** crystal structure and was previously discussed.

As the signal multiplicity suggests, nuclear spin-spin coupling from adjacent hydrogens causes NMR lines to split into smaller signals with well-defined relative intensities and spacings. The multiplicity for n equivalent spin-½ nuclei, such as ^{1}H, is given by n+1, explaining the multiplicity found on the spectra (Hore, 2015). Meanwhile, chemical shifts happen because the magnetic field actually experienced by the nucleus differs slightly from the external field, which induces the electrons to circulate within their orbitals, generating small magnetic fields in the opposite direction to the original magnetic field (Hore, 2015). Thus, this nucleus is shielded from the external field by its surrounding electrons. When the electrons are stripped from the hydrogen atoms, they are de-shielded, usually by more electronegative elements, and the signal appears more downfield in the spectrum (Hore, 2015). For this reason, the signal for the hydrogens on the cyclopentadienyl ring closer to the azomethine appears more downfield, due to the stripping of electrons caused by this group. Similarly, this phenomenon explains the hydrogen from the aroylhydrazone (amide) group being the most downfield, due to the de-shielding effect caused by the proximity to a more electronegative atom.

5.2.6. Cyclic Voltammetry

The cyclic voltammetry for both ligands (1.0 mmol L^{-1}) at different scan rates (50 to 500 mV s^{-1}) is shown in Figure 17. The solvent was a 1:1 methanol/water mixture containing NaCl 0.1 mol L^{-1} as the supporting electrolyte. The first step in the characterization by cyclic voltammetry is the determination of the reversible (or not) nature of the process since every law that reigns this experiment depends on it. The difference between reversible, irreversible, and *quasi*-reversible processes is dictated by electrode kinetics (Compton & Banks, 2007). A fast enough electrode reaction is considered reversible, a slow reaction is irreversible, and, finally, *quasi*-reversible processes are in-between. This electrode kinetic depends heavily on the diffusion layer thickness, which is dictated by the scan rate (v) set in the experiment. Thus, every reaction has a reversible limit, in which, if the scan rate is fast enough, the process will be irreversible (Compton & Banks, 2007).

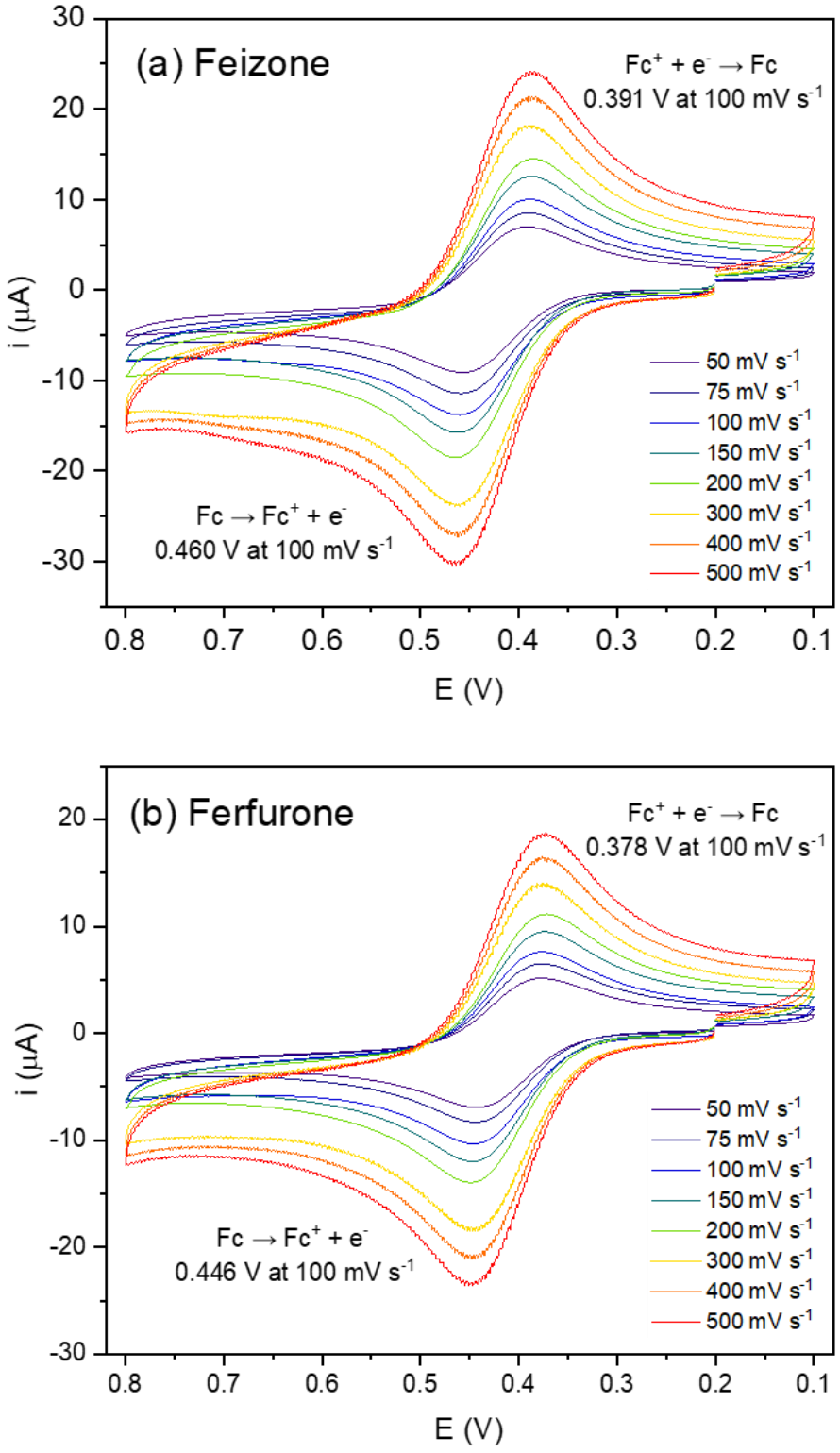

Figure 17. Cyclic voltammogram of **Feizone** (a) and **Ferfurone** (b) in 1:1 a methanol/water mixture containing 0.1 mol L^{-1} NaCl, at different scan rates. Here, Fc represents the ferrocenyl group in these ligands. Potentials *vs.* Ag/AgCl 3 mol L^{-1} KCl electrode.

However, ‘fast’ and ‘slow’ are relative terms and do not suffice to determine the parameters in which a reaction is reversible or not. The rate of electron transfer kinetics is measured by the standard electrochemical rate constant, k^0, which refers to the time needed for the electroactive species to arrange for the electron transfer process. It does not relate to the electron transfer rate itself, as it actually happens in a tremendously faster manner, with rates in the order of 10^{-16} s (Trachioti *et al.*, 2023). Additionally, the rate of mass transport, m_T, is measured by the diffusion coefficient (D) and the size/thickness of the diffusion layer (δ):

$$m_T = \frac{D}{\delta} \qquad 1$$

with layer thickness (δ) and time (t) given by:

$$\delta \sim \sqrt{Dt}\,, \quad t \sim \frac{RT}{Fv}\,, \qquad so:$$

$$m_T \sim \sqrt{\frac{FDv}{RT}} \qquad 2$$

valid for cyclic voltammetry experiments (Compton & Banks, 2007), where *v* is the corresponding scan rate and D is the diffusion coefficient, which we can evaluate through the Nicholson-Shain equation (Equation 3, parameters in Table 5), which depends on the current peak at forward scan (i_{peak}) (Bogdan *et al.*, 2014).

$$D = \frac{\left(i_{peak}\right)^2 RT}{(0.4463\, nc_0AF)^2 nFv} \qquad 3$$

Table 5. Nicholson-Shain equation parameters, showing standard units and, when it applies, the constant values in parentheses.

Equation parameters
D: Diffusion coefficient ($cm^2\ s^{-1}$)
i_{peak}: Peak current (A)
R: Ideal gas constant (8.314 $J\ mol^{-1}\ K^{-1}$)
T: Temperature (298 K)
n: Number of electrons in the process
c_0: Bulking concentration ($mol\ L^{-1}$)
A: Working electrode surface area ($\pi\ 0.15^2\ cm^2$)
F: Faraday constant ($9.6485\times10^4\ s\ A\ mol^{-1}$)
v: Scan rate ($V\ s^{-1}$)

Consequently, calculating the diffusion coefficient D based on i_{peak} for each ligand at 1.0 $mmol\ L^{-1}$ and scan rate of 0.1 $V\ s^{-1}$, considering a one-electron process, and the experimental cathodic i_{peak} was 10.0 μA for **Feizone** and 7.62 μA for **Ferfurone**. Thus,

$$D_{Feizone} = 2.79 \times 10^{-6}\ cm^2\ s^{-1}$$

$$D_{Ferfurone} = 1.61 \times 10^{-6}\ cm^2\ s^{-1}$$

These values match the magnitude order of those described for ferrocene in multiple solvents (Tsierkezos, 2007).

As mentioned before, the distinction between fast and slow electrode kinetics is crucial in order to understand the reversibility of a process. It is given by the relation between the previously mentioned rate of mass transport m_T and k^0, in the following manner (Compton & Banks, 2007):

$$k^0 \gg m_T \quad (reversible)$$

$$k^0 \ll m_T \quad (irreversible)$$

In this sense, the transition between the reversible and irreversible limits can be followed through a new parameter, Λ:

$$\Lambda = \frac{k^0}{m_T} = \frac{k^0}{\sqrt{\frac{FDv}{RT}}} \qquad 4$$

The original, classical paper by Matsuda & Ayabe (1955) that introduces Λ also suggested ranges for classification, assuming standard parameters and 298 K:

Reversible:

$$\Lambda \geq 15, \;\; k^0 \geq 0.3v^{1/2}\ cm\ s^{-1}$$

quasi-reversible:

$$15 > \Lambda > 10^{-3}, \;\; 0.3v^{1/2} > k^0 > 2 \times 10^{-5}v^{1/2}\ cm\ s^{-1}$$

irreversible:

$$\Lambda \leq 10^{-3}, \;\; k^0 \leq 2 \times 10^{-5}v^{1/2}\ cm\ s^{-1}$$

Taking it all into consideration, by fitting experimental voltammograms of varying scan rates to give different Λ values, it becomes possible to evaluate k^0, the standard electrochemical rate constant. Consequently, it also becomes possible to determine the reversibility of the process at a specific scan rate, hence the suggested ranges mentioned. Plotting the module of the difference between the potential of anodic and cathodic peaks (ΔEpp) with different log *v* gives raise to two different expected behaviors. At the reversible range (low scan rates), ΔEpp is given by:

$$\Delta E_{pp} = 2.218\ \frac{RT}{nF}$$
$$\Delta E_{pp} = 57\ mV\ (298\ K) \qquad 5$$

while at the irreversible range (high scan rates), the peak potential, E_p, is given by:

$$E_p = \frac{-RT}{\alpha F}\ln(v) + constant,$$
$$so\ that\ \Delta E_{pp} \gg 2.218\ \frac{RT}{F} \qquad 6$$

Note that Equation 5, regarding the reversible range, does not depend on the scan rate (v). Within this plot, the intersection point between the two fittings, regarding both the reversible and irreversible ranges, is exactly the intermediate between reversible and irreversible limits. As so, this is the point where $k^0 = m_T$, and $\Lambda = 1$ (Compton & Banks, 2007).

$$\Lambda = 1, \qquad so\ k^0 = m_T\ , \qquad k^0 = \sqrt{\frac{FDv}{RT}} \tag{7}$$

The plot with ΔEpp varying along log v can be found for both ligands in Figure 18. Λ is equal to 1 for the scan rates of 1.7 V s^{-1} and 1.8 V s^{-1} for **Feizone** and **Ferfurone**, respectively. So, solving Equation 7 by using these scan rates and previously calculated diffusion coefficient values, we get:

$$k^0{}_{Feizone} = 1.37 \times 10^{-2}\ cm\ s^{-1}$$

$$k^0{}_{Ferfurone} = 1.39 \times 10^{-2}\ cm\ s^{-1}$$

These values for k^0 allow a more thorough analysis of the reversibility limits using the above-stated reference values for each kind of process.

The reversible limits of the process are:

$$15\ > \Lambda\ > 10^{-3}\ , \qquad as\ \frac{k^0}{\sqrt{\frac{FDv_i}{RT}}} = \Lambda_i\ , \qquad so$$

$$v_{lim} \sim \frac{RT}{FD}\left(\frac{k^0}{\Lambda}\right)^2 \tag{8}$$

Following through, for **Feizone**:

$$the\ process\ is\ reversible\ when: \quad v_{lim,rev.} \leq 7.63 \times 10^{-3}\ V\ s^{-1}$$
$$and\ irreversible\ when:$$
$$v_{lim,irrev.} \geq 1.72 \times 10^{6}\ V\ s^{-1}\ (no\ physical\ application).$$

And for **Ferfurone**:

$$the\ process\ is\ reversible\ when: \quad v_{lim,rev.} \leq 7.85 \times 10^{-3}\ V\ s^{-1}$$
$$and\ irreversible\ when:$$
$$v_{lim,irrev.} \geq 1.77 \times 10^{6}\ V\ s^{-1}\ (no\ physical\ application).$$

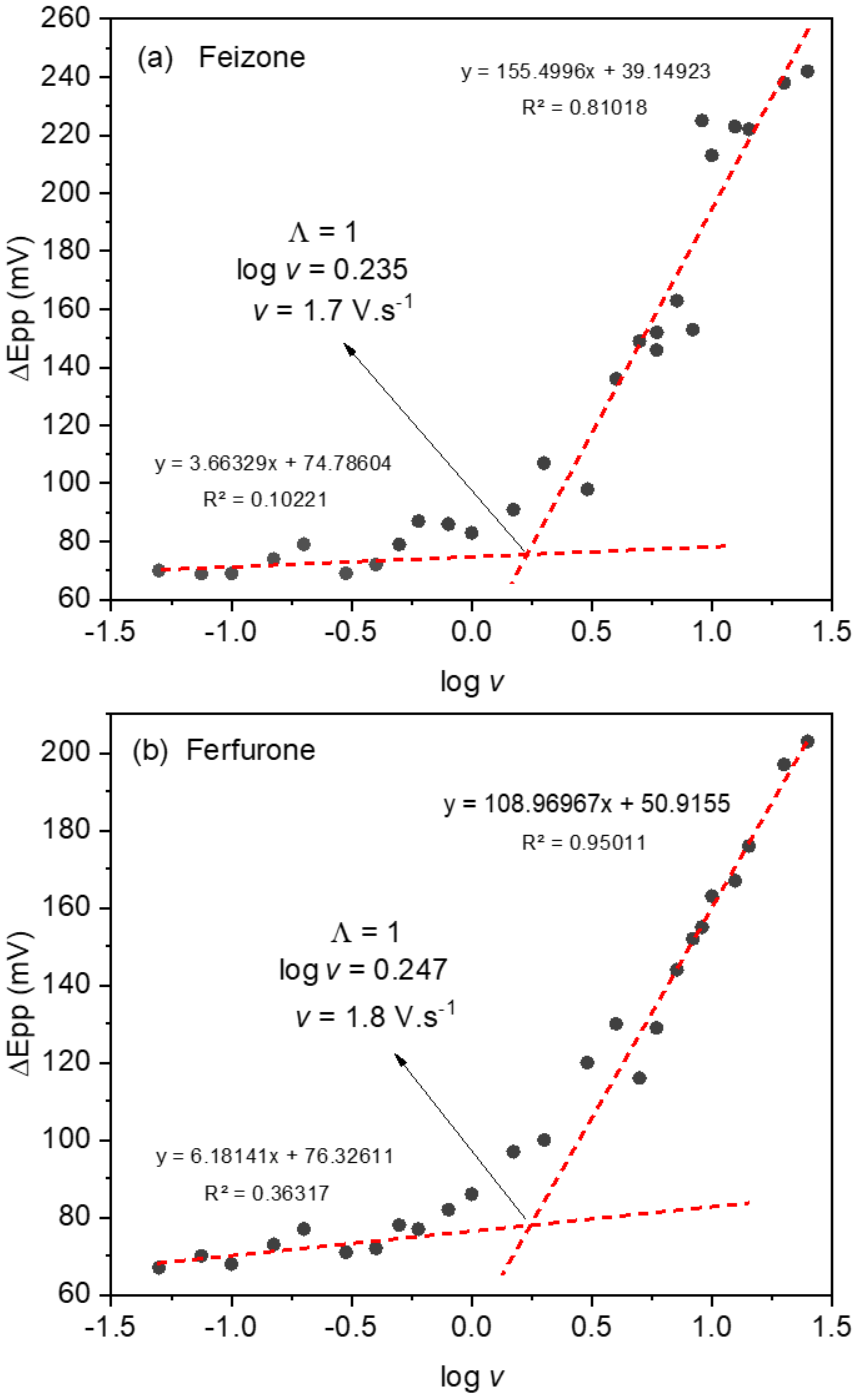

Figure 18. Δ*E*pp vs. log *v* plot for **Feizone** (a) and **Ferfurone** (b), indicating the linear fittings for the respective reversibility limits.

These limits point out that our working scan rates (from 0.05 to 0.5 V s^{-1}), as seen in Figure 17, are in the range of *quasi*-reversible processes for these systems. The increasing values for the difference in cathodic and anodic peak potentials as the scan rates rise also indicate a *quasi*-reversible pattern, corroborated by CV experiments for the same or similar species in the literature (Gupta *et al.*, 2014).

Since we know exactly the scan rate range in which a reversible process drives the reaction, it becomes possible to stipulate some parameters for this reaction, such as the number of electrons involved and the standard potentials (Compton & Banks, 2007). At the scan rate of 0.005 V s^{-1} (a value within the reversible regime for both ligands), **Feizone** potential peaks are E_{pc} = 0.384 and E_{pa} = 0.468 V, and **Ferfurone** peaks are E_{pc} = 0.376 and E_{pa} = 0.448 V.

For a reversible process:

$$\Delta E_{pp} = 2.218\,\frac{RT}{nF}\;; \quad n = \;2.218\,\frac{RT}{\Delta E_{pp}\,F} \qquad 9$$

So, for **Feizone**:

$$n = 0.7 \rightarrow n \sim 1\ electron\ process.$$

And for **Ferfurone**:

$$n = 0.8 \rightarrow n \sim 1\ electron\ process.$$

Moreover, knowing the reversible limits of the process in both ligands, it is possible to evaluate the standard potential (E^0) for the respective reactions from the Nernst equation (Elgrishi *et al.*, 2018). This equation relates the measured potential (E) with E^0 in the form:

$$E = E^0 - \frac{RT}{nF} ln \frac{[Red]}{[Ox]}, \qquad 10$$

So, if [Red] = [Ox],

$$ln \frac{[Red]}{[Ox]} = 0$$

$$and \quad E = E^0\,.$$

The point in which the concentration of reduced and oxidized species are the same is found midway between the anodic and cathodic peaks ($E_{½}$) (Compton & Banks, 2007). Thus, the equation becomes:

$$E_{½} = \frac{E_{peak,red} + E_{peak,ox}}{2} = E^0 \qquad 11$$

However, it is important to mention that the determination of the reversible limits of an electrochemical reaction in the cyclic voltammetry is more accurate for smaller and simpler molecules. The results taken in consideration here are merely an approximation of the real parameters that drives these reactions. Thus, we can't affirm the $E_{½}$ is strictly equal to the E^0 for these reactions. Also, note that an Ag/AgCl 3.0 mol L^{-1} KCl electrode (silver chloride electrode) was used as the reference electrode; so, all potentials measured so far are against this reference. The potential of the silver chloride electrode against the standard hydrogen electrode (or SHE) is E = +0.22249 V (Standard Potential of the Silver-Silver Chloride Electrode, 1978). Thus, for the reversible scan rate of 0.005 V s^{-1}:

$E_{½\ Feizone} = 426\ mV$ *vs.* Silver Chloride Electrode;

$E_{½\ Feizone} = 648\ mV$ *vs.* SHE.

$E_{½\ Ferfurone} = 412\ mV$ *vs.* Silver Chloride Electrode;

$E_{½\ Ferfurone} = 634\ mV$ *vs.* SHE.

The $E_{½}$ potentials estimations for these ligands are higher than the standard potential of ferrocene (560 mV *vs.* SHE), first described by Page & Wilkinson (1952). These increased potentials in the presence of the electronegative groups pyridine and furan suggest a strong electronic interaction between both hydrazone substituents. By withdrawing electron density from ferrocene, hydrazone moieties in the ligands make them more difficult to oxidize, thus explaining the observed raised potentials. This phenomenon was explored in similar substituted ferrocenyl groups as well, by Gupta *et al.* (2014) and Noh *et al.* (1999).

5.2.7. Square-Wave Voltammetry

Square-wave voltammetry is a form of differential pulse voltammetry. It is a large-amplitude differential technique that combines a square wave with a staircase potential applied to a working electrode. This method achieves high sensitivity due to the minimal influence of non-faradaic currents. Consequently, this technique is widely used as an electrochemical measurement technique in diverse fields such as food science, medicine, and environmental research (Tolun & Altintas, 2023).

In this work, square-wave voltammetry was applied to study the interaction between the ligands and the $A\beta_{1\text{-}40}$ peptide in low concentrations. As such, the characterization of the voltammetric profile of these ligands in the same conditions used for the peptide-involving experiment was performed.

Anodic and cathodic scans reveal two electrochemical processes, with the first one associated with the ferrocenyl redox couple, appearing at nearly the same potential peaks, with E_{peak} of +0.383 V and +0.369 V for **Feizone** and **Ferfurone**, respectively. These potentials match the $E_{½}$ observed in cyclic voltammetry for both ligands, as expected. Another electrochemical process appears at a higher potential. Since the blank sample voltammogram, containing only the buffer solution, shows no electrochemical activity in this potentials' range, this must be a ligand-related process, indicating another redox couple present in the medium. Note that these waves do not appear in cyclic voltammetry assays, as discussed in the previous section, probably due to the lower currents involved. At a first glance, analyzing the cathodic scanning alone displayed in Figure 19a, this process could be associated with the presence of ferrocenecarboxaldehyde, detected at around +0.52 V. This precursor could be produced either by the hydrolysis of the ligands or impurity excess from the synthesis. However, both samples used in the experiments are derived from recrystallization and constitute very pure, crystalline products. Following along, the anodic scanning of ferrocenecarboxaldehyde still presents a potential at around +0.52 V. However, for ligands **Feizone** and **Ferfurone,** the second anodic waves appear at a very different potential: around +0.67 V, being much more apparent for **Ferfurone** (Figure 19b). Usually, square-wave voltammograms show the $E_{½}$ in either anodic or cathodic scanning. However, this is only true for reversible and *quasi*-reversible processes. For irreversible processes

in square-wave voltammetry, as in this case, the redox couple can appear as separate potentials depending on the scanning direction. This potential distinction on anodic scanning leads to the conclusion that this second electrochemical reaction is not related to ferrocenecarboxaldehyde. Later, the cyclic voltammetry profile of these ligands will be shown to be dependent on the pH, not only by shifting the ferrocenyl process, but also by the appearance of a completely new irreversible electrochemical wave. This process is very close to the potential seen in square-wave voltammetry, and we hypothesize it is probably related to an irreversible electrochemical reaction of the hydrazone moiety, perhaps connected to its iminolization, which occurs in a basic medium.

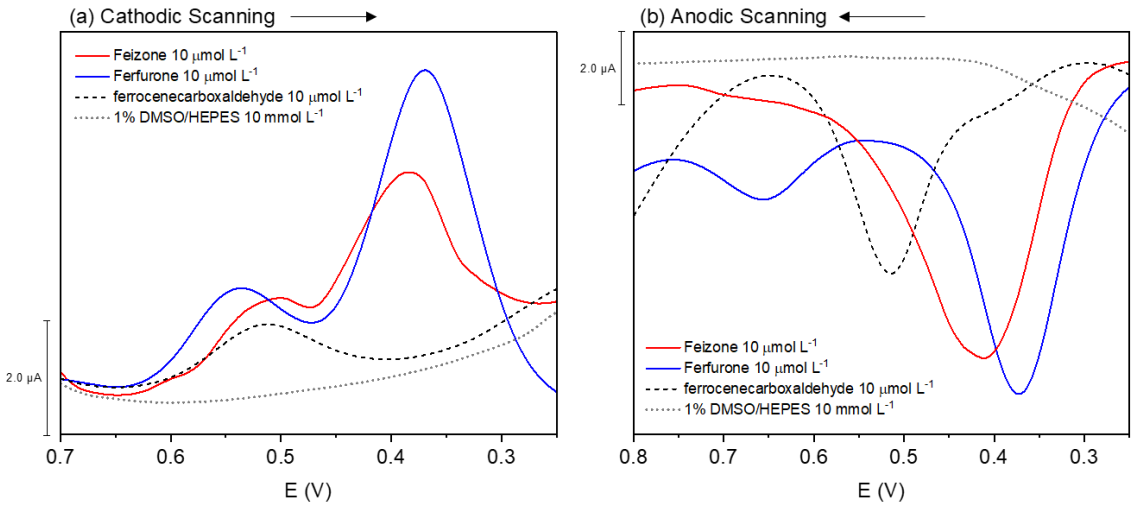

Figure 19. Square-wave voltammogram of **Feizone** (red), **Ferfurone** (blue), and ferrocenecarboxaldehyde (black dashed line) at 1% DMSO/HEPES 10 mmol L^{-1} pH 7.4 buffer with NaCl 0.1 mol L^{-1} (grey dotted line) at 1 mV step. Potentials *vs.* Ag/AgCl 3 mol L^{-1} KCl electrode.

5.3 Syntheses and characterization of complexes

Zinc(II) and copper(II) complexes of **Feizone** and **Ferfurone** ligands were synthesized with methanol. Attempting to react zinc with these ligands without adding base didn't yield any product, as confirmed by ICP-OES analysis of the final residue. For this reason, the subsequent zinc(II) complexes' reactions were carried out under reflux for 4 hours by adding 1 molar equivalent of a strong base, NaOH,

to force the deprotonation of the hydrazone, in order to raise its coordination ability. On the contrary, the copper(II) complexes form more rapidly, at room temperature, in 2 hours, due to a higher coordination kinetic nature of this metal compared to zinc (Lincoln, 2005; Taube, 1970). This phenomenon suggests these ligands have selectivity for copper(II) ions under biological conditions, which can be very useful since zinc(II) ions act as neurotransmitters and have increased concentration in the brain in a free, non-coordinated form (Frederickson *et al.*, 2005).

Thus, for **Feizone**, the reaction with $ZnCl_2$ resulted in a bright red precipitate, obtained with a yield of 43%. This complex, named **Feizone-Zn** was filtered, dried, and properly isolated for characterization. Still regarding the same ligand, a purple precipitate was formed in the reaction with $Cu(NO_3)_2 \cdot 3H_2O$, named **Feizone-Cu**, also filtered and dried, obtained with a reaction yield of 37%. Both complexes were characterized only in the solid state due to solubility problems.

For **Ferfurone**, the reaction with $ZnCl_2$ resulted in a brighter red solution, which was impossible to crystallize or precipitate. After drying it completely, we attempted to recrystallize it with different solvents and struggled to either dissolve the residue or obtain a purified product. For this reason, **Ferfurone-Zn** couldn't be characterized. On the other hand, reaction with $Cu(NO_3)_2 \cdot 3H_2O$ at a 2:1 ligand-to metal stoichiometry, afforded a dark red solution which, after resting, crystallized after about 80% of the solvent was evaporated. This process resulted in tiny crystals, which were filtered, dried, and characterized. This compound received the name **Ferfurone-Cu**, and was obtained with a yield of 9%. Although it, unfortunately, was not suitable for a complete crystallographic characterization, the molecular structure was partially determined by XRD, and it is presented in Figure 20.

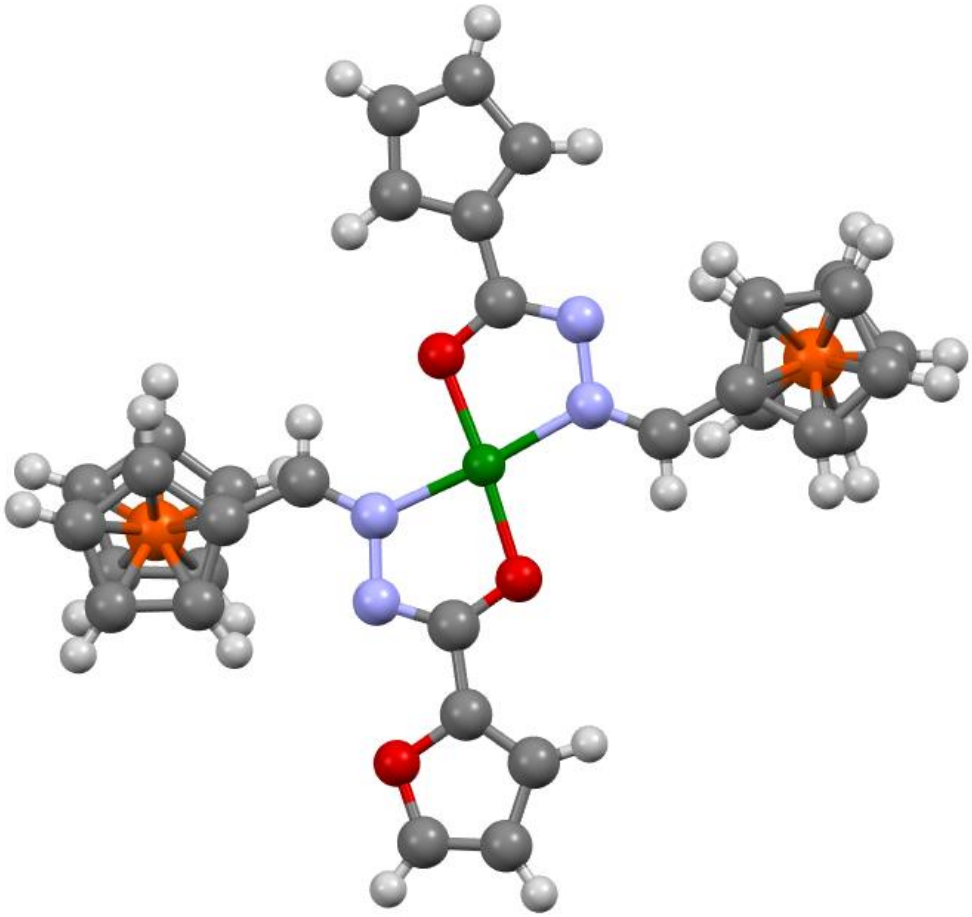

Figure 20. Partial structure representation of **Ferfurone-Cu** as determined by XRD. Green sphere represents the Cu^{2+} ion and the orange ones, Fe^{2+}.

In this structure, copper centers have a coordination number of 4, presenting a square geometry. Each **Ferfurone** unit act as a bidentate ligand through their azomethine nitrogen and carbonyl oxygen, forming a five-membered chelate ring structure. Interestingly, the hydrazone appears as a (*Z*)-isomer, which is expected to be less stable than the (*E*)-isomer counterpart. Probably this isomer is forced during crystallization for a more stable crystalline lattice structure. Note that the methanol molecule present in the ligand's crystalline structure is absent here. Moreover, in the absence of counter-ions in this complex's structure, each ligand must have suffered deprotonation in the amide nitrogen, coordinating copper(II) in the form of negative iminolate ligands.

The description of zinc(II) coordination compounds for these ligands is very scarce in the literature. Yunyin *et al.* (1998) reported the 2:1 **Feizone-Zn** complex

along with very few properties. No report of a zinc complex with **Ferfurone** was found whatsoever. The literature is richer regarding copper(II) complexes of these ligands, reporting 2:1 ligand-to-copper stoichiometry compounds for both ligands (Patil *et al.*, 1982; Qingbao *et al.*, 1994; Yunyin *et al.*, 1998). Copper(II) complexes with triphenyl phosphate and one of these ligands were also reported regarding their DNA interaction and cytotoxic activity (Krishnamoorthy *et al.*, 2012; Sathyadevi *et al.*, 2012). None of the cited works provided a voltammetry study around these complexes, neither directly dissolving the prepared complexes nor a complexation study measuring the voltammogram of complexes generated *in situ*.

5.3.1. Vibrational Spectroscopy

The infrared spectra of copper(II) and zinc(II) complexes (Figure 21) show significant changes compared to the free ligands. The main IR frequencies and their assignments are listed in Table 6. The ν(N–H) and ν(C=O) vibration modes are absent in the complexes, evidencing ligand deprotonation and metal coordination as iminolates. Moreover, the ν(C=N) band from azomethine presents a decreased frequency, whereas ν(N–N) absorption has its energy increased upon coordination, maybe due to generalized electronic delocalization in the negatively charged ligand. Two new vibration modes appear in the complexes: ν(C=N–N=C) and the ν(C–O), clearly indicating the iminolization in the process of coordinating the metals. These assignments are in agreement with the literature; all complexes appear to be of ML_2 stoichiometry (Patil *et al.*, 1982; Qingbao *et al.*, 1994; Yunyin *et al.*, 1998).

Table 6. Important mid-IR absorption frequencies (cm^{-1}) of **Feizone** and **Ferfurone** and their respective copper(II) and zinc(II) complexes in KBr disc, at room temperature.

Compound	ν(N–H)	ν(C=O)	ν(C=N)	ν(N–N)	ν(C=N–N=C)	ν(C–O)
Feizone	3147	1671	1604	896	–	–
Feizone-Zn	–	–	1568	918	1600	1260
Feizone-Cu	–	–	1514	915	1610	1240
Ferfurone	3207	1652	1608	930	–	–
Ferfurone-Cu	–	–	1581	1013	1615	1352

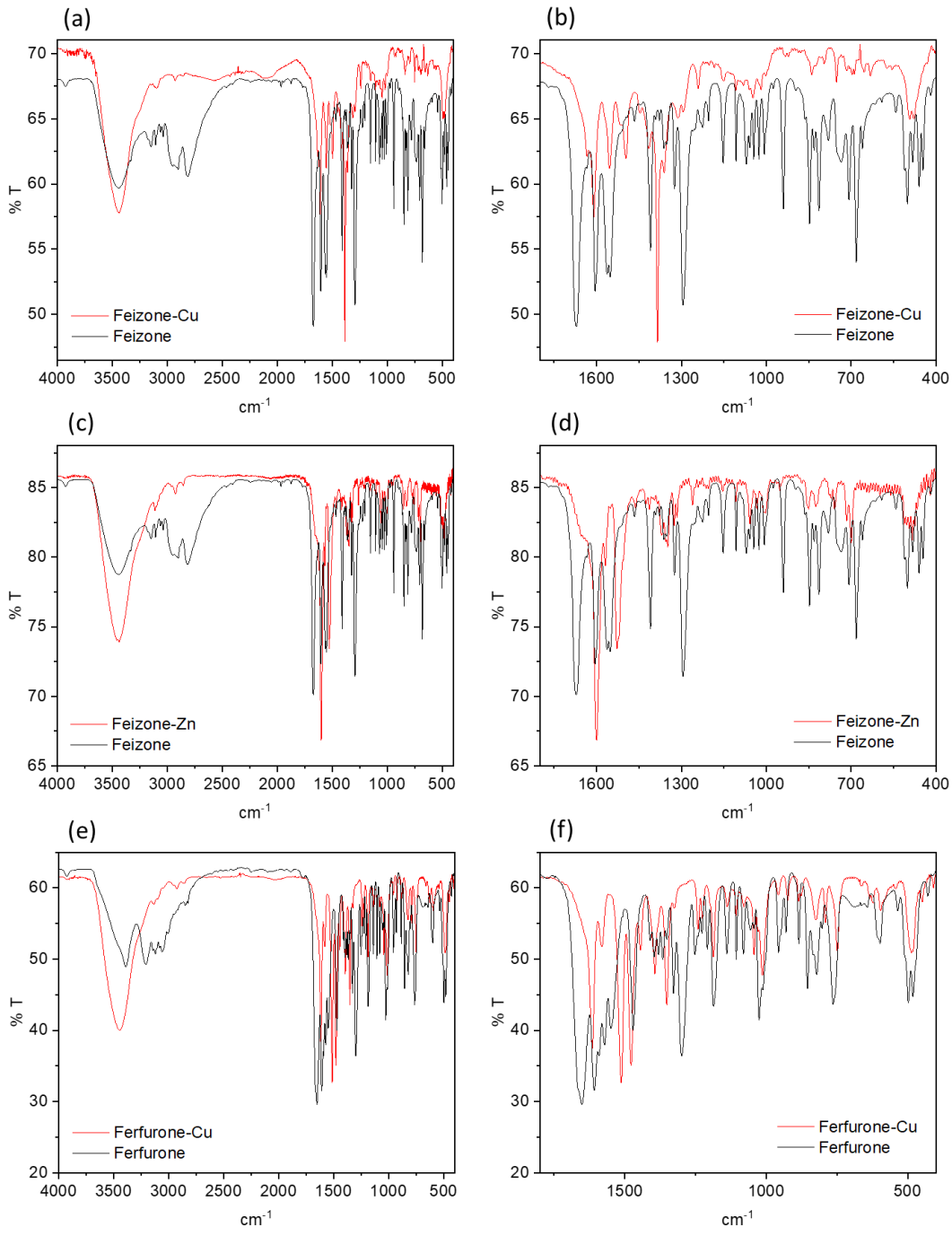

Figure 21. Mid-IR spectra in KBr pellets of **Feizone-Cu** (a), **Feizone-Zn** (c), and **Ferfurone-Cu** (e), along with a magnification in the 1750-400 cm^{-1} range for **Feizone-Cu** (b), **Feizone-Zn** (d), and **Ferfurone-Cu** (f).

5.3.2. Thermogravimetry Analysis

As the complexes were only poorly soluble in the conventional laboratory solvents, thermogravimetric analysis was performed in order to attempt to explore their structure, confirming the characteristics observed by the IR data. Again, this is useful mainly for studying the final inert residue at the end of the curve to check the metal composition of these compounds. The behavior of the compounds below 200 ºC is also important to attest the presence of coordinated or structural solvent molecules. The thermogravimetric curves are presented in Figure 22.

For **Feizone** complexes, decompositions starting at 300 ºC (**Feizone-Zn**) and 177 ºC (**Feizone-Cu**) were observed. In the latter, this may represent a coordinated solvent. The inert residues start at 597 ºC for Zn^{2+} and 522 ºC for Cu^{2+} complexes. Here, the final residue analysis becomes intricate, as there are two different metals present (either zinc and iron or copper and iron) and because, in the absence of crystallographic data, the total molar mass of these compounds is unknown. For this reason, more analyses are needed to explore these complexes' structures.

For **Ferfurone-Cu**, decompositions start at 268 ºC and end at 416 ºC, with a stable residue representing 33.6% of the total mass. This residue was assigned as a mixture of CuO and Fe_2O_3 (calculated: 33.8%), which confirms the 1:2 metal-to-ligand stoichiometry observed in the crystallographic analysis.

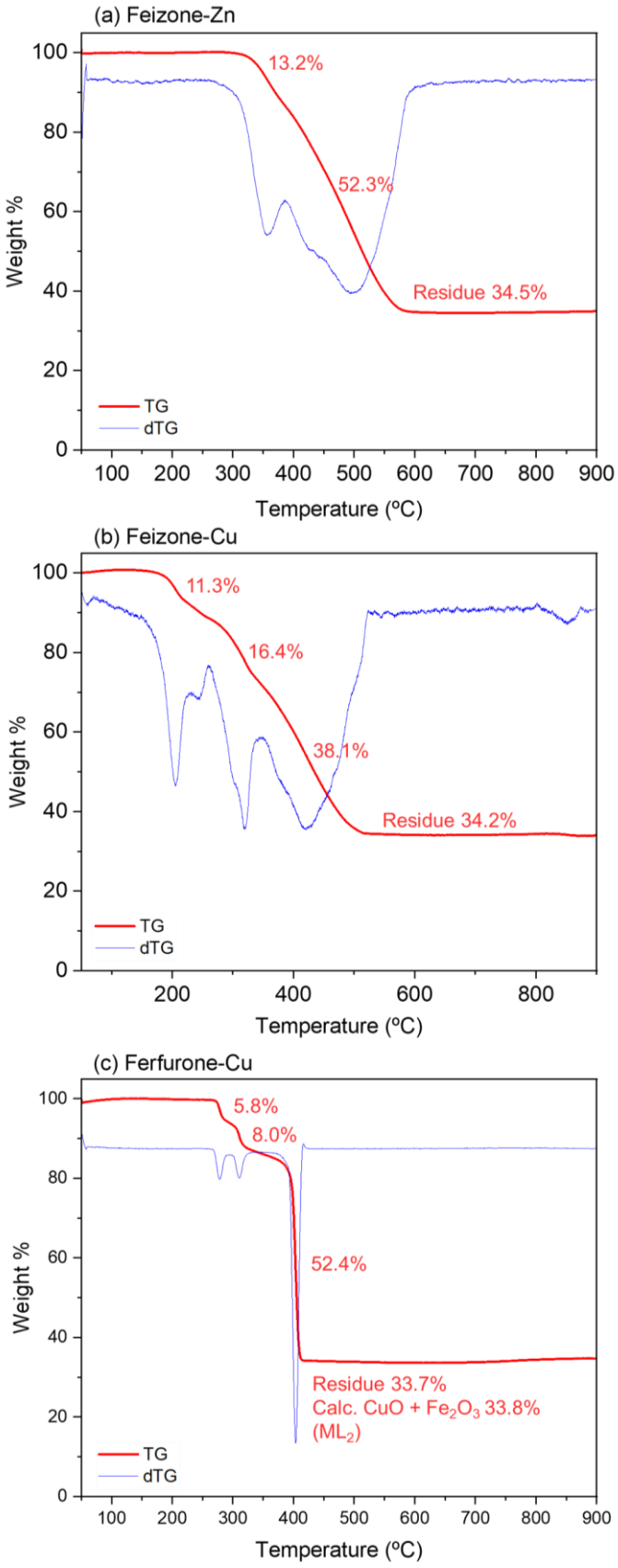

Figure 22. Thermogravimetric curves of **Feizone-Zn** (a), **Feizone-Cu** (b), and **Ferfurone-Cu** (c) complexes between 50-900 ºC, under N_2 flux (heat rate of 10 ºC min^{-1}) (red) and their first derivative (blue).

5.3.3. Emission Spectroscopy

The metal quantification through ICP-OES helps to elucidate the metal:ligand stoichiometry. Each one of the ligands **Feizone**, **Ferfurone,** and the complex **Ferfurone-Cu** have some kind of crystallographic data, being able just to confirm if the bulk crystals also have the same formula as the diffracted crystal. As discussed in the thermogravimetric analyses section, these compounds have experimental results outstandingly close to the theoretically calculated values. The ICP-OES data is no different, showing 0.1-0.5% difference between experimental and theoretical data. The calculations for **Ferfurone-Cu** were made based on CuO/Fe_2O_3 residue.

Meanwhile, the experimental data regarding **Feizone** complexes **Feizone-Zn** and **Feizone-Cu** greatly diverge from those calculated with basis on a 1:2 metal-to-ligand stoichiometry, for either Zn/Cu and Fe. The experimental and calculated percentages for every ligand and their respective complexes are displayed in Table 7.

Table 7. Mass percentage values (% m/m), experimental and calculated, of metals for every complex and their parent ligands. Experimental data obtained from ICP-OES assays and calculated values considers 1:2 metal-to-ligand stoichiometry complexes.

	%Fe		**%Zn**		**%Cu**	
	Exp.	Calcd.	Exp.	Calcd.	Exp.	Calcd.
Feizone	17.0	16.8	-	-	-	-
Ferfurone	17.8	17.3	-	-	-	-
Ferfurone-Cu	15.9	15.8	-	-	9.1	9.0
Feizone-Zn	20.0	15.3	18.0	9.0	-	-
Feizone-Cu	20.5	15.3	-	-	15.0	8.7

5.3.4. Cyclic Voltammetry Characterization

Due to the low solubility of the presented complexes, the voltammetric assays for these compounds were carried out using a more qualitative approach, only to investigate the behavior of the complexes when compared to the ligands. The cyclic voltammetry assays (Figure 23) were carried out at a 100 mV s^{-1} scan rate, using DMSO as the solvent and $TBAPF_6$ as the supporting electrolyte.

All three complexes showed an increased potential regarding the oxidation of the ferrocenyl group in comparison with their respective ligands, meaning that the metal coordination by the hydrazone group makes the ferrocenyl group less prone to oxidation. The anodic potential peak for **Feizone** is +0.678 V *vs.* Ag/AgCl, while for **Feizone-Zn** and **Feizone-Cu** are 0.800 and 0.775 V *vs.* Ag/AgCl, respectively.

In **Feizone-Zn** voltammogram, there are oxidation and reduction waves in the same potentials as those of the free ligand, suggesting that part of the complex dissociates after solubilization. This behavior is probably due to zinc(II) complex's low stability in polar solvents as DMSO.

For **Ferfurone**, the anodic peak is found at +0.665 V *vs.* Ag/AgCl, and for **Ferfurone-Cu**, at +0.777 V *vs.* Ag/AgCl. The increased potential indicates an electron withdrawal effect upon the ferrocenyl group, making it less possible for the Fe^{2+} ion present in the structure to give away another electron in an oxidation reaction. As in the previous cases, the reduction wave is absent in the potential range scanned for these complexes, in DMSO, suggesting strongly irreversible processes for the ferrocenyl group. These observations indicate that the coordination deeply affects the electronic properties of the ligands considered here, and the observed irreversibility points to slower diffusion kinetics on the working electrode. We can then conclude that complexation to copper(II) or zinc(II) makes the ferrocenyl-associated process irreversible, by suppressing the reduction wave.

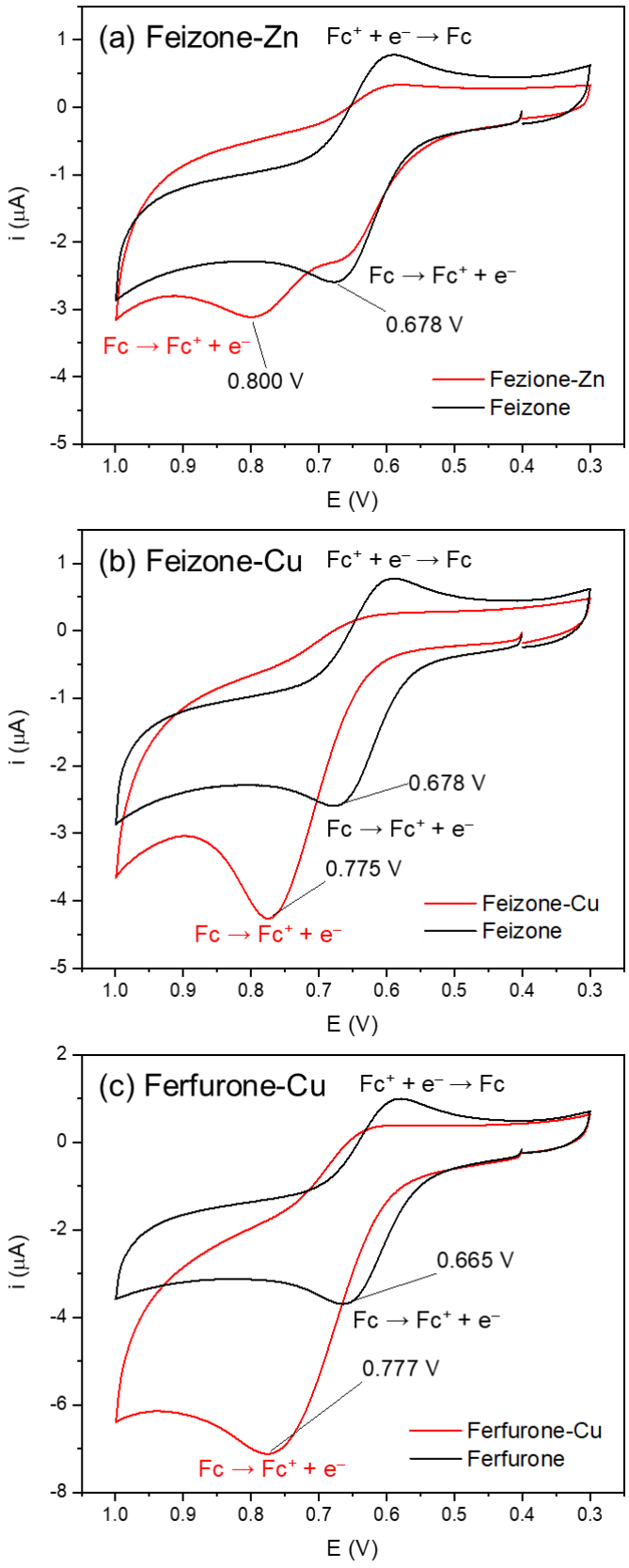

Figure 23. Cyclic voltammograms of the complexes **Feizone-Zn** (a), **Feizone-Cu** (b), and **Ferfurone-Cu** (c) superimposed with their respective parent ligands. Measurements were performed in DMSO containing 0.1 mol L^{-1} $TBAPF_6$, at the scan rate of 0.100 V s^{-1}. Potentials *vs.* Ag/AgCl 3 mol L^{-1} KCl electrode.

6. Results and Discussion Part II – Deprotonation, Stability, and Complexation Studies

6.1 Apparent pK_a through Cyclic Voltammetry

The apparent pK_a for **Feizone** and **Ferfurone** were estimated through cyclic voltammetry assays. Since the zinc complexes were only obtained with the addition of a strong base, it becomes important to estimate the pH where the hydrazone amide deprotonation occurs. Thus, this assay consisted of reading several voltammograms on equally distant pHs, as presented in Figure 24. It is clear that, between pH 10 and 11, both voltammograms begin to change drastically, pointing to changes in the electronic structure of the hydrazone as a function of the pH. This evidence suggests that a possible iminolization due to the hydrazone's amide deprotonation induces changes in the electrochemistry, not only of the ferrocenyl group, but in other parts of the molecules as well, as seen by the appearance of another redox couple at about +0.62 V *vs.* Ag/AgCl for both ligands. By plotting $E_{½}$ (the average between the two, cathodic and anodic, potential peaks) against the pH, it is possible to estimate the apparent pK_a for this reaction at the curve's inflection point (Compton & Banks, 2007). This process results in the pK_a values of 10.71 ± 0.04 for **Feizone** and 11.01 ± 0.03 for **Ferfurone**. The lesser pK_a for **Feizone** could be due to the aromatic structure of the pyridine group adjacent to the acidic hydrogen on the hydrazone, being easier to deprotonate due to higher electronic delocalization. Both ligands stay mainly in the protonated form at physiological pH (7.4), meaning they probably couldn't coordinate zinc(II) ions in this condition, as previously stated.

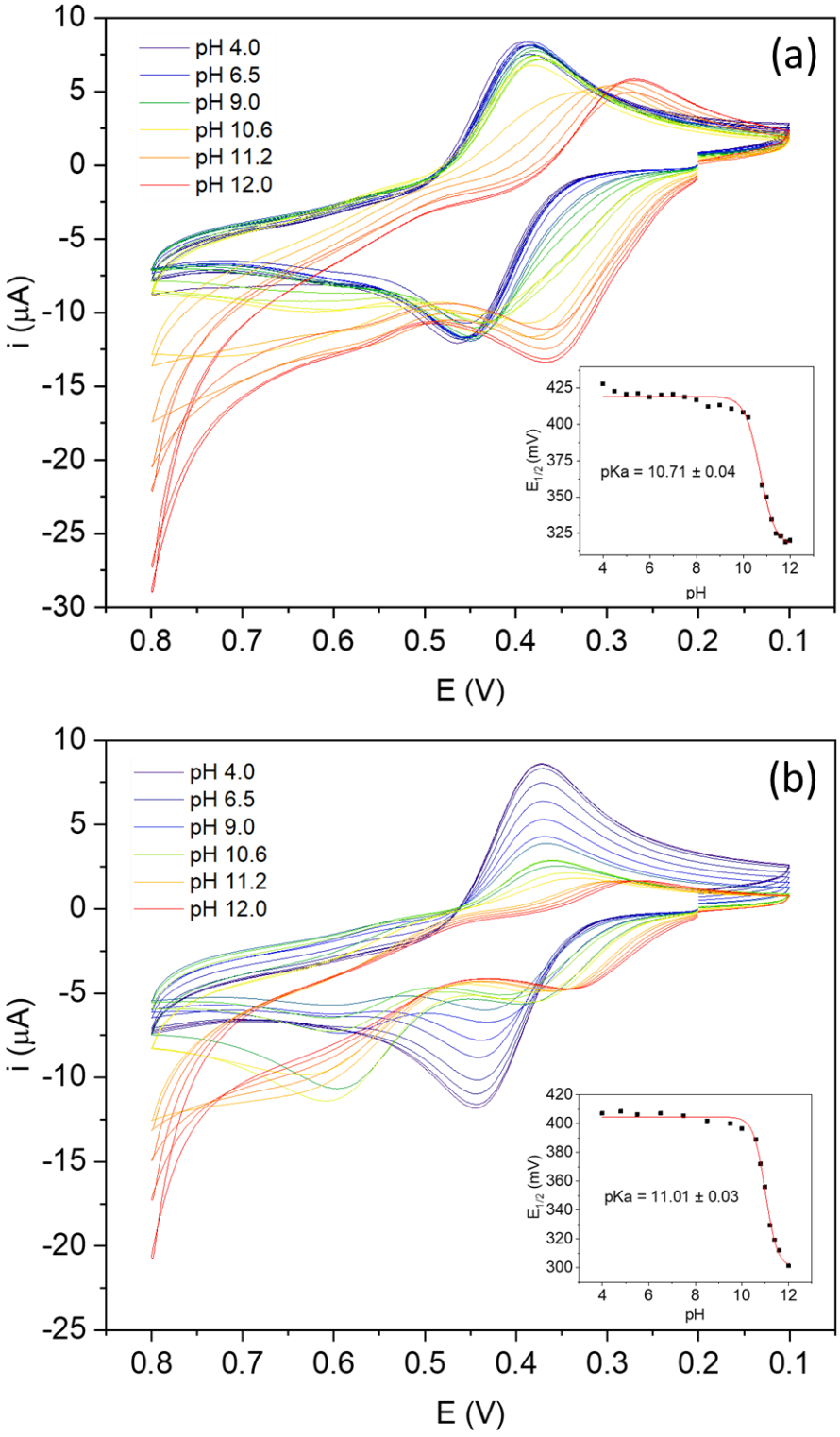

Figure 24. Cyclic voltammogram of **Feizone** (a) and **Ferufurone** (b) in methanol/water 1:1 mixture with NaCl 0.1 mol L^{-1} in different pH values at 100 mV s^{-1}. The inset shows the $E_{½}$ *vs.* pH plot and the pK_a value obtained by a Boltzmann fitting. Only some of the pH values is shown in the legend for simplification Potentials *vs.* Ag/AgCl 3 mol L^{-1} KCl electrode.

6.2. Hydrolytic Stability

Since the aim of the study for these compounds is centered on their potential biological activity, and knowing that *N*-acylhydrazones can undergo hydrolysis, it is fundamental to investigate their stability in aqueous solution at *pseudo*-biological conditions (pH 7,4). Therefore, the hydrolytic stability of both ligands was studied at regular intervals for 48 h through UV-Vis spectroscopy, as shown in Figure 25. Comparing the absorption bands of ligands and their precursors over time allow us to confirm the hydrolysis reaction. Taking the wavelength of maximum absorption as reference (301.5 nm for **Feizone** and 308.0 nm for **Ferfurone**), the concentration retainment after 12 h is 90% and 93% for **Feizone** and **Ferfurone**, respectively. This stability is associated with a great electron delocalization within the structure of these ligands, which is in accordance with other hydrazones previously studied by our group with similar electron conjugation (Cukierman *et al.*, 2018; Cukierman *et al.*, 2020). Since the average estimated time for a drug to act in the body is 8 h, these ligands appear reasonably stable in aqueous solution as drug candidates.

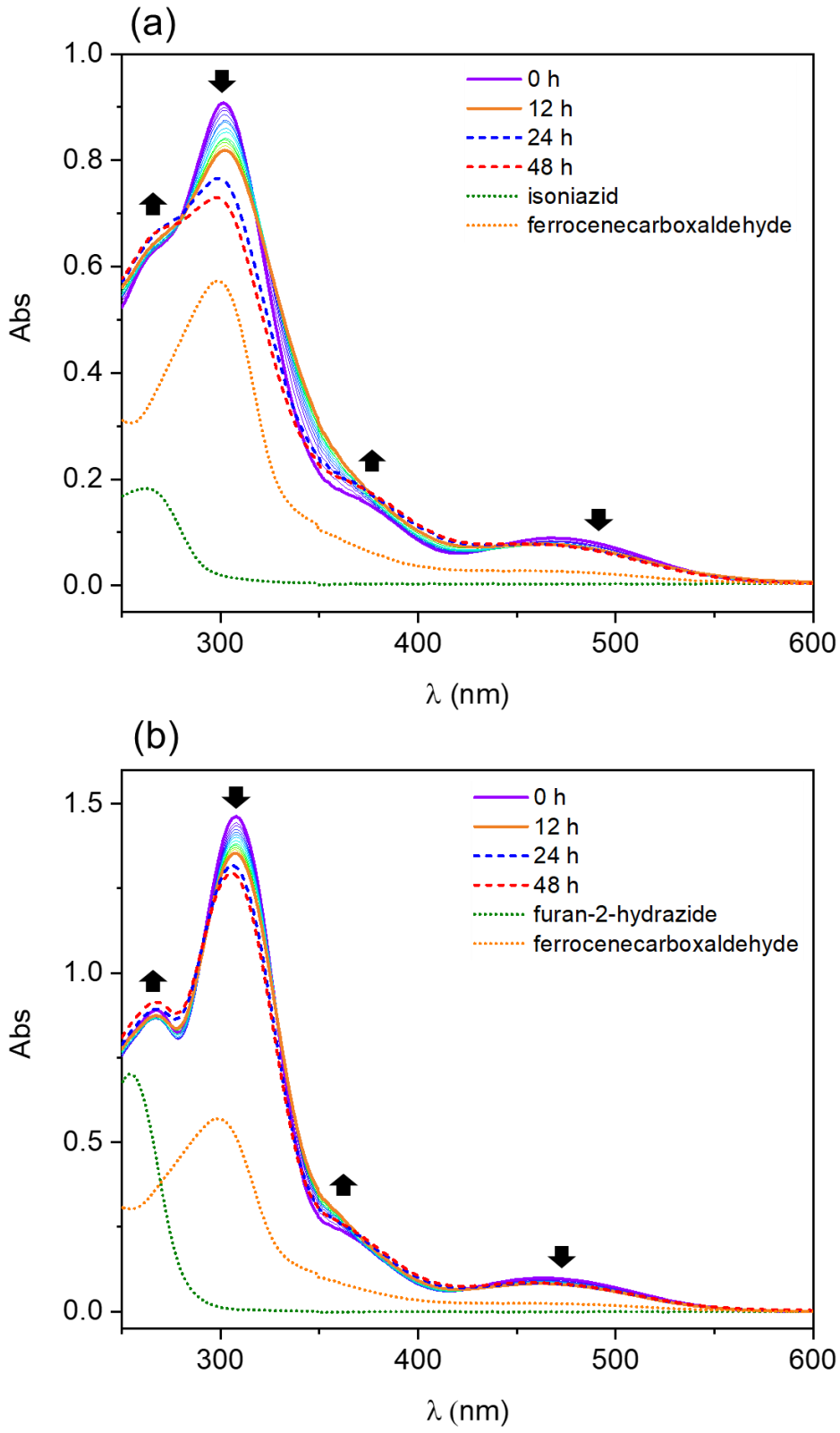

Figure 25. Electronic molecular absorption spectra of **Feizone** (a) and **Ferfurone** (b) at 50 μmol L^{-1} in 1% DMSO/TRIS 10mmol L^{-1} (pH 7.4) taken at regular intervals for 48 h. The spectra of the precursors, isoniazid and furan-2-hydrazide, are shown in dotted green lines, and ferrocenecarboxaldehyde in orange. Black arrows indicate the temporal changes in the spectra.

6.3 Photolytic Stability Study

The hydrolytic stability assays discussed above were carried out by protecting the compounds from external light sources; otherwise, a distinguishable darkening occurs in the solutions' colors. This behavior was observed for both ligands and the ferrocenecarboxaldehyde precursor, varying according to the solvent (Figure 26). Although **Feizone** and **Ferfurone** have been reported in the literature (Gupta *et al.*, 2014; Krishnamoorthy *et al.*, 2012; Patil *et al.*, 1982; Qingbao *et al.*, 1994; Ravindran *et al.*, 2023; Sathyadevi *et al.*, 2012; Yunyin *et al.*, 1998), it is important to remark that we could not find any previous mention to this behavior, possibly because it passed unseen in the described published research or it was decided to "hide" this "inconvenient property" due to its inherent complexity. When exposed to light, the solutions are unstable in DMF and DMSO, but have some stability in methanol and ethanol, even with sunlight exposure (Figure 27).

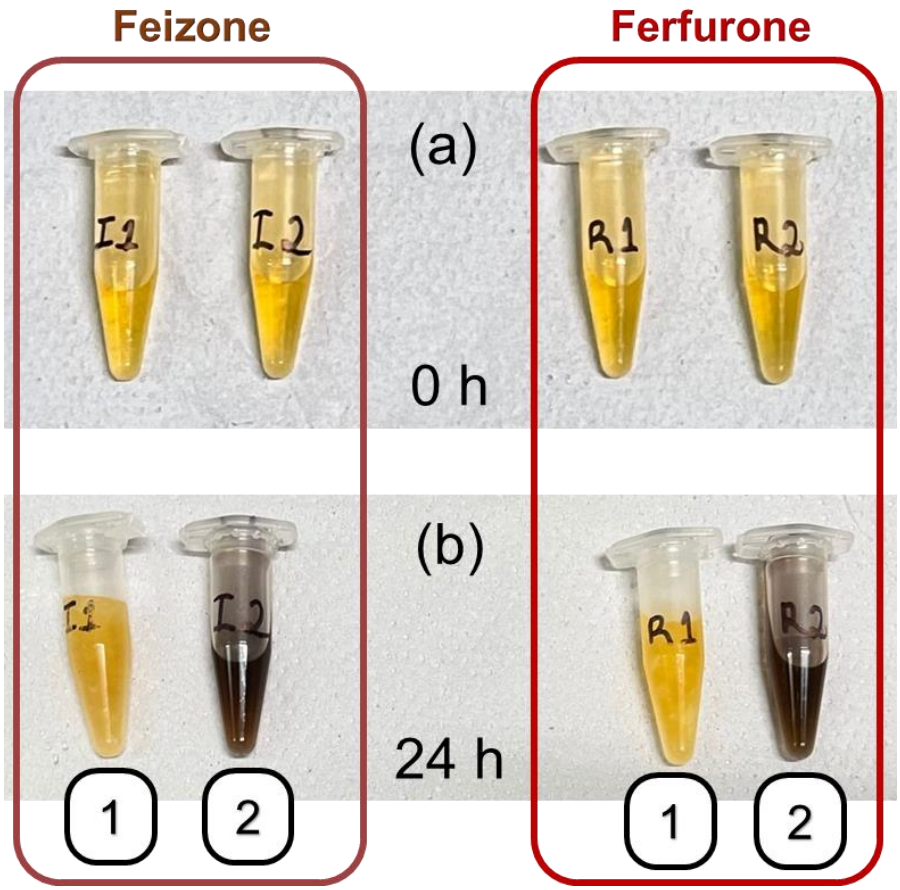

Figure 26. Photos at different timepoints of DMSO solutions (1.0 mmol L^{-1}) of **Feizone** (left) and **Ferfurone** (right) immediately after preparation (a) and after 24 h of storage (b). Solutions labeled as 1 were kept at 4 ºC protected from sunlight, while solutions labeled as 2 were exposed to sunlight.

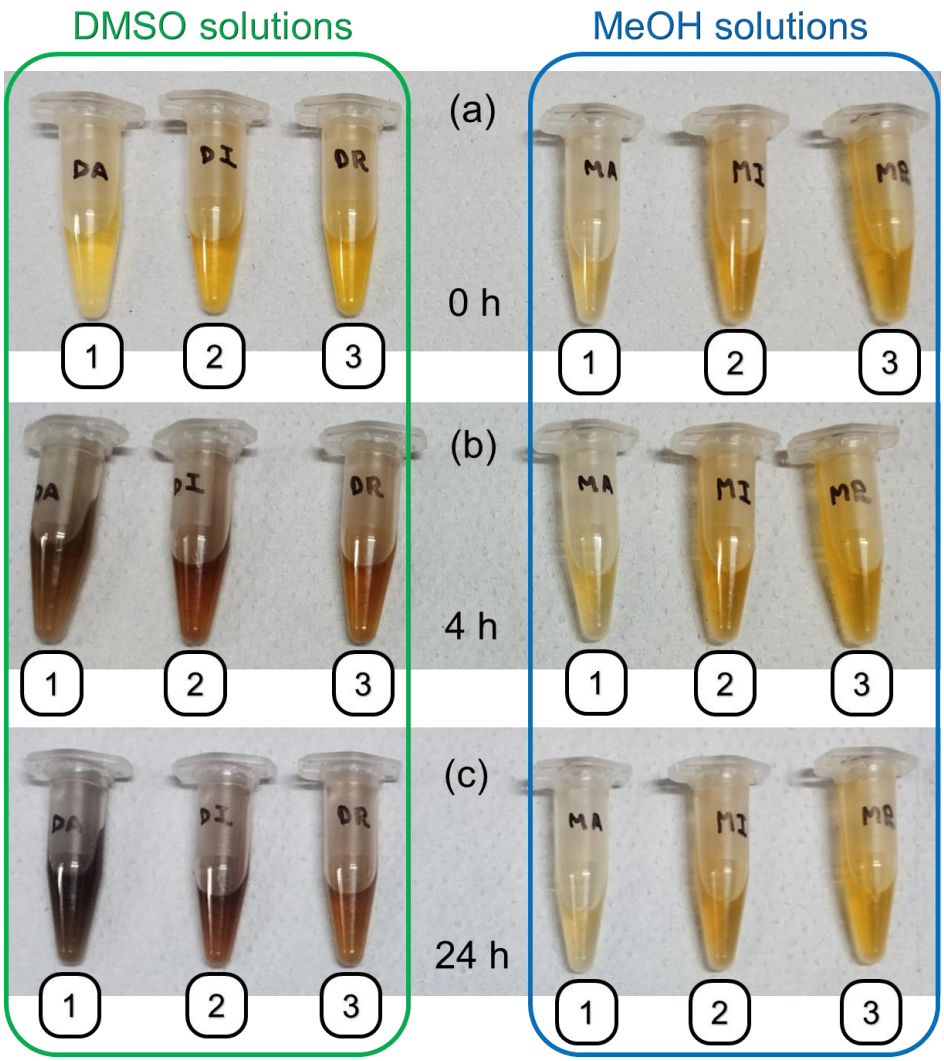

Figure 27. Photos at different timepoints of solutions (1.0 mmol L^{-1}) in DMSO (left) and methanol (right) of ferrocenecarboxaldehyde (1), **Feizone** (2), and **Ferfurone** (3). Photos were taken immediately after preparation (a), after 4 h (b), and after 24 h of bench storage (c) under direct sunlight exposure.

In the solid phase, some dark precipitates were also found among the ligands' crystals obtained from the reaction, but could not be isolated or characterized. After being stored at room temperature and protected from light sources, the ligands and their complexes maintained their color and structure for months in the solid state. ^{1}H NMR spectra of the darkened solutions were taken on DMSO-d_6, after 24 h of sunlight exposure. The spectra showed broadened and poorly resolved signals for ferrocenecarboxaldehyde and slightly broadened signals for both ligands, as shown in Figure 28, which may indicate oxidation of iron in the ferrocenyl group to the

paramagnetic form Fe^{3+}. For **Feizone**, after 24 h, a couple of signals at 7.81 and 8.77 ppm disappear, and a broad singlet appears around 8.10 ppm; for **Ferfurone**, after 24 h, every signal is maintained and slightly broadened. Surprisingly, two tiny signals appear in the 24 h spectra at 6.57 and 6.48 ppm. As the **Ferfurone** spectrum has more resolution, it is possible to identify these signals as two doublets with a roof effect. As they appear with the same chemical shift for the three compounds, the signals could have probably come from a solvent-related process.

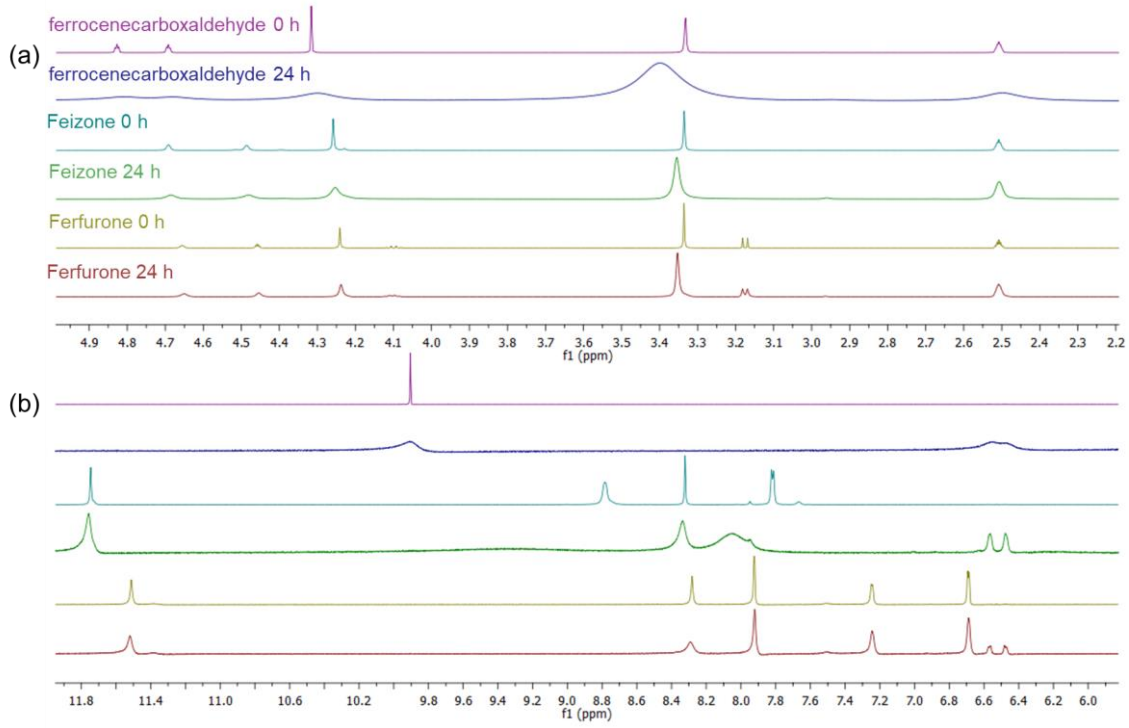

Figure 28. ^{1}H NMR spectra of ferrocenecarboxaldehyde, **Feizone,** and **Ferfurone** in DMSO-d_6 at 0 h (violet, cyan, and yellow, respectively), and after 24 h under sunlight exposure (blue, green, and red, respectively). Spectra are cut from 2.2 to 5.0 ppm (a) and from 6.0 to 12.0 ppm (b) for better observation of signal broadening.

UV-Vis spectroscopy data were taken in equally spaced time lapses for 4 h on samples protected from and exposed to light (Figure 29). Comparing those spectra, a hyperchromic effect over time for compounds exposed to sunlight is noticeable. There is also a slight hypsochromic shift of approximately 6.5 nm in the *d-d* band of the unsheltered solutions. The lack of important wavelength shifts suggests the structure around the coordination site on ferrocenyl is maintained. The spectrum of ferrocenecarboxaldehyde is the one most drastically changed over time, even in the

absence of light, showing different processes that appear to be aggravated by light exposure. Even though, the alterations in the *d-d* bands are similar to those observed in **Feizone**'s and **Ferfurone**'s spectra, suggesting it undergoes the same chemical process as the ligands. This indicates that the chemical change is probably centered on the ferrocenyl moiety of these compounds. Additionally, the fact that the changes observed seem to be more drastic for ferrocenecarboxaldehyde points out that the presence of the *N*-acylhydrazone group somehow attenuates this process.

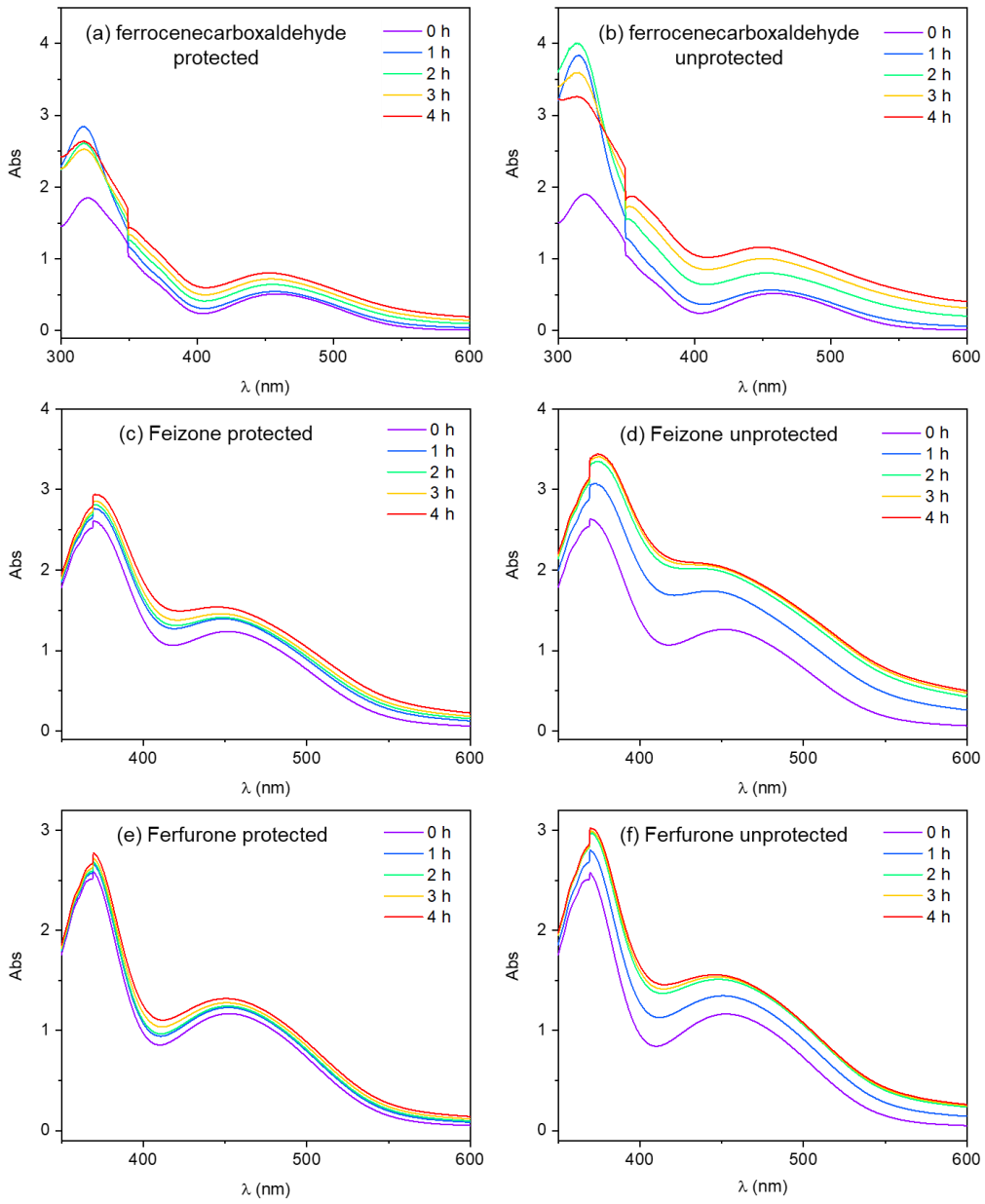

Figure 29. Molecular electronic absorption of ferrocenecarboxaldehyde (a, b), **Feizone** (c, d), and **Ferfurone** (e, f) at 1.0 mmol L^{-1} in DMSO both protected (left) and unprotected (right) from sunlight in equally spaced timepoints for 4 h.

On this evidence, we propose a process involving the oxidation of Fe^{2+} to Fe^{3+} by the loss of one electron to the solvent, possibly explaining the UV-Vis assay's lack of wavelength absorption shift. This process may also account for the increased instability in DMF and DMSO rather than in methanol / ethanol since these solvents are more prone to receive an electron. Moreover, as mentioned above, it suggests that the broader and unresolved ^1H NMR signals are due to the presence of the oxidized Fe^{3+} center, which is paramagnetic and reduces the magnetic relaxation time, broadening the signals (Hore, 2015). Moreover, if the solvent reacts with the ferrocenyl-containing compound in this manner, it corroborates the hypothesis that the two doublets at 6.57 and 6.48 ppm in the ^1H NMR spectra originated from the DMSO-derived reaction product. However, an entire understanding of this process requires additional studies, which go beyond the scope of this work.

Nevertheless, if the reaction is indeed an oxidation of the ferrocenyl group involving the solvent, it would be expected that the compounds will progressively be converted from neutral to positively charged species in solution, increasing their conductivity. Table 8 shows the results of conductivity measurements performed on freshly prepared, 4 h aged and 24 h aged solutions of ferrocenecarboxaldehyde (precursor), **Feizone** and **Ferfurone**. On the other hand, cyclic voltammograms of the freshly prepared and 24 h aged solutions are shown in Figure 30.

Table 8. Molar conductivity (S cm² mol^{-1}) over time of DMSO and MeOH 1.0 mmol L^{-1} ferrocenecarboxaldehyde, **Feizone** and **Ferfurone** solutions exposed to sunlight (25 ºC).

Compounds	**Molar Conductivity in DMSO (S cm² mol^{-1})**				**Molar Conductivity in MeOH (S cm² mol^{-1})**			
	0 h	4 h	24 h	$\%_{24h}$*	0 h	4 h	24 h	$\%_{24h}$*
Precursor	2.63	4.40	6.57	**+149%**	81.6	81.4	81.1	–
Feizone	1.54	2.85	3.63	**+136%**	3.50	3.95	4.38	**+25%**
Ferfurone	2.12	4.13	5.66	**+168%**	3.48	3.80	4.15	**+19%**

* $\%_{24h}$ stands for percentage change after 24 h.

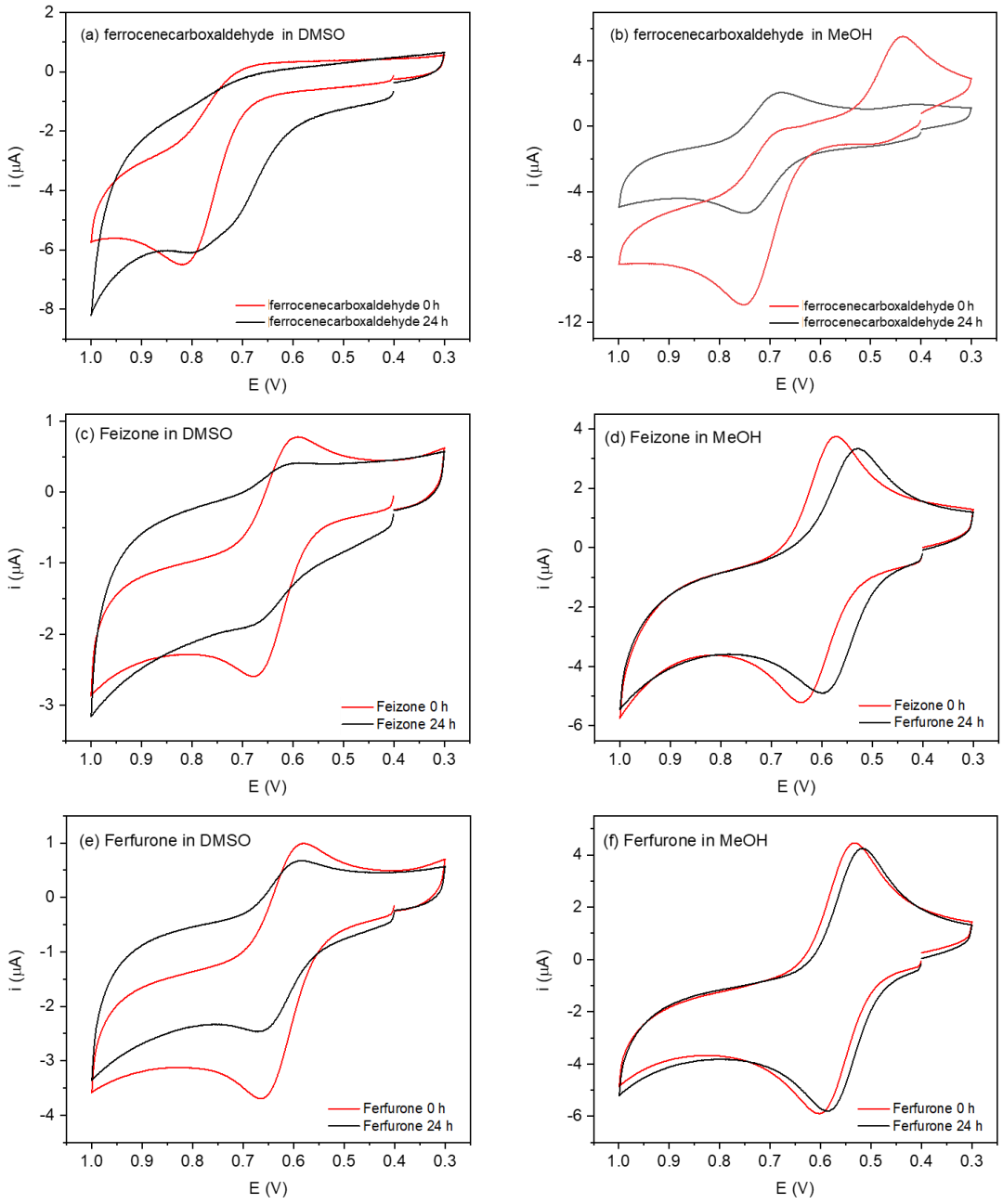

Figure 30. Cyclic voltammograms of ferrocenecarboxaldehyde (a, b), **Feizone** (c, d) and **Ferfurone** (d, f) in DMSO (left) and MeOH (right), at a concentration of 50 µmol L^{-1}, at 100 mV s^{-1} scan rate. Supporting electrolyte is 0.1 mol L^{-1} $TBAPF_6$. The voltammograms refer to freshly prepared (red) and 24 h aged – sunlight exposed (black) solutions. Potentials *vs.* Ag/AgCl 3 mol L^{-1} KCl electrode.

The conductivity measurements show increasing values over time for these compounds, presenting a 136% to 168% intensification for DMSO solutions and a 0 to 25% variation in MeOH, after 24 h. However, the literature points out that the conductivity value for a 1:1 electrolyte (1.0 mmol L^{-1}) is much higher, in the range of 50-70 S cm^2 mol^{-1} in DMSO and 80-115 S cm^2 mol^{-1} in MeOH (Geary, 1971). This suggests that the oxidation of the ferrocenyl derivatives is not complete, but rather occurs only to a limited extent.

In DMSO solution, ferrocenecarboxaldehyde shows an irreversible process, with a well-defined anodic potential at +0.821 V *vs.* Ag/AgCl. After 24 h of sunlight exposure, the voltammogram appears enlarged, the cathodic peak potential (E_{pc}) is still absent and the anodic peak potential (E_{pa}) appears slightly shifted to +0.803 V.

On the other hand, **Feizone** in DMSO solution presents both the anodic and cathodic waves, with peaks at +0.678 and +0.590 V *vs.* Ag/AgCl, respectively. After 24 h of sunlight exposure, peak current reduces but potentials are virtually the same. In the case of **Ferfurone,** a similar behavior is observed.

In this sense, we can conclude that, besides the reported current differences, the voltammograms of the freshly prepared and sunlight-aged (24 h) solutions for both **Feizone** and **Ferfurone** are very similar. This is, once again, consistent with an ageing process mainly mediated by ferrocenyl oxidation, since we expect that the voltammograms of reduced and oxidated counterparts in a redox couple to be identical. As stated before, the Nicholson-Schain equation (Equation 12) represents the relation between the peak current and various parameters.

$$i_p = 0.4463\, A\, (n\, F)^{3/2} \left(\frac{D c_0 v}{RT}\right)^{1/2} \qquad 12$$

The only two possible parameters that could affect current are the diffusion coefficient (D) and the bulk concentration (c_0). As the potential shifts very slightly after 24 h, the main responsible for the loss in current values might be the change in the diffusion coefficient, which depends on solvent viscosity (μ) and the solute Stokes radius (R_0), as stated in the Stokes-Einstein equation (Equation 13).

$$D = \frac{k_B T}{6\pi\mu R_0} \quad (13)$$

As the solution viscosity should not vary much with the whole process, the origin of the voltammogram's current change appears to be on the Stokes radius. As such, a possible increase of charge in the solution by oxidating the ferrocenyl group could induce a violent change in the Stokes radii of these compounds.

In contrast, the MeOH cyclic voltammograms for the ligands show very little change in current magnitude for these compounds, corroborating the observations made so far, as no visible darkening is observed even after 24 h.

However, the ferrocenecaerboxaldehyde precursor, which shows a process of low reversibility with E_{pa} and E_{pc} of +0.753 and +0.435 V *vs.* Ag/AgCl, respectively, changes it into an apparently reversible one with $E_{½}$ equal to +0.714 V *vs.* Ag/AgCl after 24 h of light exposure. The different behavior of ferrocenecaerboxaldehyde and the ligands elucidates that these compounds undergo distinct processes upon light exposure, even though they present the same macroscopic aspect in solution.

Following through, **Feizone** in MeOH appears with E_{pa} and E_{pc} shifted after 24 h of sunlight exposure from +0.640 V and +0.571 V to +0.597 V and +0.530 V *vs.* Ag/AgCl, respectively. Meanwhile, **Ferfurone** has its E_{pa} and E_{pc} values shifted from +0.608 V and +0.532 V to +0.587 V and +0.517 V, correspondingly.

6.4 Cyclic Voltammetry Complexation Studies

Cyclic voltammetry was used to study the complexation of two biometal-derived ions, Zn^{2+} and Cu^{2+}, which are fundamental in the context of Alzheimer's disease (Bush, 2003). Assays on the coordination of zinc by **Feizone** and **Ferfurone** were carried out first. As Zn^{2+} does not undergoes any electrochemical process in the studied potential range, it is expected to be electrochemically silent in these assays, which aimed to understand the voltametric profile of the ferrocenyl group in the course of a metal ion coordination.

6.4.1. Zinc Complexation Study

Firstly, to attest to the need for a strongly basic medium to deprotonate the hydrazone for this reaction to occur, the voltammograms shown in Figure 31 depict the addition of Zn^{2+} to a ligand solution with no addition of base. After adding the zinc solution until reach three times the molar equivalent of the ligand, a strong base was added. The voltammogram stays practically unchanged for both ligands during the zinc addition, with potential peaks E_{pa} and E_{pc} of +0.461 and +0.390 V for **Feizone** and +0.448 and +0.382 V for **Ferfurone**, respectively. The potential peaks are shifted when the base is added, indicating the complexation reaction only occurs in a strongly basic medium, as previously stated. After the base addition, the potential peaks shift to +0.485 V (E_{pa}) and +0.400 V (E_{pc}) for the ligand **Feizone** and +0.469 V (E_{pa}) and E_{pc} +0.396 V (E_{pc}) for **Ferfurone**. The current of both peaks also changes notably after the addition of NaOH, turning the voltammogram much narrower, probably due to the low solubility of the formed complexes. The **Feizone** ligand presents anodic (i_{pa}) and cathodic (i_{pc}) peak currents of −11.1 and +7.79 μA, before the base was added, and −3.54 and +2.64 μA after its addition, respectively. **Ferfurone** presents i_{pa} of −11.2 and i_{pc} of +7.92 μA, which change to −9.72 and +6.07 μA after addition of the base. As can be seen, this phenomenon is intensified in the case of **Feizone**, since **Feizone-Zn** is only sparingly soluble in most organic solvents. It is important to point out that when the base is added before the zinc is already in the solution a different behavior is observed, pointing out that the order of reactants addition influences the final product, as discussed in the next paragraph.

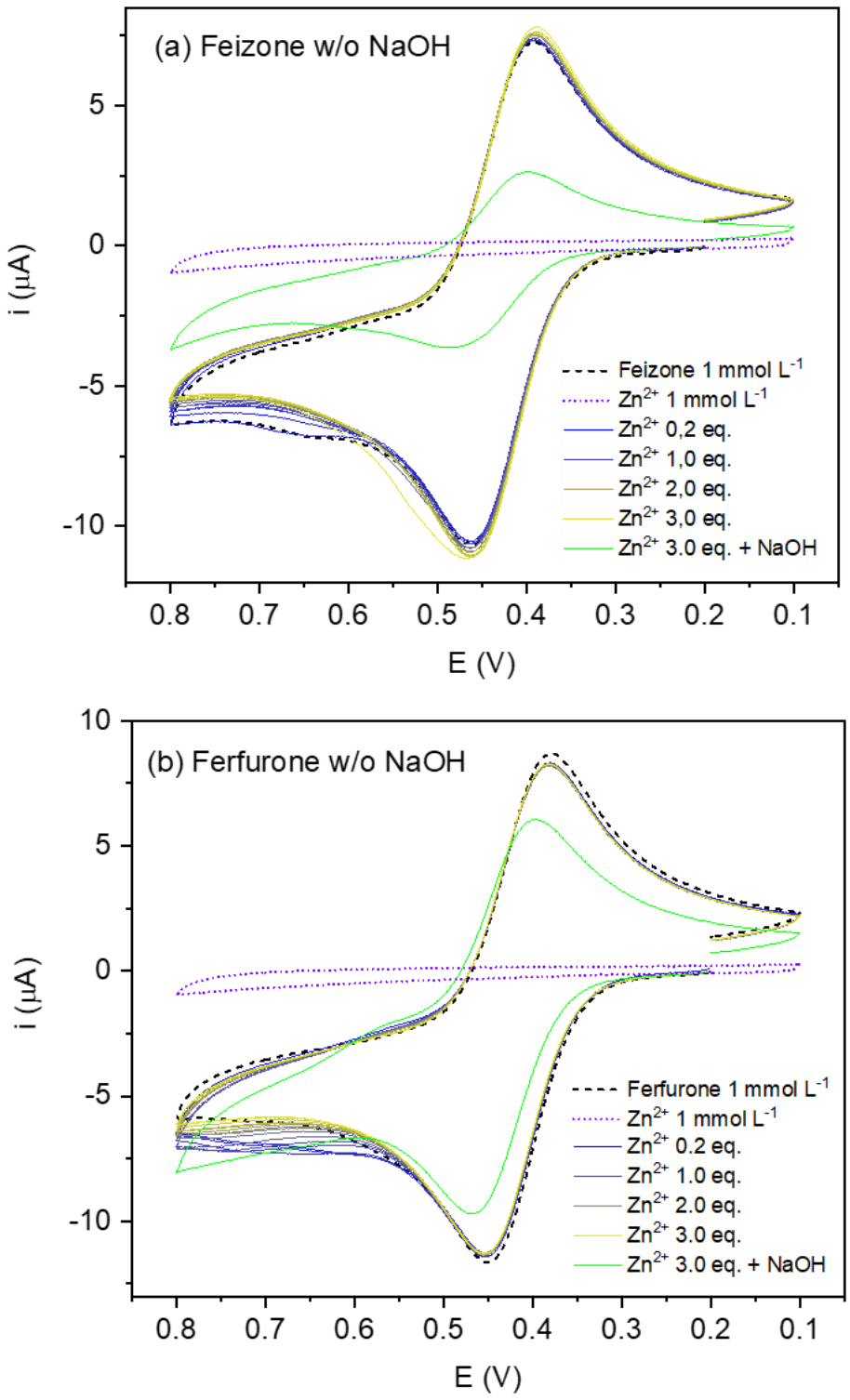

Figure 31. Cyclic voltammograms of 1.0 mmol L^{-1} of **Feizone** (a) and **Ferfurone** (b) with 0.1 mol L^{-1} NaCl in a methanol/water 1:1 mixture, initially with no addition of NaOH (black dashed line), then progressively adding Zn^{2+} solution until 3 molar equivalents in relation to the ligand (blue to yellow lines). After the zinc had been added, 1 molar equivalent of NaOH was added (green line), triggering the reaction. The voltammogram of a 1 mmol L^{-1} Zn^{2+} solution under the same conditions (blue dotted line) was included for comparison. Potentials *vs.* Ag/AgCl 3 mol L^{-1} KCl electrode.

Next, still regarding the study of zinc(II) complexation, the base was added before any addition of zinc, as presented in Figure 32. Basification of the medium affects significantly the voltammogram profile, as already reported during the pK_a estimation experiment. Instead of the only *quasi*-reversible electrochemical process typical of these ligands, in a strongly basic medium, two different electrochemical processes appear, with average of potential peaks ($E_{½}$) of +0.618 and +0.427 V *vs.* Ag/AgCl for **Feizone**; and +0.557 and +0.376 V for **Ferfurone**.

For **Feizone**, the magnitude of the current decreases for both the oxidation and reduction processes of the ferrocenyl group as the titration with zinc progresses, which is accompanied by a slight displacement of peak potentials. However, the most significant change in the voltammogram occurs at the first addition of zinc (0.2 molar equivalents): the one-process behavior is regained, suggesting that the irreversible second process seen in basic medium originates from the free iminolate group formed upon deprotonation of the hydrazone (Figure 32a).

By plotting i_{pc} as a function of the molar equivalents of Zn^{2+} (Figure 32a, *inset*) it is possible to observe a double sigmoidal curve profile, suggesting that the complexation reaction occurs in two sequential steps of different stoichiometries. Inflection points are found at 0.28 ± 0.05 and 1.52 ± 0.04 of Zn^{2+} molar equivalents. Although the second inflection point seems to point out to a 3:2 metal-to-ligand stoichiometry, additional research is necessary to better understand the chemical nature of the product(s) formed. The very low solubility of **Feizone-Zn** precludes carrying out more in-depth solution studies on it.

For **Ferfurone**, the progressive addition of zinc(II) ions recovers completely the ligand's voltammogram profile in a neutral medium, suggesting that, instead of being coordinated by **Ferfurone**, the metal is somehow promoting the protonation of the hydrazone group. As zinc(II) is an amphoteric cation, the observed behavior can be due to its reaction with the base, forming soluble zinc hydroxide complexes, which might be preferable over the **Ferfurone-Zn** complex. This process releases protons back to the medium, possibly promoting the ligand's protonation. The fact that this phenomenon doesn't occur for the **Feizone-Zn** system rises the hypothesis of polymerization in the case of this complex, which leads to more stable products being preferable over zinc(II) hydroxide complexes. This does not seem to happen for **Ferfurone**, possibly because the furan group has a lower coordinating power.

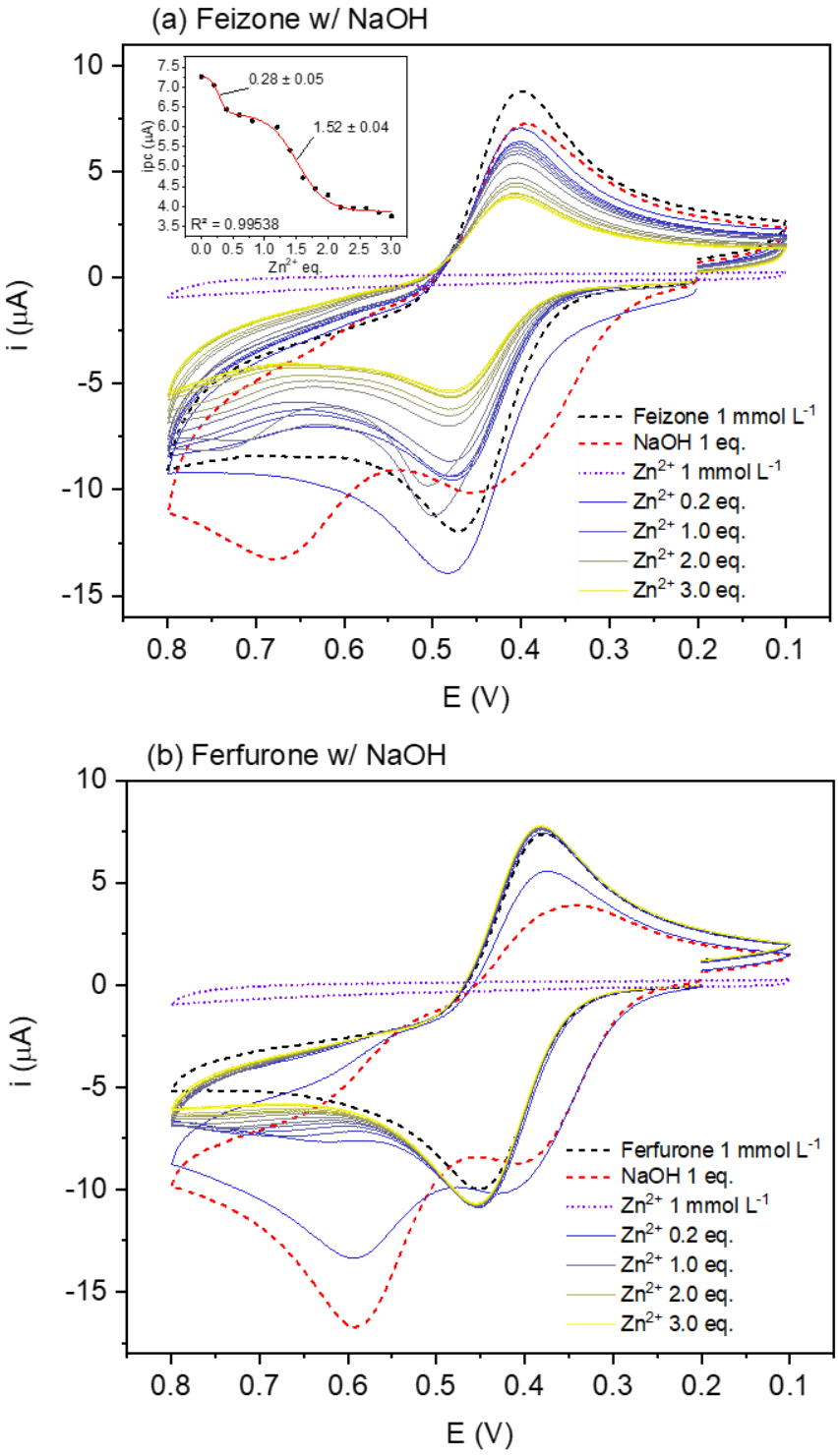

Figure 32. Cyclic voltammograms of 1.0 mmol L^{-1} of **Feizone** (a) and **Ferfurone** (b) with 0.1 mol L^{-1} NaCl in a methanol/water 1:1 mixture (black dashed line) and with the addition of 1 molar equivalent of NaOH (red dashed line). Then, Zn^{2+} solution was progressively added until 3 molar equivalents in relation to the ligand (blue to yellow lines). The voltammogram of a 1 mmol L^{-1} Zn^{2+} solution under the same conditions (blue dotted line) was included for comparison. *Inset* [**32a**]: i_{pc} *vs.* Zn^{2+} molar equivalents addition for the ligand **Feizone**. Fitting was performed with a BiDoseResp function. Potentials *vs.* Ag/AgCl 3 mol L^{-1} KCl electrode.

6.4.2. Copper Complexation Study

For copper(II) complexation, there is no need for any base addition, as previously stated. As such, the copper(II) solution was progressively added, and the voltammograms are shown in Figure 33. Two distinct electrochemical processes happen for these voltammograms, the ferrocenyl redox couple with $E_{½}$ for **Feizone** and **Ferfurone** at +0.417 and +0.411 V, and the copper redox couple, at +0.256 and +0.256 V, respectively after 2 molar equivalents of Cu^{2+} addition. Both ligands show slight potential shifts in the ferrocenyl process. The most apparent change in both voltammograms is the magnitude increase of current regarding the Cu^{2+} transformation, which also presents potential shifts in the oxidation and reduction processes. For **Feizone**, after the 2-molar equivalent addition of Cu^{2+} solution, the ferrocenyl process potential slightly shifts from +0.452 V E_{pa} and +0.380 V E_{pc} to +0.453 V and +0.381 V E_{pa} and E_{pc}, respectively. For **Ferfurone**, E_{pa} and E_{pc} shift from +0.455 V and +0.379 V to +0.451 V and +0.371 V respectively. The most significant change in both voltammograms is the copper reaction, which initially appears as free Cu^{2+} with E_{pa} and E_{pc} of +0.315 V and +0.206 V, being shifted to +0.319 V and +0.192 V for **Feizone-Cu** and +0.311 V and +0.201 V for **Ferfurone-Cu** after 2-molar equivalent addition of Cu^{2+} solution.

A double sigmoidal profile is obtained by plotting the copper reaction's E_{pc} *vs.* the Cu^{2+} molar equivalent added for both ligands (*insets* of Figures 33a and 33b). The inflection points indicate the reaction stoichiometry between these compounds, appearing at 0.47 ± 0.02 and 1.45 ± 0.06 for **Feizone** and 0.40 ± 0.03 and 1.39 ± 0.04 for **Ferfurone**. The first inflection point approximates to 0.5 in both cases, suggesting the 1:2 metal-to-ligands stoichiometry reaction, as viewed for **Ferfurone-Cu**, confirmed by crystallographic data, thermogravimetric analyses, and metal mass percentage by ICP-OES. A second inflection point, which approximates to 1.5 of Cu^{2+} molar equivalents, appears again for both copper(II) complexes, possibly pointing to a 3:2 metal-to-ligand stoichiometry, as seen for **Feizone-Zn**. Although furan has a significantly lower coordination power than pyridine, these side groups present in the ligands may participate in the metal coordination, perhaps giving rise to other coordination arrangement possibilities. However, additional research is still required to better understand other coordination possibilities of these systems.

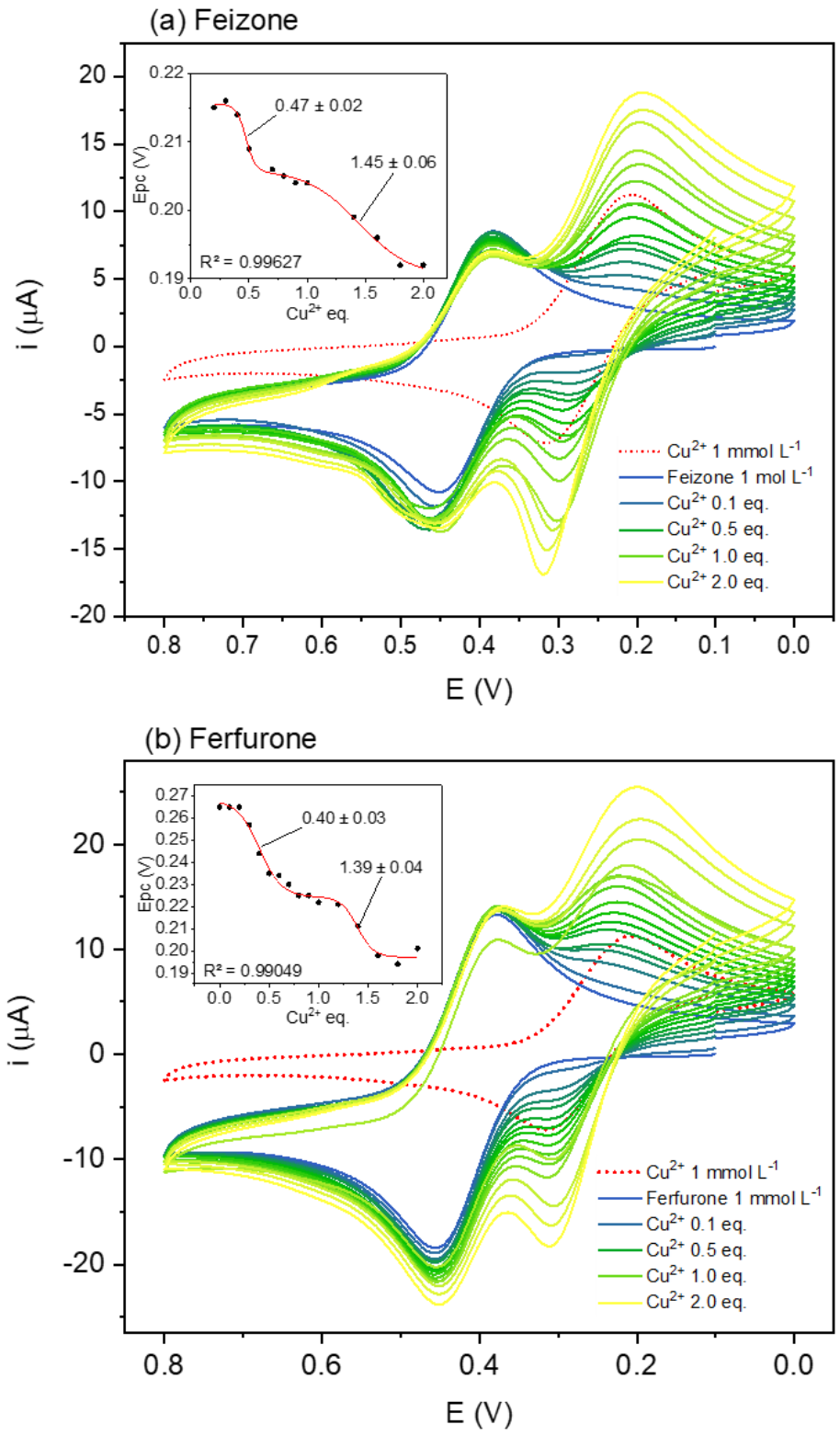

Figure 33. Cyclic voltammograms of 1.0 mmol L^{-1} of **Feizone** (a) and **Ferfurone** (b) with 0.1 mol L^{-1} NaCl in methanol/water 1:1 mixture (black dashed line), then progressively added Cu^{2+} solution until 2 molar equivalents (blue to green, to yellow lines) of the ligand. The voltammogram for the solution of Cu^{2+} 1 mmol L^{-1} in the same conditions (red dotted line) is present for comparison. *Insets:* E_{pc} *vs.* Cu^{2+} molar equivalent addition. Fitting was performed with a BiDoseResp function. Potentials *vs.* Ag/AgCl 3 mol L^{-1} KCl electrode.

7. Results and Discussion Part III – Pharmacological Parameters and Biological Studies

7.1 *In silico* Pharmacological Descriptors

In order to obtain relevant *in silico* pharmacological descriptors of these ligands, due to time management, it was chosen to use the Osiris Property Explorer™ software. This made possible a preliminary analysis of these ligands respecting their ability for prominent drugs.

Firstly, the molecular weight (MW) is considered, related to the ease with which these compounds can permeate through biological membranes. The bigger the molecular weight, the more difficult it is for the drug to cross cell membranes. Subsequently, log P and log S are analyzed. Log P stands for the octanol-water partition coefficient, representing the affinity with either a hydrophilic or lipophilic medium, while log S refers to the compound's solubility in aqueous solution.

These parameters infer the behavior of these molecules in the polar variety of environments on a physiological body. A balance between hydrophilicity and lipophilicity is ultimately desired for this type of drug, as such, it can't be highly lipophilic, which would cause its retention in the lipophilic cellular space, nor can it be excessively hydrophilic, which would result in great difficulty for this drug to cross the lipid bilayer of the biological membranes.

The TPSA stands for the topological polar surface area, which evaluates the degree of polarity of the molecule. The higher the concentration of partial charges in regions of the compounds, the greater its hydrophilic character, so the TPSA infers if the considered species would present elevated hydrophilicity, hampering the lipid penetration capacity.

Another crucial parameter for evaluating a drug candidate is its druglikeness. This metric is determined by comparing the molecular fragments of the candidate compound against a database of commercially available drugs and another database of non-drug compounds. The molecule is compared to a set of 3,300 commercial drugs and 15,000 chemical substances.

Lastly, the drug score combines druglikeness, Log P, log S, molecular weight, and toxicity risks into a single value. This allows a comprehensive assessment of the compound's overall potential to qualify as a drug, in terms of which, computing these parameters, the closest the drug score value is to 1, the more prominent the analyzed drug is. For drugs aiming to treat neuropathologies, the BBB is the most important biological barrier, as it fundamentally controls what gets inside the brain. The data for **Feizone** and **Ferfurone** along with the reference values of the stated parameters regarding BBB-crossing and cell permeability are shown in Table 9. (Kelder *et al.*, 1999; van de Waterbeemd *et al.*, 1998).

Table 9. Calculated descriptors of pharmacological relevance for the ligands studied. Reference values for the pharmacological descriptors for cell permeability and BBB-crossing are also present.

	Feizone	**Ferfurone**	**Cell permeability**	**BBB-crossing**
MW (g mol^{-1})	333.17	354.18	≤ 500	≤ 400
cLog P	1.81	2.00	−1 ≤ Log P ≤ 5	−1 ≤ Log P ≤ 5
cLog S	−2.74	−3.22	≥ −4	≥ −4
TPSA	54.35	54.60	≤ 140	≤ 90
Druglikeness	4.39	3.22	> 0	> 0
Drug-Score	0.33	0.88	–	–

The calculated parameters have identified that these compounds exhibit proper theoretical results regarding the crossing of biological membranes. The cLog S results are slightly lesser than the desirable but, hopefully, this can be bypassed in future studies using disposable techniques, such as structural changes or the preparation of inclusion complexes with more hydrophilic carriers. Their exceptional performance in key metrics suggests the potential of these molecules as promising drug candidates and warrant further investigation and development.

7.2 Superoxide Radical Scavenging Activity Study

Reactive oxygen species (ROS) are crucial contributors to oxidative stress in Alzheimer's disease (AD). Metals such as iron, copper, and aluminum facilitate the generation of free radicals, including the harmful hydroxyl radicals, which inflict severe damage on DNA, proteins, lipids, and carbohydrates. Oxidative stress arises predominantly from the transference of one electron to dioxygen (O_2) during the electron transport chain in mitochondria, resulting in the formation of anion radical superoxide ($O_2^{\bullet-}$), an important by-product of aerobic respiration. Superoxide can subsequently lead to the production of other ROS, as hydrogen peroxide (H_2O_2) and highly reactive hydroxyl radicals ($OH^{\bullet}$) (Nunomura *et al.*, 2001; Rival *et al.*, 2009).

Mitochondria generate superoxide radicals during normal respiration, with production increasing significantly when respiration is somehow compromised. While superoxide radicals have limited membrane permeability, their dismutation product, hydrogen peroxide, can easily diffuse through membranes. Crucially, in the presence of redox-active metals such as iron or copper, hydrogen peroxide becomes a precursor for the formation of hydroxyl radicals through Fenton or pseudo-Fenton reactions. Therefore, mitochondrial dysfunction can enhance the oxidative damage by both producing excess hydrogen peroxide and facilitating the release of heme iron into the cytosol by the lysosomal degradation of damaged organelles (Perry *et al.*, 2000).

The activities and expression of many natural antioxidant enzymes, including superoxide dismutase, glutathione peroxidase, glutathione reductase, and catalase, have been investigated in the context of AD and may partially contribute to reduce oxidative damage. While overall levels of superoxide dismutase are not consistently altered in AD (Markesbery & Carney, 1999), immunocytochemical studies have shown localized increases in superoxide dismutase and catalase specifically at the neurofibrillary tangles and senile plaques (Pappolla *et al.*, 1992). However, the disruption of copper homeostasis, leading to the accumulation of a substantial copper pool, may result in decreased glutathione levels. This can then enhance the cytotoxic effects of ROS by promoting copper's catalytic activity and, subsequently, increasing ROS production (Kozlowski *et al.*, 2012).

Fenton-like reactions produced by ferrocenyl-based compounds are widely known in the literature, being explored in anti-cancer and anti-biotic activities (Ornelas & Astruc, 2023), and they are believed to even boost the anti-malarial activity of ferroquine (Patra & Gasser, 2017). However, the AD-afflicted brain is already stressed by ROS and RNS generated by Fenton and Haber-Weiss reactions. In this manner, a possible drug to treat or diagnose AD could not contribute to this already-established oxidative stress. Nevertheless, ferrocene's cytotoxicity and generation of ROS is pointed to heavily depend on its redox potential (E^o). In terms of which, the lesser the potential, the higher the cytotoxicity (Věžník *et al.*, 2021). As viewed in the electrochemical characterization section of **Feizone** and **Ferfurone**, they present increased E^o, surpassing ferrocene in +0.088 V and +0.074 V. Additionally, *N*-acylhydrazones exhibit significant free radical scavenging activity, potentially attributed to their amide N–H group, which can donate a proton to solvent or, more probably, to radicals. Upon H^+ donation, the iminolate anion may undergo a one-electron oxidation, generating a hydrazone-derived radical, which is stabilized due to electron conjugation in its structure. The facts described above offer a reasonable explanation for the inhibition of ferroneyl's-mediated ROS generation.

To test the scavenging activity of **Feizone** and **Ferfurone**, the electrochemical production of superoxide radicals was chosen as the most convenient method. These radicals were generated by solubilizing molecular oxygen (O_2) from the air into a $TBAPF_6$ 0.1 mol L^{-1} DMF solution and subsequently running a cyclic voltammetry experiment, transferring an electron to O_2 in the cathodic process around –0.846 V *vs.* Ag/AgCl and losing it again in an anodic process at around –0.674 V, completing the cycle. Three voltammetric cycles were performed for each ligand concentration, as presented in Figure 34. This process allows a statistical treatment for the cycles, determining if the decrease in the current found in the anodic process, probably due to the destruction of the generated $O_2^{\bullet-}$ radicals before they can be re-oxidized, is statistically significant (Figure 34). The analysis showed a significant reduction of the anodic current peaks in the presence of every **Feizone** concentration tested, from 100 to 500 μmol L^{-1}, with a maximum decrease of 15.9% at 500 μmol L^{-1}. On the other hand, for **Ferfurone**, only at a concentration of 800 μmol L^{-1} the anodic peak showed a statistically significant difference, of 13.3%. As the concentrations of both

Feizone and **Ferfurone** increased, the anodic peak current decreased, indicating the depletion of $O_2^{\bullet-}$ due to its irreversible reaction with the ligands. The lower activity of **Ferfurone** may be related to its higher pK_a value, as depletion of the $O_2^{\bullet-}$ anion probably occurs by the protonation of these radicals to $HO_2^{\bullet}$. In the sequence, the radical $HO_2^{\bullet}$ generated can undergo dismutation, producing H_2O_2 and O_2.

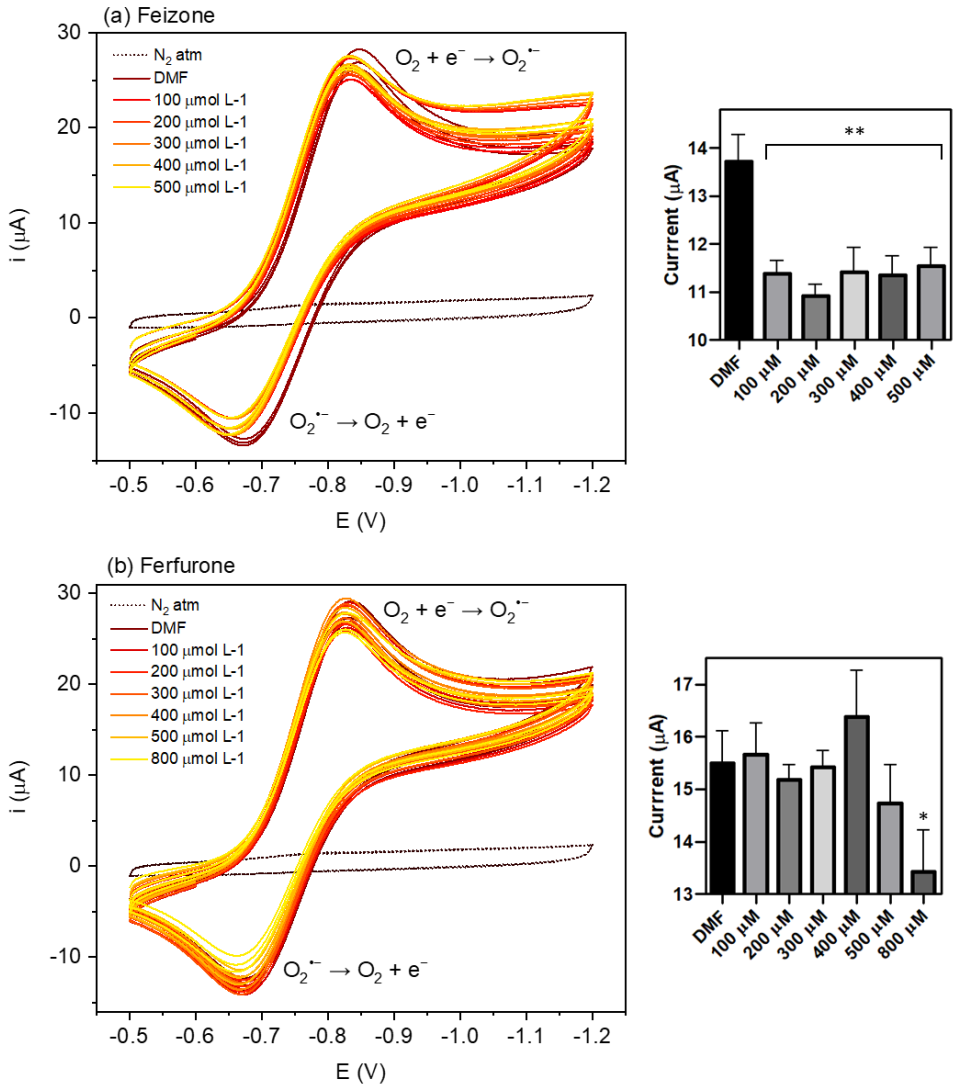

Figure 34. Cyclic voltammograms of $O_2/O_2^{\bullet-}$ redox couple in O_2 solution in DMF in the absence (brown line) and in the presence of different concentrations (red to yellow lines) of **Feizone** (a) and **Ferfurone** (b). The black dotted line represents the voltammogram recorded in N_2 atmosphere at the same conditions. Supporting electrolyte was 0.1 mol L^{-1} $TBAPF_6$ in DMF and the scan rate was 100 mV s^{-1}. On the right, is found a column graph of the peak anodic current of each concentration for the respective ligand. Statistically significant values are represented as *p < 0.05; **p < 0.01. Potentials *vs.* Ag/AgCl 3 mol L^{-1} KCl electrode.

7.3 Preliminary Study of the Interaction with $A\beta_{1-40}$ Peptide

Aβ peptides are produced from APP cleavage by β- and γ-secretases, a process known as the amyloidogenic pathway. The most significant Aβ species for AD are $A\beta_{1-40}$ and $A\beta_{1-42}$. Once produced, Aβ is secreted into the extracellular space as a monomer. Due to its sequence, Aβ (especially $A\beta_{1-42}$) has a strong tendency to aggregate in a concentration-dependent manner. As previously discussed, the soluble oligomeric forms of Aβ are the most neurotoxic, causing progressive synaptic and neuronal damage, disrupting neuronal metal homeostasis, and inducing oxidative injury. This leads to abnormal oligomerization, widespread neuronal dysfunction, and cell death associated with neurotransmitter deficits (Haass & Selkoe, 2007; Knopman *et al.*, 2021). Therefore, the proposed metallophores must capture the coordinated metals within the Aβ oligomers. Subsequently, to function as electrochemical probes and indicate the presence of widespread Aβ oligomers in the brain, they must associate with these peptides while electrochemically signaling this interaction.

To investigate the ligand-Aβ interaction, square-wave voltammetry was selected for its higher sensitivity, enabling analysis at lower concentrations of Aβ and ligands. $A\beta_{1-40}$ was chosen for this study because the tendency of $A\beta_{1-42}$ to aggregate would significantly interfere with data acquisition. Figure 35 displays the voltammograms for the interaction between $A\beta_{1-40}$ and both ligands.

The voltammograms show minor variances in the peak potential, of 0.01 V for **Feizone** and 0.02 V for **Ferfurone**, after the addition of 2 molar equivalents of $A\beta_{1-40}$. A more expressive change in these voltammograms is marked in the current peak (i_{peak}), which progressively rises throughout $A\beta_{1-40}$ addition. An exponential asymptote curve profile is observed by plotting the i_{peak} *vs.* $A\beta_{1-40}$ molar equivalent addition, suggesting a saturation in the interaction between ligand and peptide. For **Ferfurone**, this plot profile is observed with an apparent saturation at 2.0 $A\beta_{1-40}$ molar equivalent, suggesting each molecule of this ligand can interact with up to 2 peptides at once. Meanwhile, for **Feizone**, this plot profile is observed with scarce points, thus becoming less trustworthy, appearing with saturation at 0.5 $A\beta_{1-40}$ molar equivalent, indicating the saturation occurs at 1 peptide for 2 **Feizone** molecules.

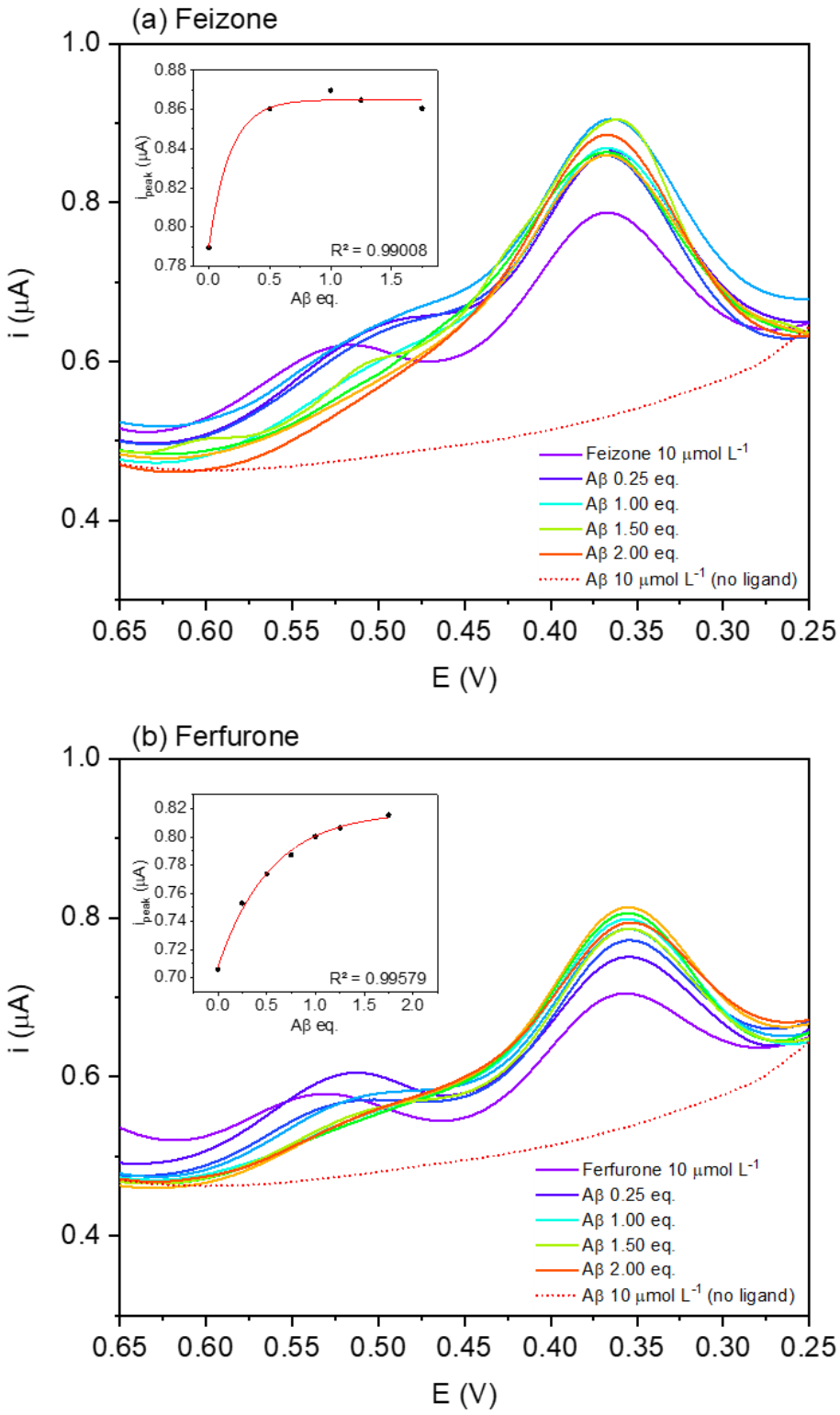

Figure 35. Square-wave voltammograms of 10 μmol L^{-1} of **Feizone** (a) and **Ferfurone** (b) with 0.1 mol L^{-1} NaCl in 1 % DMSO/HEPES buffer 10 mmol L^{-1} in pH 7.4 (violet line), then progressively added $A\beta_{1\text{-}40}$ aliquots until 2 molar equivalents (rainbow lines until red) of the ligand. The voltammogram for the solution of $A\beta_{1\text{-}40}$ 10 μmol L^{-1} in the same conditions (red dotted line) is present for comparison. Inset presents i_{peak} *vs.* $A\beta_{1\text{-}40}$ molar equivalent addition with an Asymptotic1 fitting. Potentials *vs.* Ag/AgCl 3 mol L^{-1} KCl electrode.

As previously discussed, two electrochemical processes are observed for the ligands within this potential range, the main ferrocenyl redox couple reaction and another reaction around +0.52 V. This second reaction does not come from remaining aldehyde in solution and is speculated to be a hydrazone inner electrochemical process. This process vanishes along with the addition of $A\beta_{1\text{-}40}$ solution, suggesting that the interaction, observed by the i_{peak} of ferrocenyl reaction, impairs this redox reaction. This leads to the conclusion that the hydrazone somehow participates in the interaction with the peptide. Some possible polar interactions with $A\beta_{1\text{-}40}$ are hydrogen bonds, between the hydrazone and amino acid groups of the peptide, as tyrosine, histidine, and serine; and apolar interaction as π-π stacking from aromatic groups in tyrosine and phenylalanine. The formation of H bonds with $A\beta_{1\text{-}40}$ may impair the iminolization of these compounds, suggesting that the electrochemical process coming from the hydrazone is connected to a free iminol group, as also seen in the **Feizone-Zn** complexation study through cyclic voltammetry.

8. Conclusions

In this work, two *N*-acylhydrazones were synthesized through a condensation reaction between ferrocenecarboxaldehyde and a pair of distinct *N*-acylhydrazides, namely, isoniazid and furan-2-hydrazide, each leading to a different ligand: **Feizone** and **Ferfurone**, respectively. From these ligands, three complexes were prepared, two copper(II) and a zinc(II) complex. Although none of these compounds are novel to the literature (except for another structure of **Ferfurone**, containing a crystallized methanol molecule), the motivation and some characterization made in this work bring new discussion on the properties and application of these compounds.

These ligands showed satisfactory ability to coordinate Cu^{2+} ions in solution at room temperature, but they require a strongly basic medium to coordinate Zn^{2+} species. This observation suggests that the deprotonation of the *N*-acylhydrazones' amide must occur to enhance the coordination capability of these ligands. The pK_a estimation through cyclic voltammetry resulted in 10.7 for **Feizone** and 11.0 for **Ferfurone**, indicating that, in physiological conditions, these ligands should have a selectivity for coordinating Cu^{2+} ions.

The hydrolytic stability was assessed, showing over 90% of the compounds' retainment after 12 h. This stability is configured by electron conjugation present in these ligands, which represent excellent characteristics for a desirable drug candidate. Additionally, photolytic stability was also evaluated, as a darkening in the solution's color was observed after exposure to light. After several experiments in this matter, we speculate a redox reaction between some solvents (such as DMF and DMSO) and the ferrocenyl group present in **Feizone** and **Ferfurone**.

Complexation studies through cyclic voltammetry showed double sigmoidal profiles on the analysis of peak currents *vs.* the concentration of the metal. These profiles suggest different coordination stoichiometries as the metal concentration increases. However, additional research is certainly necessary to better understand the chemical nature of the product(s) formed.

The theoretical pharmacologic parameters were obtained, presenting a great theoretical potential for these compounds in crossing biological membranes. The radical scavenging potentials of **Feizone** and **Ferfurone** were estimated toward

electrochemically generated superoxide radicals, showing a decrease of current magnitude of up to 15.9% (for 500 μmol L^{-1} of the ligand **Feizone**), and 13.3% (for 800 μmol L^{-1} of **Ferfurone**). These results translate into the successful (although low) activity in scavenging of radicals by the hydrazone group, which is crucial in this work's compounds, as ferrocene has been linked to oxygen radical production.

The square-wave voltammetry results on $A\beta_{1-40}$ interaction with the ligands resulted in gradual changes in the current magnitude of the ferrocenyl redox wave. These changes suggest the interaction of the ligands with this peptide. By analyzing the peak current *vs.* concentration of $A\beta_{1-40}$, an asymptotic curve demonstrates the saturation of ligands by Aβ. The results point to 2:1 and 1:2 ligand-to-Aβ interaction for ligands **Feizone** and **Ferfurone**, respectively. However, these are preliminary results and, although they point to the possibility of using the ferrocenyl process as an electrochemical probe for the interaction of **Feizone** and **Ferfurone** with Aβ, more accurate analyses are needed to confirm this potentiality.

The Aβ plaques along with the excessive amount of Cu^{2+} in the brain are important biomarkers of AD, a disease known for more than a century and for which there is still no cure. As stated in the previous paragraph, the electrochemical signals generated from the binding of ligands with these biomarkers demonstrate the potential of these *N*-acylhydrazones as electrochemical probes in the context of this disease. This could provide valuable insights into the presence and progression of AD, making these ligands useful tools for early diagnosis and patients' monitoring. Furthermore, their ability to selectively bind Cu^{2+} in a physiological environment suggests their potential effectiveness for the treatment of some biochemical changes associated with AD. As a result, these ligands could contribute significantly to the development of new diagnostic techniques, as well as therapeutic strategies aimed at mitigating the impact of Alzheimer's disease.

9. Bibliography

ADLARD, P. A.; CHERNY, R. A.; FINKELSTEIN, D. I.; GAUTIER, E. *et al.* Rapid Restoration of Cognition in Alzheimer's Transgenic Mice with 8-Hydroxy Quinoline Analogs Is Associated with Decreased Interstitial Aβ. **Neuron**, 59, n. 1, p. 43-55, 2008/07/10/ 2008.

ADLARD, P. A.; PARNCUTT, J. M.; FINKELSTEIN, D. I.; BUSH, A. I. Cognitive loss in zinc transporter-3 knock-out mice: a phenocopy for the synaptic and memory deficits of Alzheimer's disease? **J Neurosci**, 30, n. 5, p. 1631-1636, Feb 3 2010.

ALZHEIMER, A.; STELZMANN, R. A.; SCHNITZLEIN, H. N.; MURTAGH, F. R. An English translation of Alzheimer's 1907 paper, "Uber eine eigenartige Erkankung der Hirnrinde". **Clin Anat**, 8, n. 6, p. 429-431, 1995.

ANNAMALAI, B.; WON, J. S.; CHOI, S.; SINGH, I. *et al.* Role of S-nitrosoglutathione mediated mechanisms in tau hyper-phosphorylation. **Biochem Biophys Res Commun**, 458, n. 1, p. 214-219, Feb 27 2015.

APPEL, M.; FRICK, B.; IVANOV, A.; ELBERT, J. *et al.* Vibrational spectra of ferrocene, ferrocene-containing polymers and their oxidized compounds. **Journal of Physics: Conference Series**, 554, n. 1, p. 012008, 2014/11/10 2014.

ASTRUC, D. Why is Ferrocene so Exceptional? **European Journal of Inorganic Chemistry**, 2017, n. 1, p. 6-29, 2017/01/03 2017.

BABIJ, N. R.; MCCUSKER, E. O.; WHITEKER, G. T.; CANTURK, B. *et al.* NMR Chemical Shifts of Trace Impurities: Industrially Preferred Solvents Used in Process and Green Chemistry. **Organic Process Research & Development**, 20, n. 3, p. 661-667, 2016/03/18 2016.

BAREGGI, S. R.; CORNELLI, U. Clioquinol: review of its mechanisms of action and clinical uses in neurodegenerative disorders. **CNS Neurosci Ther**, 18, n. 1, p. 41-46, Jan 2012.

BARNHAM, K. J.; BUSH, A. I. Metals in Alzheimer's and Parkinson's diseases. **Curr Opin Chem Biol**, 12, n. 2, p. 222-228, Apr 2008.

BEERS, J.; GLERUM, D. M.; TZAGOLOFF, A. Purification, Characterization, and Localization of Yeast Cox17p, a Mitochondrial Copper Shuttle*. **Journal of Biological Chemistry**, 272, n. 52, p. 33191-33196, 1997/12/26/ 1997.

BENARROCH, E. E. Glutamatergic synaptic plasticity and dysfunction in Alzheimer disease: Emerging mechanisms. **Neurology**, 91, n. 3, p. 125-132, Jul 17 2018.

BHATT, V. Chapter 8 - Metal Carbonyls. *In*: BHATT, V. (Ed.). **Essentials of Coordination Chemistry**: Academic Press, 2016. p. 191-236.

BIESCHKE, J.; HERBST, M.; WIGLENDA, T.; FRIEDRICH, R. P. *et al.* Small-molecule conversion of toxic oligomers to nontoxic β-sheet-rich amyloid fibrils. **Nat Chem Biol**, 8, n. 1, p. 93-101, Nov 20 2011.

BIOT, C.; GLORIAN, G.; MACIEJEWSKI, L. A.; BROCARD, J. S. *et al.* Synthesis and Antimalarial Activity in Vitro and in Vivo of a New Ferrocene−Chloroquine Analogue. **Journal of Medicinal Chemistry**, 40, n. 23, p. 3715-3718, 1997/11/01 1997.

BLENNOW, K.; DUBOIS, B.; FAGAN, A. M.; LEWCZUK, P. *et al.* Clinical utility of cerebrospinal fluid biomarkers in the diagnosis of early Alzheimer's disease. **Alzheimers Dement**, 11, n. 1, p. 58-69, Jan 2015.

BOGDAN, M.; BRUGGER, D.; ROSENSTIEL, W.; SPEISER, B. Estimation of diffusion coefficients from voltammetric signals by support vector and gaussian process regression. **J Cheminform**, 6, p. 30, 2014.

BOOM, A.; AUTHELET, M.; DEDECKER, R.; FRÉDÉRICK, C. *et al.* Bimodal modulation of tau protein phosphorylation and conformation by extracellular Zn2+ in human-tau transfected cells. **Biochimica et Biophysica Acta (BBA) - Molecular Cell Research**, 1793, n. 6, p. 1058-1067, 2009/06/01/ 2009.

BRAAK, H.; BRAAK, E. Neuropathological stageing of Alzheimer-related changes. **Acta Neuropathol**, 82, n. 4, p. 239-259, 1991.

BREIJYEH, Z.; KARAMAN, R. Comprehensive Review on Alzheimer's Disease: Causes and Treatment. **Molecules**, 25, n. 24, Dec 8 2020.

BUSH, A. I. The metallobiology of Alzheimer's disease. **Trends Neurosci**, 26, n. 4, p. 207-214, Apr 2003.

BUSH, A. I.; PETTINGELL, W. H.; MULTHAUP, G.; D PARADIS, M. *et al.* Rapid induction of Alzheimer A beta amyloid formation by zinc. **Science**, 265, n. 5177, p. 1464-1467, Sep 2 1994.

CARVALHO, A.; BARBOSA, B. M.; FLORES, J. S.; DO CARMO GONÇALVES, P. *et al.* New mescaline-related N-acylhydrazone and its unsubstituted benzoyl derivative: Promising metallophores for copper-associated deleterious effects relief in Alzheimer's disease. **Journal of Inorganic Biochemistry**, 238, p. 112033, 2023/01/01/ 2023.

CHAUDHARY, A.; POONIA, K. The redox mechanism of ferrocene and its phytochemical and biochemical compounds in anticancer therapy: A mini review. **Inorganic Chemistry Communications**, 134, p. 109044, 2021/12/01/ 2021.

CHEN, P.; MIAH, M.; ASCHNER, M. Metals and Neurodegeneration [version 1; peer review: 3 approved]. **F1000Research**, 5, n. 366, 2016.

CHERNY, R. A.; ATWOOD, C. S.; XILINAS, M. E.; GRAY, D. N. *et al.* Treatment with a copper-zinc chelator markedly and rapidly inhibits beta-amyloid accumulation in Alzheimer's disease transgenic mice. **Neuron**, 30, n. 3, p. 665-676, Jun 2001.

CHOWDHURY, S. Monoclonal Antibody Treatments for Alzheimer's Disease: Aducanumab and Lecanemab. **Discoveries**, 11, n. 3, 2023.

CHRISTIE, J. E.; SHERING, A.; FERGUSON, J.; GLEN, A. I. Physostigmine and arecoline: effects of intravenous infusions in Alzheimer presenile dementia. **Br J Psychiatry**, 138, p. 46-50, Jan 1981.

COLE, T. B.; WENZEL, H. J.; KAFER, K. E.; SCHWARTZKROIN, P. A. *et al.* Elimination of zinc from synaptic vesicles in the intact mouse brain by disruption of the ZnT3 gene. **Proc Natl Acad Sci U S A**, 96, n. 4, p. 1716-1721, Feb 16 1999.

COMPTON, R. G.; BANKS, C. E. **Understanding Voltammetry**. World Scientific, 2007. (G - Reference,Information and Interdisciplinary Subjects Series. 9789812706256.

CONNELLY, N. G.; GEIGER, W. E. Chemical Redox Agents for Organometallic Chemistry. **Chemical Reviews**, 96, n. 2, p. 877-910, 1996/01/01 1996.

CUKIERMAN, D. S.; ACCARDO, E.; GOMES, R. G.; DE FALCO, A. *et al.* Aroylhydrazones constitute a promising class of 'metal-protein attenuating compounds' for the treatment of Alzheimer's disease: a proof-of-concept based on the study of the interactions between zinc(II) and pyridine-2-carboxaldehyde isonicotinoyl hydrazone. **JBIC Journal of Biological Inorganic Chemistry**, 23, n. 8, p. 1227-1241, 2018/12/01 2018.

CUKIERMAN, D. S.; EVANGELISTA, B. N.; NETO, C. C.; FRANCO, C. H. J. *et al.* Mildness in preparative conditions directly affects the otherwise straightforward syntheses outcome of Schiff-base isoniazid derivatives: Aroylhydrazones and their solvolysis-related dihydrazones. **Journal of Molecular Structure**, 1228, p. 129437, 2021/03/15/ 2021.

CUKIERMAN, D. S.; LÁZARO, D. F.; SACCO, P.; FERREIRA, P. R. *et al.* X1INH, an improved next-generation affinity-optimized hydrazonic ligand, attenuates abnormal copper(i)/copper(ii)-α-Syn interactions and affects protein aggregation in a cellular model of synucleinopathy. **Dalton Transactions**, 49, n. 45, p. 16252-16267, 2020. 10.1039/D0DT01138J.

CUKIERMAN, D. S.; PINHEIRO, A. B.; CASTIÑEIRAS-FILHO, S. L. P.; DA SILVA, A. S. P. *et al.* A moderate metal-binding hydrazone meets the criteria for a bioinorganic approach towards Parkinson's disease: Therapeutic potential, blood-brain barrier crossing evaluation and preliminary toxicological studies. **Journal of Inorganic Biochemistry**, 170, p. 160-168, 2017/05/01/ 2017.

CUKIERMAN, D. S.; REY, N. A. Tridentate N-Acylhydrazones as Moderate Ligands for the Potential Management of Cognitive Decline Associated With Metal-Enhanced Neuroaggregopathies. **Frontiers in Neurology**, 13, 2022-February-16 2022. Opinion.

DANYSZ, W.; PARSONS, C. G.; MOBIUS, H. J.; STOFFLER, A. *et al.* Neuroprotective and symptomatological action of memantine relevant for Alzheimer's disease--a unified glutamatergic hypothesis on the mechanism of action. **Neurotox Res**, 2, n. 2-3, p. 85-97, 2000.

DAVIES, P.; MALONEY, A. J. Selective loss of central cholinergic neurons in Alzheimer's disease. **Lancet**, 2, n. 8000, p. 1403, Dec 25 1976.

DE CALIGNON, A.; POLYDORO, M.; SUÁREZ-CALVET, M.; WILLIAM, C. *et al.* Propagation of tau pathology in a model of early Alzheimer's disease. **Neuron**, 73, n. 4, p. 685-697, Feb 23 2012.

DE FALCO, A.; CUKIERMAN, D. S.; HAUSER-DAVIS, R. A.; REY, N. A. ALZHEIMER'S DISEASE: ETIOLOGICAL HYPOTHESES AND TREATMENT PERSPECTIVES. **Química Nova**, 39, n. 1, 2016.

DE FALCO, A.; KINCHESKI, G. C.; ATRIÁN-BLASCO, E.; HUREAU, C. *et al.* The aroylhydrazone INHHQ prevents memory impairment induced by Alzheimer's-linked amyloid-β oligomers in mice. **Behav Pharmacol**, 31, n. 8, p. 738-747, Dec 2020.

DE FREITAS, L. V.; DA SILVA, C. C.; ELLENA, J.; COSTA, L. A. *et al.* Structural and vibrational study of 8-hydroxyquinoline-2-carboxaldehyde isonicotinoyl hydrazone--a potential metal-protein attenuating compound (MPAC) for the treatment of Alzheimer's disease. **Spectrochim Acta A Mol Biomol Spectrosc**, 116, p. 41-48, Dec 2013.

DELACOURTE, A.; DAVID, J. P.; SERGEANT, N.; BUÉE, L. *et al.* The biochemical pathway of neurofibrillary degeneration in aging and Alzheimer's disease. **Neurology**, 52, n. 6, p. 1158-1165, Apr 12 1999.

DHILLON, S. Aducanumab: First Approval. **Drugs**, 81, n. 12, p. 1437-1443, 2021/08/01 2021.

DIANA, E.; ROSSETTI, R.; STANGHELLINI, P. L.; KETTLE, S. F. A. Vibrational Study of (η5-Cyclopentadienyl)metal Complexes. **Inorganic Chemistry**, 36, n. 3, p. 382-391, 1997/01/01 1997.

DODANI, S. C.; FIRL, A.; CHAN, J.; NAM, C. I. *et al.* Copper is an endogenous modulator of neural circuit spontaneous activity. **Proceedings of the National Academy of Sciences**, 111, n. 46, p. 16280-16285, 2014/11/18 2014.

DOLOMANOV, O. V.; BOURHIS, L. J.; GILDEA, R. J.; HOWARD, J. A. K. *et al.* OLEX2: a complete structure solution, refinement and analysis program. **Journal of Applied Crystallography**, 42, n. 2, p. 339-341, 2009.

DOS SANTOS FILHO, J. M.; DE SOUZA CASTRO, M. V. B. Synthesis, structural characterization, and antimicrobial activity of novel ferrocene-N-acyl hydrazones designed by means of molecular simplification strategy Celebrating the 100th anniversary of the birth of Professor Paulo Freire. **Journal of Organometallic Chemistry**, 979, p. 122488, 2022/11/15/ 2022.

DRACHMAN, D. A.; SAHAKIAN, B. J. Memory and cognitive function in the elderly. A preliminary trial of physostigmine. **Arch Neurol**, 37, n. 10, p. 674-675, Oct 1980.

DUJARDIN, S.; COMMINS, C.; LATHUILIERE, A.; BEEREPOOT, P. *et al.* Tau molecular diversity contributes to clinical heterogeneity in Alzheimer's disease. **Nat Med**, 26, n. 8, p. 1256-1263, Aug 2020.

EDWARDS, E. I.; EPTON, R.; MARR, G. Organometallic derivatives of penicillins and cephalosporins a new class of semi-synthetic antibiotics. **Journal of Organometallic Chemistry**, 85, n. 2, p. C23-C25, 1975/02/04/ 1975.

EDWARDS, E. I.; EPTON, R.; MARR, G. 1,1′-Ferrocenyldiacetic Acid Anhydride and its Use in the preparation of heteroannularly substituted ferrocenyl-penicillins and -cephalosporins. **Journal of Organometallic Chemistry**, 122, n. 3, p. C49-C53, 1976/12/21/ 1976.

EFTEKHARZADEH, B.; DAIGLE, J. G.; KAPINOS, L. E.; COYNE, A. *et al.* Tau Protein Disrupts Nucleocytoplasmic Transport in Alzheimer's Disease. **Neuron**, 99, n. 5, p. 925-940.e927, Sep 5 2018.

ELGRISHI, N.; ROUNTREE, K. J.; MCCARTHY, B. D.; ROUNTREE, E. S. *et al.* A Practical Beginner's Guide to Cyclic Voltammetry. **Journal of Chemical Education**, 95, n. 2, p. 197-206, 2018/02/13 2018.

FABBRIZZI, L. The ferrocenium/ferrocene couple: a versatile redox switch. **ChemTexts**, 6, n. 4, p. 22, 2020/10/09 2020.

FARRUGIA, L. WinGX and ORTEP for Windows: an update. **Journal of Applied Crystallography**, 45, n. 4, p. 849-854, 2012.

FERNÁNDEZ-PALACIOS, S.; MATAMOROS, E.; MORATO ROJAS, I.; LÓPEZ NAVARRETE, J. T. *et al.* New Insights into Acylhydrazones E/Z Isomerization: An Experimental and Theoretical Approach. **Int J Mol Sci**, 24, n. 19, Sep 29 2023.

FERREIRA, S. T.; KLEIN, W. L. The Aβ oligomer hypothesis for synapse failure and memory loss in Alzheimer's disease. **Neurobiol Learn Mem**, 96, n. 4, p. 529-543, Nov 2011.

FICA-CONTRERAS, S. M.; SHUSTER, S. O.; DURFEE, N. D.; BOWE, G. J. K. *et al.* Glycation of Lys-16 and Arg-5 in amyloid-β and the presence of Cu2+ play a major role in the oxidative stress mechanism of Alzheimer's disease. **JBIC Journal of Biological Inorganic Chemistry**, 22, n. 8, p. 1211-1222, 2017/12/01 2017.

FISCHER, E. O.; PFAB, W. Cyclopentadien-Metallkomplexe, ein neuer Typ metallorganischer Verbindungen. 7, n. 7, p. 377-379, 1952.

FREDERICKSON, C. J.; KOH, J.-Y.; BUSH, A. I. The neurobiology of zinc in health and disease. **Nature Reviews Neuroscience**, 6, n. 6, p. 449-462, 2005/06/01 2005.

GAGGELLI, E.; KOZLOWSKI, H.; VALENSIN, D.; VALENSIN, G. Copper Homeostasis and Neurodegenerative Disorders (Alzheimer's, Prion, and

Parkinson's Diseases and Amyotrophic Lateral Sclerosis). **Chemical Reviews**, 106, n. 6, p. 1995-2044, 2006/06/01 2006.

GALIĆ, N.; PERIĆ, B.; KOJIĆ-PRODIĆ, B.; CIMERMAN, Z. Structural and spectroscopic characteristics of aroylhydrazones derived from nicotinic acid hydrazide. **Journal of Molecular Structure**, 559, n. 1, p. 187-194, 2001/01/09/ 2001.

GALLARDO, G.; HOLTZMAN, D. M. Amyloid-β and Tau at the Crossroads of Alzheimer's Disease. **Adv Exp Med Biol**, 1184, p. 187-203, 2019.

GAMOV, G. A.; KHODOV, I. A.; BELOV, K. V.; ZAVALISHIN, M. N. *et al.* Spatial structure, thermodynamics and kinetics of formation of hydrazones derived from pyridoxal 5′-phosphate and 2-furoic, thiophene-2-carboxylic hydrazides in solution. **Journal of Molecular Liquids**, 283, p. 825-833, 2019/06/01/ 2019.

GARKUSHA, O. G.; LOKSHIN, B. V.; BORISOV, G. K. Vibrational spectra and structure of dicyclopentadienylzinc. **Journal of Organometallic Chemistry**, 553, n. 1, p. 59-65, 1998/02/25/ 1998.

GEARY, W. J. The use of conductivity measurements in organic solvents for the characterisation of coordination compounds. **Coordination Chemistry Reviews**, 7, n. 1, p. 81-122, 1971/10/01/ 1971.

GOMES, L. M. F.; VIEIRA, R. P.; JONES, M. R.; WANG, M. C. P. *et al.* 8-Hydroxyquinoline Schiff-base compounds as antioxidants and modulators of copper-mediated Aβ peptide aggregation. **Journal of Inorganic Biochemistry**, 139, p. 106-116, 2014/10/01/ 2014.

GREENAMYRE, J. T.; YOUNG, A. B. Excitatory amino acids and Alzheimer's disease. **Neurobiol Aging**, 10, n. 5, p. 593-602, Sep-Oct 1989.

GUPTA, S. R.; MOURYA, P.; SINGH, M. M.; SINGH, V. P. Synthesis, structural, electrochemical and corrosion inhibition properties of two new ferrocene Schiff bases derived from hydrazides. **Journal of Organometallic Chemistry**, 767, p. 136-143, 2014/09/15/ 2014.

HAASS, C.; SELKOE, D. J. Soluble protein oligomers in neurodegeneration: lessons from the Alzheimer's amyloid beta-peptide. **Nat Rev Mol Cell Biol**, 8, n. 2, p. 101-112, Feb 2007.

HAILE, F.; LEE, K. EE33 Cost-Effectiveness of Aducanumab, Lecanemab, and Donanemab for Early Alzheimer Disease in the US. **Value in Health**, 27, n. 6, Supplement, p. S63, 2024/06/01/ 2024.

HANE, F.; LEONENKO, Z. Effect of Metals on Kinetic Pathways of Amyloid-β Aggregation. **Biomolecules**, v.4, n. 1, p. 101-116, DOI: 10.3390/biom4010101.

HANE, F.; TRAN, G.; ATTWOOD, S. J.; LEONENKO, Z. Cu(2+) affects amyloid-β (1-42) aggregation by increasing peptide-peptide binding forces. **PLoS One**, 8, n. 3, p. e59005, 2013.

HARDY, J. A.; HIGGINS, G. A. Alzheimer's disease: the amyloid cascade hypothesis. **Science**, 256, n. 5054, p. 184-185, Apr 10 1992.

HAUSER-DAVIS, R. A.; DE FREITAS, L. V.; CUKIERMAN, D. S.; CRUZ, W. S. *et al.* Disruption of zinc and copper interactions with Aβ(1–40) by a non-toxic, isoniazid-derived, hydrazone: a novel biometal homeostasis restoring agent in Alzheimer's disease therapy?†. **Metallomics**, 7, n. 5, p. 743-747, 2015.

HOERNKE, M.; KOKSCH, B.; BREZESINSKI, G. Influence of the hydrophobic interface and transition metal ions on the conformation of amyloidogenic model peptides. **Biophys Chem**, 150, n. 1-3, p. 64-72, Aug 2010.

HOLTZMAN, D. M.; MORRIS, J. C.; GOATE, A. M. Alzheimer's disease: the challenge of the second century. **Sci Transl Med**, 3, n. 77, p. 77sr71, Apr 6 2011.

HORE, P. J. **Nuclear Magnetic Resonance**. Oxford University Press, 2015. (Oxford chemistry primers. 9780191849480.

HUANG, L.-K.; KUAN, Y.-C.; LIN, H.-W.; HU, C.-J. Clinical trials of new drugs for Alzheimer disease: a 2020–2023 update. **Journal of Biomedical Science**, 30, n. 1, p. 83, 2023/10/02 2023.

HUANG, Y.; WU, Z.; CAO, Y.; LANG, M. *et al.* Zinc Binding Directly Regulates Tau Toxicity Independent of Tau Hyperphosphorylation. **Cell Reports**, 8, n. 3, p. 831-842, 2014/08/07/ 2014.

KALITA, J.; KUMAR, V.; MISRA, U. K.; BORA, H. K. Memory and Learning Dysfunction Following Copper Toxicity: Biochemical and

Immunohistochemical Basis. **Molecular Neurobiology**, 55, n. 5, p. 3800-3811, 2018/05/01 2018.

KÁSA, P.; RAKONCZAY, Z.; GULYA, K. The cholinergic system in Alzheimer's disease. **Prog Neurobiol**, 52, n. 6, p. 511-535, Aug 1997.

KEALY, T. J.; PAUSON, P. L. A New Type of Organo-Iron Compound. **Nature**, 168, n. 4285, p. 1039-1040, 1951/12/01 1951.

KELDER, J.; GROOTENHUIS, P. D.; BAYADA, D. M.; DELBRESSINE, L. P. *et al.* Polar molecular surface as a dominating determinant for oral absorption and brain penetration of drugs. **Pharm Res**, 16, n. 10, p. 1514-1519, Oct 1999.

KHARKAR, S. P.; DUTTA, K. A. Metal Protein Attenuating Compounds (MPACs): An Emerging Approach for the Treatment of Neurodegenerative Disorders. **Current Bioactive Compounds**, 4, n. 2, p. 57-67, 2008.

KIM, I.-S.; JIN, I.; YOON, H.-S. Decarbonylated cyclophilin A Cpr1 protein protects Saccharomyces cerevisiae KNU5377Y when exposed to stress induced by menadione. **Cell Stress and Chaperones**, 16, n. 1, p. 1-14, 2011/01/01/ 2011.

KNOPMAN, D. S.; AMIEVA, H.; PETERSEN, R. C.; CHÉTELAT, G. *et al.* Alzheimer disease. **Nat Rev Dis Primers**, 7, n. 1, p. 33, May 13 2021.

KOFFIE, R. M.; HYMAN, B. T.; SPIRES-JONES, T. L. Alzheimer's disease: synapses gone cold. **Mol Neurodegener**, 6, n. 1, p. 63, Aug 26 2011.

KOZLOWSKI, H.; LUCZKOWSKI, M.; REMELLI, M.; VALENSIN, D. Copper, zinc and iron in neurodegenerative diseases (Alzheimer's, Parkinson's and prion diseases). **Coordination Chemistry Reviews**, 256, n. 19, p. 2129-2141, 2012/10/01/ 2012.

KRISHNAMOORTHY, P.; SATHYADEVI, P.; BUTORAC, R. R.; COWLEY, A. H. *et al.* Copper(i) and nickel(ii) complexes with 1 : 1 vs. 1 : 2 coordination of ferrocenyl hydrazone ligands: Do the geometry and composition of complexes affect DNA binding/cleavage, protein binding, antioxidant and cytotoxic activities? **Dalton Transactions**, 41, n. 15, p. 4423-4436, 2012. 10.1039/C2DT11938B.

LAMBERT, M. P.; BARLOW, A. K.; CHROMY, B. A.; EDWARDS, C. *et al.* Diffusible, nonfibrillar ligands derived from Abeta1-42 are potent central

nervous system neurotoxins. **Proc Natl Acad Sci U S A**, 95, n. 11, p. 6448-6453, May 26 1998.

LAWRENCE, M. A. W.; LORRAINE, S. C.; WILSON, K.-A.; WILSON, K. Review: Voltammetric properties and applications of hydrazones and azo moieties. **Polyhedron**, 173, p. 114111, 2019/11/15/ 2019.

LEE, J. Y.; COLE, T. B.; PALMITER, R. D.; SUH, S. W. *et al.* Contribution by synaptic zinc to the gender-disparate plaque formation in human Swedish mutant APP transgenic mice. **Proc Natl Acad Sci U S A**, 99, n. 11, p. 7705-7710, May 28 2002.

LINCOLN, S. F. Mechanistic Studies of Metal Aqua Ions: A Semi-Historical Perspective. **Helvetica Chimica Acta**, 88, n. 3, p. 523-545, 2005/03/01 2005.

LOEV, B.; FLORES, M. Notes- Ferrocene Derivatives. **The Journal of Organic Chemistry**, 26, n. 9, p. 3595-3595, 1961/09/01 1961.

LU, C.; GUO, Y.; YAN, J.; LUO, Z. *et al.* Design, synthesis, and evaluation of multitarget-directed resveratrol derivatives for the treatment of Alzheimer's disease. **J Med Chem**, 56, n. 14, p. 5843-5859, Jul 25 2013.

LUDWIG, B. S.; CORREIA, J. D. G.; KÜHN, F. E. Ferrocene derivatives as anti-infective agents. **Coordination Chemistry Reviews**, 396, p. 22-48, 2019/10/01/ 2019.

LYUBARTSEVA, G.; SMITH, J. L.; MARKESBERY, W. R.; LOVELL, M. A. Alterations of Zinc Transporter Proteins ZnT-1, ZnT-4 and ZnT-6 in Preclinical Alzheimer's Disease Brain. **Brain Pathology**, 20, n. 2, p. 343-350, 2010/03/01 2010.

MACRAE, C. F.; BRUNO, I. J.; CHISHOLM, J. A.; EDGINGTON, P. R. *et al.* Mercury CSD 2.0 - new features for the visualization and investigation of crystal structures. **Journal of Applied Crystallography**, 41, n. 2, p. 466-470, 2008.

MANCINO, A. M.; HINDO, S. S.; KOCHI, A.; LIM, M. H. Effects of clioquinol on metal-triggered amyloid-beta aggregation revisited. **Inorg Chem**, 48, n. 20, p. 9596-9598, Oct 19 2009.

MARET, W. Oxidative metal release from metallothionein via zinc-thiol/disulfide interchange. **Proceedings of the National Academy of Sciences**, 91, n. 1, p. 237-241, 1994/01/04 1994.

MARKESBERY, W. R.; CARNEY, J. M. Oxidative alterations in Alzheimer's disease. **Brain Pathol**, 9, n. 1, p. 133-146, Jan 1999.

MATSUDA, H.; AYABE, Y. Zur Theorie der Randles-Sevčikschen Kathodenstrahl-Polarographie. **Zeitschrift für Elektrochemie, Berichte der Bunsengesellschaft für physikalische Chemie**, 59, n. 6, p. 494-503, 1955/08/01 1955.

MCCALL, K. A.; HUANG, C.-c.; FIERKE, C. A. Function and Mechanism of Zinc Metalloenzymes. **The Journal of Nutrition**, 130, n. 5, p. 1437S-1446S, 2000/05/01/ 2000.

MORJAN, R. Y.; MKADMH, A. M.; BEADHAM, I.; ELMANAMA, A. A. *et al.* Antibacterial activities of novel nicotinic acid hydrazides and their conversion into N-acetyl-1,3,4-oxadiazoles. **Bioorg Med Chem Lett**, 24, n. 24, p. 5796-5800, Dec 15 2014.

MOURA, F. d. S.; SOBRINHO, Y. S.; STELLET, C.; SERNA, J. D. P. *et al.* Copper(ii) complexes of a furan-containing aroylhydrazonic ligand: syntheses, structural studies, solution chemistry and interaction with HSA. **Dalton Transactions**, 52, n. 47, p. 17731-17746, 2023. 10.1039/D3DT02597G.

MULTHAUP, G.; SCHLICKSUPP, A.; HESSE, L.; BEHER, D. *et al.* The Amyloid Precursor Protein of Alzheimer's Disease in the Reduction of Copper(II) to Copper(I). **Science**, 271, n. 5254, p. 1406-1409, 1996/03/08 1996.

NAKAMOTO, K. **Infrared and Raman Spectra of Inorganic and Coordination Compounds, Part B: Applications in Coordination, Organometallic, and Bioinorganic Chemistry**. Wiley, 2009. (Infrared and Raman Spectra of Inorganic and Coordination Compounds. 9780470405871.

NOH, D.-Y.; LEE, H.-J.; UNDERBILL, A. E. Ferrocene-containing vt compound as a new molecular donor. **Synthetic Metals**, 102, n. 1, p. 1698, 1999/06/01/ 1999.

NUNOMURA, A.; PERRY, G.; ALIEV, G.; HIRAI, K. *et al.* Oxidative Damage Is the Earliest Event in Alzheimer Disease. **Journal of Neuropathology & Experimental Neurology**, 60, n. 8, p. 759-767, 2001.

ORNELAS, C.; ASTRUC, D. Ferrocene-Based Drugs, Delivery Nanomaterials and Fenton Mechanism: State of the Art, Recent

Developments and Prospects. **Pharmaceutics**, v.15, n. 8, DOI: 10.3390/pharmaceutics15082044.

ORR, M. E.; ODDO, S. Autophagic/lysosomal dysfunction in Alzheimer's disease. **Alzheimer's Research & Therapy**, 5, n. 5, p. 53, 2013/10/29 2013.

OUTTEN, C. E.; O'HALLORAN, T. V. Femtomolar sensitivity of metalloregulatory proteins controlling zinc homeostasis. **Science**, 292, n. 5526, p. 2488-2492, 2001. Article.

PAGE, J. A.; WILKINSON, G. The Polarographic Chemistry of Ferrocene, Ruthenocene and the Metal Hydrocarbon Ions. **Journal of the American Chemical Society**, 74, n. 23, p. 6149-6150, 1952/12/01 1952.

PAPPOLLA, M. A.; OMAR, R. A.; KIM, K. S.; ROBAKIS, N. K. Immunohistochemical evidence of oxidative [corrected] stress in Alzheimer's disease. **Am J Pathol**, 140, n. 3, p. 621-628, Mar 1992.

PARDRIDGE, W. M. Alzheimer's disease drug development and the problem of the blood-brain barrier. **Alzheimers Dement**, 5, n. 5, p. 427-432, Sep 2009.

PARSONS, C. G.; STÖFFLER, A.; DANYSZ, W. Memantine: a NMDA receptor antagonist that improves memory by restoration of homeostasis in the glutamatergic system--too little activation is bad, too much is even worse. **Neuropharmacology**, 53, n. 6, p. 699-723, Nov 2007.

PATIL, S. R.; KANTAK, U. N.; SEN, D. N. Some ferrocenyl aroyl hydrazones and their copper(II) complexes. **Inorganica Chimica Acta**, 63, p. 261-265, 1982/01/01/ 1982.

PATRA, M.; GASSER, G. The medicinal chemistry of ferrocene and its derivatives. **Nature Reviews Chemistry**, 1, n. 9, p. 0066, 2017/09/06 2017.

PERRY, G.; NUNOMURA, A.; HIRAI, K.; TAKEDA, A. *et al.* Oxidative damage in Alzheimer's disease: the metabolic dimension. **Int J Dev Neurosci**, 18, n. 4-5, p. 417-421, Jul-Aug 2000.

PHILLIPS, L.; LACEY, A. R.; COOPER, M. K. Analysis of substituted ferrocenes by infrared spectroscopy. **Journal of the Chemical Society, Dalton Transactions**, n. 5, p. 1383-1391, 1988. 10.1039/DT9880001383.

POOLER, A. M.; NOBLE, W.; HANGER, D. P. A role for tau at the synapse in Alzheimer's disease pathogenesis. **Neuropharmacology**, 76 Pt A, p. 1-8, Jan 2014.

PRINCE, M.; ALI, G. C.; GUERCHET, M.; PRINA, A. M. *et al.* Recent global trends in the prevalence and incidence of dementia, and survival with dementia. **Alzheimers Res Ther**, 8, n. 1, p. 23, Jul 30 2016.

PURANDARA, H.; RAGHAVENDRA, S.; FORO, S.; PATIL, P. *et al.* Synthesis, spectroscopic characterization, crystal structure, Hirshfeld surface analysis and third-order nonlinear optical properties of 2-(4-chlorophenoxy)-N'-[(1E)-1-(4-methylphenyl) ethylidene] acetohydrazide. **Journal of Molecular Structure**, 1185, p. 205-211, 2019/06/05/ 2019.

PUZZO, D.; PRIVITERA, L.; LEZNIK, E.; FÀ, M. *et al.* Picomolar amyloid-beta positively modulates synaptic plasticity and memory in hippocampus. **J Neurosci**, 28, n. 53, p. 14537-14545, Dec 31 2008.

QINGBAO, S.; XIAOLI, W.; YONGMIN, L.; YONGXIANG, M. Acylferrocene 2-furoyl hydrazones and their transition metal(II) complexes. **Polyhedron**, 13, n. 15, p. 2395-2399, 1994/08/01/ 1994.

RAMESH BABU, N.; SUBASHCHANDRABOSE, S.; SYED ALI PADUSHA, M.; SALEEM, H. *et al.* Synthesis and spectral characterization of hydrazone derivative of furfural using experimental and DFT methods. **Spectrochimica Acta Part A: Molecular and Biomolecular Spectroscopy**, 120, p. 314-322, 2014/02/24/ 2014.

RAVINDRAN, N. E. A.; YADAV, M.; TAMIZH, M. M.; BHUVANESH, N. *et al.* Solvent-Free Synthesis of Substituted Benzimidazoles and Quinazolinones via Acceptorless Dehydrogenative Coupling Using Ferrocene-Hydrazone-Based Ru(II)-p–cymene Catalysts. **Asian Journal of Organic Chemistry**, 12, n. 3, p. e202200675, 2023/03/01 2023.

RICE, H. C.; DE MALMAZET, D.; SCHREURS, A.; FRERE, S. *et al.* Secreted amyloid-β precursor protein functions as a GABA(B)R1a ligand to modulate synaptic transmission. **Science**, 363, n. 6423, Jan 11 2019.

RIGAKU, O. CrysAlisPRO, Rigaku Oxford Diffraction. Rigaku Corporation. **Tokyo, Japan**, 2015.

RIVAL, T.; PAGE, R. M.; CHANDRARATNA, D. S.; SENDALL, T. J. *et al.* Fenton chemistry and oxidative stress mediate the toxicity of the β-amyloid peptide in a Drosophila model of Alzheimer’s disease. **European Journal of Neuroscience**, 29, n. 7, p. 1335-1347, 2009/04/01 2009.

ROBERTS, B. R.; RYAN, T. M.; BUSH, A. I.; MASTERS, C. L. *et al.* The role of metallobiology and amyloid-β peptides in Alzheimer's disease. **Journal of Neurochemistry**, 120, n. s1, p. 149-166, 2012/01/01 2012.

SATHYADEVI, P.; KRISHNAMOORTHY, P.; BUTORAC, R. R.; COWLEY, A. H. *et al.* Synthesis of novel heterobimetallic copper(i) hydrazone Schiff base complexes: A comparative study on the effect of heterocyclic hydrazides towards interaction with DNA/protein, free radical scavenging and cytotoxicity†. **Metallomics**, 4, n. 5, p. 498-511, 2012.

SCOTT, L. E.; ORVIG, C. Medicinal inorganic chemistry approaches to passivation and removal of aberrant metal ions in disease. **Chem Rev**, 109, n. 10, p. 4885-4910, Oct 2009.

SELKOE, D. J. Amyloid beta-protein and the genetics of Alzheimer's disease. **J Biol Chem**, 271, n. 31, p. 18295-18298, Aug 2 1996.

SELKOE, D. J. Soluble oligomers of the amyloid beta-protein impair synaptic plasticity and behavior. **Behav Brain Res**, 192, n. 1, p. 106-113, Sep 1 2008.

SELVAM, P.; SATHIYAKUMAR, S.; SRINIVASAN, K.; PREMKUMAR, T. A Copper(II) complex of a new hydrazone: A solid-state single source precursor for the preparation of both Cu and CuO nanoparticles. **Journal of Molecular Structure**, 1177, p. 469-475, 2019/02/05/ 2019.

SENSI, S. L.; GRANZOTTO, A.; SIOTTO, M.; SQUITTI, R. Copper and Zinc Dysregulation in Alzheimer's Disease. **Trends in Pharmacological Sciences**, 39, n. 12, p. 1049-1063, 2018.

SENSI, S. L.; PAOLETTI, P.; BUSH, A. I.; SEKLER, I. Zinc in the physiology and pathology of the CNS. **Nature Reviews Neuroscience**, 10, n. 11, p. 780-791, 2009/11/01 2009.

SERRANO-POZO, A.; FROSCH, M. P.; MASLIAH, E.; HYMAN, B. T. Neuropathological alterations in Alzheimer disease. **Cold Spring Harb Perspect Med**, 1, n. 1, p. a006189, Sep 2011.

SHELDRICK, G. Crystal structure refinement with SHELXL. **Acta Crystallographica Section C**, 71, n. 1, p. 3-8, 2015.

SILVERSTEIN, R. M.; WEBSTER, F. X.; KIEMLE, D. J.; BRYCE, D. L. **Spectrometric Identification of Organic Compounds**. Wiley, 2014. 9780470616376.

SMITH, M. d. A. C. Doença de Alzheimer. **Revista Brasileira de Psiquiatria**, 21, n. suppl 2, p. 03-07, 1999.

SOCEA, L.-I.; BARBUCEANU, S.-F.; PAHONTU, E. M.; DUMITRU, A.-C. *et al.* Acylhydrazones and Their Biological Activity: A Review. **Molecules**, v.27, n. 24, DOI: 10.3390/molecules27248719.

SOREGHAN, B.; KOSMOSKI, J.; GLABE, C. Surfactant properties of Alzheimer's A beta peptides and the mechanism of amyloid aggregation. **J Biol Chem**, 269, n. 46, p. 28551-28554, Nov 18 1994.

SPIRES-JONES, T. L.; HYMAN, B. T. The intersection of amyloid beta and tau at synapses in Alzheimer's disease. **Neuron**, 82, n. 4, p. 756-771, May 21 2014.

SQUITTI, R.; SIMONELLI, I.; CASSETTA, E.; LUPOI, D. *et al.* Patients with Increased Non-Ceruloplasmin Copper Appear a Distinct Sub-Group of Alzheimer's Disease: A Neuroimaging Study. **Current Alzheimer research**, 14, n. 12, p. 1318-1326, 2017. Article.

STANCU, I. C.; VASCONCELOS, B.; TERWEL, D.; DEWACHTER, I. Models of β-amyloid induced Tau-pathology: the long and "folded" road to understand the mechanism. **Mol Neurodegener**, 9, p. 51, Nov 18 2014.

Standard Potential of the Silver-Silver Chloride Electrode. 50, n. 11-12, p. 1701-1706, 1978.

STEINER, T. The Hydrogen Bond in the Solid State. **Angewandte Chemie International Edition**, 41, n. 1, p. 48-76, 2002/01/04 2002.

SU, B.; WANG, X.; NUNOMURA, A.; MOREIRA, P. I. *et al.* Oxidative stress signaling in Alzheimer's disease. **Curr Alzheimer Res**, 5, n. 6, p. 525-532, Dec 2008.

SUN, X.-Y.; WEI, Y.-P.; XIONG, Y.; WANG, X.-C. *et al.* Synaptic Released Zinc Promotes Tau Hyperphosphorylation by Inhibition of Protein Phosphatase 2A (PP2A)*. **Journal of Biological Chemistry**, 287, n. 14, p. 11174-11182, 2012/03/30/ 2012.

SWERDLOW, R. H. The neurodegenerative mitochondriopathies. **Journal of Alzheimer's Disease**, 17, n. 4, p. 737-751, 2009. Review.

TAUBE, H. I - INTRODUCTION OF THE REAGENTS: Studies in Hydration of Cations. *In*: TAUBE, H. (Ed.). **Electron Transfer Reactions of Complex Ions in Solution**: Academic Press, 1970. p. 1-26.

THINAKARAN, G.; KOO, E. H. Amyloid precursor protein trafficking, processing, and function. **J Biol Chem**, 283, n. 44, p. 29615-29619, Oct 31 2008.

ŢÎNŢAŞ, M. L.; DIAC, A. P.; SORAN, A.; TEREC, A. *et al.* Structural characterization of new 2-aryl-5-phenyl-1,3,4-oxadiazin-6-ones and their N-aroylhydrazone precursors. **Journal of Molecular Structure**, 1058, p. 106-113, 2014/01/24/ 2014.

TOLUN, A.; ALTINTAS, Z. Chapter 16 - Chemical sensing of food phenolics and antioxidant capacity. *In*: BARHOUM, A. e ALTINTAS, Z. (Ed.). **Advanced Sensor Technology**: Elsevier, 2023. p. 593-646.

TOP, S.; TANG, J.; VESSIÈRES, A.; CARREZ, D. *et al.* Ferrocenyl hydroxytamoxifen: a prototype for a new range of oestradiol receptor site-directed cytotoxics. **Chemical Communications**, n. 8, p. 955-956, 1996. 10.1039/CC9960000955.

TORRIERO, A. A. J.; MRUTHUNJAYA, A. K. V. Ferrocene-Based Electrochemical Sensors for Cations. **Inorganics**, v.11, n. 12, DOI: 10.3390/inorganics11120472.

TRACHIOTI, M. G.; LAZANAS, A. C.; PRODROMIDIS, M. I. Shedding light on the calculation of electrode electroactive area and heterogeneous electron transfer rate constants at graphite screen-printed electrodes. **Mikrochim Acta**, 190, n. 7, p. 251, Jun 7 2023.

TSIERKEZOS, N. G. Cyclic Voltammetric Studies of Ferrocene in Nonaqueous Solvents in the Temperature Range from 248.15 to 298.15 K. **Journal of Solution Chemistry**, 36, n. 3, p. 289-302, 2007/03/01 2007.

UAUY, R.; OLIVARES, M.; GONZALEZ, M. Essentiality of copper in humans. **The American Journal of Clinical Nutrition**, 67, n. 5, p. 952S-959S, 1998/05/01/ 1998.

VAN DE WATERBEEMD, H.; CAMENISCH, G.; FOLKERS, G.; CHRETIEN, J. R. *et al.* Estimation of blood-brain barrier crossing of drugs using

molecular size and shape, and H-bonding descriptors. **J Drug Target**, 6, n. 2, p. 151-165, 1998.

VĚŽNÍK, J.; KONHEFR, M.; FOHLEROVÁ, Z.; LACINA, K. Redox-dependent cytotoxicity of ferrocene derivatives and ROS-activated prodrugs based on ferrocenyliminoboronates. **Journal of Inorganic Biochemistry**, 224, p. 111561, 2021/11/01/ 2021.

VITEK, G. E.; DECOURT, B.; SABBAGH, M. N. Lecanemab (BAN2401): an anti-beta-amyloid monoclonal antibody for the treatment of Alzheimer disease. **Expert Opin Investig Drugs**, 32, n. 2, p. 89-94, Feb 2023.

WALSH, D. M.; KLYUBIN, I.; FADEEVA, J. V.; CULLEN, W. K. *et al.* Naturally secreted oligomers of amyloid beta protein potently inhibit hippocampal long-term potentiation in vivo. **Nature**, 416, n. 6880, p. 535-539, Apr 4 2002.

WEINER, M. W.; VEITCH, D. P.; AISEN, P. S.; BECKETT, L. A. *et al.* Impact of the Alzheimer's Disease Neuroimaging Initiative, 2004 to 2014. **Alzheimers Dement**, 11, n. 7, p. 865-884, Jul 2015.

WHITFIELD, D. R.; VALLORTIGARA, J.; ALGHAMDI, A.; HOWLETT, D. *et al.* Assessment of ZnT3 and PSD95 protein levels in Lewy body dementias and Alzheimer's disease: association with cognitive impairment. **Neurobiology of Aging**, 35, n. 12, p. 2836-2844, 2014/12/01/ 2014.

WILCOCK, G. K.; ESIRI, M. M.; BOWEN, D. M.; SMITH, C. C. Alzheimer's disease. Correlation of cortical choline acetyltransferase activity with the severity of dementia and histological abnormalities. **J Neurol Sci**, 57, n. 2-3, p. 407-417, Dec 1982.

WILKINSON, G.; ROSENBLUM, M.; WHITING, M. C.; WOODWARD, R. B. THE STRUCTURE OF IRON BIS-CYCLOPENTADIENYL. **Journal of the American Chemical Society**, 74, n. 8, p. 2125-2126, 1952/04/01 1952.

WOODWARD, R. B.; ROSENBLUM, M.; WHITING, M. C. A NEW AROMATIC SYSTEM. **Journal of the American Chemical Society**, 74, n. 13, p. 3458-3459, 1952/07/01 1952.

WU, J. W.; HUSSAINI, S. A.; BASTILLE, I. M.; RODRIGUEZ, G. A. *et al.* Neuronal activity enhances tau propagation and tau pathology in vivo. **Nat Neurosci**, 19, n. 8, p. 1085-1092, Aug 2016.

YAMADA, K.; HOLTH, J. K.; LIAO, F.; STEWART, F. R. *et al.* Neuronal activity regulates extracellular tau in vivo. **J Exp Med**, 211, n. 3, p. 387-393, Mar 10 2014.

YEARY, R. A. Chronic toxicity of dicyclopentadienyliron (ferrocene) in dogs. **Toxicol Appl Pharmacol**, 15, n. 3, p. 666-676, Nov 1969.

YIANNOPOULOU, K. G.; PAPAGEORGIOU, S. G. Current and Future Treatments in Alzheimer Disease: An Update. **Journal of Central Nervous System Disease**, 12, p. 1179573520907397, 2020.

YUNYIN, N.; PEIKUN, C.; HONGYUN, Z.; QINGAN, W. *et al.* Ferrocenylaldehyde Nicotikoyl and Isonicotikoyl Hydrazones and Their Coordination Compounds with Transition metals (II). **Synthesis and Reactivity in Inorganic and Metal-Organic Chemistry**, 28, n. 4, p. 637-647, 1998/04/01 1998.

10. Appendix – Crystallographic Tables

Table A1. Crystal data, data collection and structure refinement details for **Feizone**.

$2(C_{17}H_{15}FeN_3O)$	$Z = 2$
$M_r = 333.17$	$F(000) = 344$
Orthorhombic, $P2_12_12_1$	$D_x = 0.744$ Mg m^{-3}
$a = 6.6863$ (1) Å	Cu $K\alpha$ radiation, $\lambda = 1.54184$ Å
$b = 10.6806$ (1) Å	$\mu = 4.08$ mm^{-1}
$c = 20.8280$ (2) Å	$T = 299$ K
$V = 1487.40$ (3) Å^3	0.24 × 0.18 × 0.05 mm
31427 measured reflections	$\theta_{max} = 79.5°$, $\theta_{min} = 4.3°$
3211 independent reflections	$h = -8 \rightarrow 8$
3040 reflections with $I > 2\sigma(I)$	$k = -13 \rightarrow 13$
$R_{int} = 0.040$	$l = -26 \rightarrow 26$
Refinement on F2	*Primary atom site location: dual*
Least-squares matrix: full	*Hydrogen site location: mixed*
R[F2 > 2s(F2)] = 0.026	*H atoms treated by a mixture of independent and constrained refinement*
wR(F2) = 0.070	*w = 1/[s2(Fo2) + (0.0366P)2 + 0.2826P]* *where P = (Fo2 + 2Fc2)/3*
S = 1.06	*(D/s)max = 0.001*
3211 reflections	*Dρmax = 0.18 e Å-3*
203 parameters	*Dρmin = -0.36 e Å-3*
0 restraints	*Absolute structure: Flack x determined using 1197 quotients [(I+)-(I-)]/[(I+)+(I-)] (Parsons, Flack and Wagner, Acta Cryst. B69 (2013) 249-259).*
	Absolute structure parameter: -0.0088 (19)

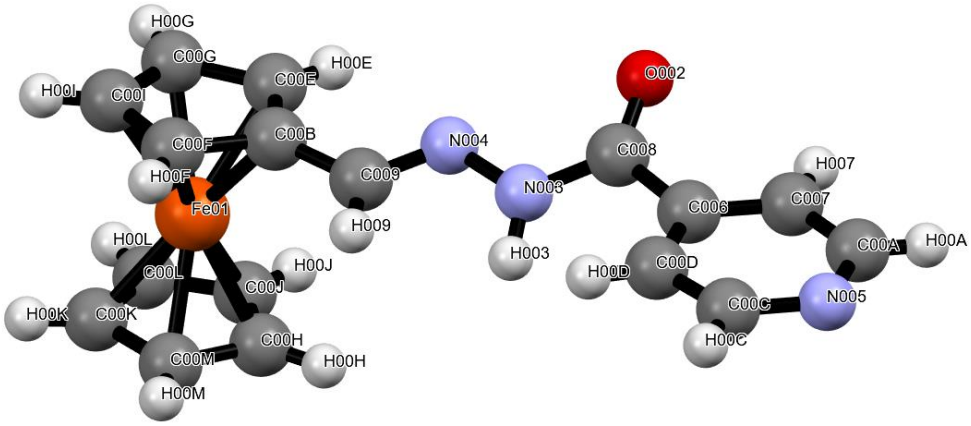

Figure A1. Feizone structure representation with atoms labelled as in crystallographic geometric parameters in Table A2.

Table A2. Geometric parameters for **Feizone** (continues).

Bond distances (Å)			
Fe01—C00B	2.040 (2)	C00A—H00A	0.9300
Fe01—C00E	2.046 (3)	C00B—C00E	1.419 (4)
Fe01—C00F	2.030 (3)	C00B—C00F	1.427 (4)
Fe01—C00G	2.042 (3)	C00C—H00C	0.9300
Fe01—C00H	2.025 (4)	C00C—C00D	1.380 (4)
Fe01—C00I	2.039 (3)	C00D—H00D	0.9300
Fe01—C00J	2.036 (4)	C00E—H00E	0.9300
Fe01—C00K	2.012 (4)	C00E—C00G	1.426 (4)
Fe01—C00L	2.031 (4)	C00F—H00F	0.9300
Fe01—C00M	2.019 (5)	C00F—C00I	1.418 (5)
O002—C008	1.226 (3)	C00G—H00G	0.9300
N003—N004	1.390 (3)	C00G—C00I	1.388 (6)
N003—C008	1.347 (3)	C00H—H00H	0.9300
N003—H003	0.91 (3)	C00H—C00J	1.317 (8)
N004—C009	1.274 (3)	C00H—C00M	1.393 (8)
N005—C00A	1.333 (3)	C00I—H00I	0.9300
N005—C00C	1.332 (3)	C00J—H00J	0.9300
C006—C007	1.385 (3)	C00J—C00L	1.359 (8)

Table A3. Geometric parameters for **Feizone** (continuation).

C006—C008	1.505 (3)	C00K—H00K	0.9300
C006—C00D	1.390 (3)	C00K—C00L	1.372 (10)
C007—H007	0.9300	C00K—C00M	1.414 (9)
C007—C00A	1.385 (3)	C00L—H00L	0.9300
C009—H009	0.9300	C00M—H00M	0.9300
C009—C00B	1.453 (3)		
Bond angles (º)			
C00B—Fe01—C00E	40.63 (12)	C00E—C00B—Fe01	69.90 (14)
C00B—Fe01—C00G	68.32 (11)	C00E—C00B—C009	127.7 (2)
C00F—Fe01—C00B	41.04 (10)	C00E—C00B—C00F	107.6 (2)
C00F—Fe01—C00E	68.60 (13)	C00F—C00B—Fe01	69.09 (14)
C00F—Fe01—C00G	67.99 (16)	C00F—C00B—C009	124.6 (3)
C00F—Fe01—C00I	40.78 (14)	N005—C00C—H00C	118.0
C00F—Fe01—C00J	165.2 (2)	N005—C00C—C00D	124.1 (2)
C00F—Fe01—C00L	154.3 (2)	C00D—C00C—H00C	118.0
C00G—Fe01—C00E	40.84 (12)	C006—C00D—H00D	120.7
C00H—Fe01—C00B	110.37 (14)	C00C—C00D—C006	118.5 (2)
C00H—Fe01—C00E	119.91 (18)	C00C—C00D—H00D	120.7
C00H—Fe01—C00F	130.1 (2)	Fe01—C00E—H00E	126.3
C00H—Fe01—C00G	152.6 (2)	C00B—C00E—Fe01	69.47 (15)
C00H—Fe01—C00I	167.3 (3)	C00B—C00E—H00E	126.3
C00H—Fe01—C00J	37.8 (2)	C00B—C00E—C00G	107.4 (3)
C00H—Fe01—C00L	64.8 (2)	C00G—C00E—Fe01	69.44 (18)
C00I—Fe01—C00B	68.55 (10)	C00G—C00E—H00E	126.3
C00I—Fe01—C00E	68.15 (14)	Fe01—C00F—H00F	125.6
C00I—Fe01—C00G	39.78 (16)	C00B—C00F—Fe01	69.87 (15)
C00J—Fe01—C00B	127.30 (18)	C00B—C00F—H00F	126.1
C00J—Fe01—C00E	108.2 (2)	C00I—C00F—Fe01	69.95 (17)
C00J—Fe01—C00G	119.7 (2)	C00I—C00F—C00B	107.7 (3)
C00J—Fe01—C00I	152.9 (2)	C00I—C00F—H00F	126.1
C00K—Fe01—C00B	155.5 (3)	Fe01—C00G—H00G	126.3
C00K—Fe01—C00E	162.8 (3)	C00E—C00G—Fe01	69.72 (16)
C00K—Fe01—C00F	120.6 (3)	C00E—C00G—H00G	125.6
C00K—Fe01—C00G	125.8 (2)	C00I—C00G—Fe01	69.98 (19)
C00K—Fe01—C00H	66.99 (19)	C00I—C00G—C00E	108.8 (3)

Table A4. Geometric parameters for **Feizone** (continuation).

C00K—Fe01—C00I	108.37 (16)	C00I—C00G—H00G	125.6
C00K—Fe01—C00J	66.7 (2)	Fe01—C00H—H00H	125.7
C00K—Fe01—C00L	39.7 (3)	C00J—C00H—Fe01	71.5 (3)
C00K—Fe01—C00M	41.1 (3)	C00J—C00H—H00H	124.8
C00L—Fe01—C00B	163.3 (3)	C00J—C00H—C00M	110.5 (5)
C00L—Fe01—C00E	126.2 (3)	C00M—C00H—Fe01	69.6 (3)
C00L—Fe01—C00G	108.2 (2)	C00M—C00H—H00H	124.8
C00L—Fe01—C00I	119.92 (18)	Fe01—C00I—H00I	126.3
C00L—Fe01—C00J	39.1 (2)	C00F—C00I—Fe01	69.27 (16)
C00M—Fe01—C00B	120.6 (2)	C00F—C00I—H00I	125.8
C00M—Fe01—C00E	154.0 (2)	C00G—C00I—Fe01	70.24 (18)
C00M—Fe01—C00F	109.5 (2)	C00G—C00I—C00F	108.5 (3)
C00M—Fe01—C00G	164.5 (3)	C00G—C00I—H00I	125.8
C00M—Fe01—C00H	40.3 (2)	Fe01—C00J—H00J	124.9
C00M—Fe01—C00I	128.4 (3)	C00H—C00J—Fe01	70.6 (3)
C00M—Fe01—C00J	66.6 (3)	C00H—C00J—H00J	125.7
C00M—Fe01—C00L	67.0 (3)	C00H—C00J—C00L	108.5 (6)
N004—N003—H003	115.3 (19)	C00L—C00J—Fe01	70.3 (3)
C008—N003—N004	120.23 (18)	C00L—C00J—H00J	125.7
C008—N003—H003	121.9 (19)	Fe01—C00K—H00K	124.4
C009—N004—N003	114.0 (2)	C00L—C00K—Fe01	70.9 (3)
C00C—N005—C00A	117.1 (2)	C00L—C00K—H00K	126.6
C007—C006—C008	119.26 (19)	C00L—C00K—C00M	106.8 (5)
C007—C006—C00D	117.8 (2)	C00M—C00K—Fe01	69.7 (2)
C00D—C006—C008	122.8 (2)	C00M—C00K—H00K	126.6
C006—C007—H007	120.3	Fe01—C00L—H00L	126.1
C006—C007—C00A	119.4 (2)	C00J—C00L—Fe01	70.6 (2)
C00A—C007—H007	120.3	C00J—C00L—C00K	109.1 (6)
O002—C008—N003	124.8 (2)	C00J—C00L—H00L	125.4
O002—C008—C006	120.98 (19)	C00K—C00L—Fe01	69.4 (3)
N003—C008—C006	114.20 (18)	C00K—C00L—H00L	125.4
N004—C009—H009	119.6	Fe01—C00M—H00M	124.9
N004—C009—C00B	120.8 (2)	C00H—C00M—Fe01	70.1 (3)
C00B—C009—H009	119.6	C00H—C00M—C00K	105.1 (6)
N005—C00A—C007	123.1 (2)	C00H—C00M—H00M	127.5

Table A5. Geometric parameters for **Feizone** (continuation).

N005—C00A—H00A	118.5	C00K—C00M—Fe01	69.2 (3)
C007—C00A—H00A	118.5	C00K—C00M—H00M	127.5
C009—C00B—Fe01	125.39 (16)		
Dihedral angles (º)			
Fe01—C00B—C00E—C00G	59.34 (18)	C009—C00B—C00F—C00I	-179.3 (2)
Fe01—C00B—C00F—C00I	-59.96 (19)	C00A—N005—C00C—C00D	-0.1 (4)
Fe01—C00E—C00G—C00I	59.3 (2)	C00B—C00E—C00G—Fe01	-59.36 (18)
Fe01—C00F—C00I—C00G	-59.5 (2)	C00B—C00E—C00G—C00I	-0.1 (3)
Fe01—C00G—C00I—C00F	58.9 (2)	C00B—C00F—C00I—Fe01	59.91 (18)
Fe01—C00H—C00J—C00L	-60.3 (3)	C00B—C00F—C00I—C00G	0.4 (3)
Fe01—C00H—C00M—C00K	60.8 (3)	C00C—N005—C00A—C007	1.3 (4)
Fe01—C00J—C00L—C00K	-58.9 (3)	C00D—C006—C007—C00A	-1.3 (3)
Fe01—C00K—C00L—C00J	59.7 (3)	C00D—C006—C008—O002	151.1 (2)
Fe01—C00K—C00M—C00H	-61.3 (3)	C00D—C006—C008—N003	-26.2 (3)
N003—N004—C009—C00B	-178.99 (19)	C00E—C00B—C00F—Fe01	59.49 (17)
N004—N003—C008—O002	0.0 (3)	C00E—C00B—C00F—C00I	-0.5 (3)
N004—N003—C008—C006	177.26 (17)	C00E—C00G—C00I—Fe01	-59.1 (2)
N004—C009—C00B—Fe01	111.8 (3)	C00E—C00G—C00I—C00F	-0.2 (3)
N004—C009—C00B—C00E	20.8 (4)	C00F—C00B—C00E—Fe01	-58.98 (18)
N004—C009—C00B—C00F	-160.6 (2)	C00F—C00B—C00E—C00G	0.4 (3)
N005—C00C—C00D—C006	-1.8 (4)	C00H—C00J—C00L—Fe01	60.6 (3)

Table A6. Geometric parameters for **Feizone** (conclusion).

C006—C007—C00A—N005	-0.6 (4)	C00H—C00J—C00L—C00K	1.6 (5)
C007—C006—C008—O002	-25.3 (3)	C00J—C00H—C00M—Fe01	-60.0 (3)
C007—C006—C008—N003	157.4 (2)	C00J—C00H—C00M—C00K	0.7 (5)
C007—C006—C00D—C00C	2.4 (4)	C00L—C00K—C00M—Fe01	61.6 (3)
C008—N003—N004—C009	-169.6 (2)	C00L—C00K—C00M—C00H	0.3 (5)
C008—C006—C007—C00A	175.3 (2)	C00M—C00H—C00J—Fe01	58.9 (3)
C008—C006—C00D—C00C	-174.1 (2)	C00M—C00H—C00J—C00L	-1.5 (5)
C009—C00B—C00E—Fe01	119.8 (2)	C00M—C00K—C00L—Fe01	-60.8 (3)
C009—C00B—C00E—C00G	179.1 (2)	C00M—C00K—C00L—C00J	-1.1 (5)
C009—C00B—C00F—Fe01	-119.3 (2)		

Table A7. Crystal data, data collection and structure refinement details for **Ferfurone**.

$2(C_{16}H_{14}FeN_2O_2)\cdot 2(CH_4O)$	$Z = 4$
$M_r = 708.37$	$F(000) = 1472$
Orthorhombic, $Pna2_1$	$D_x = 1.413$ Mg m^{-3}
$a = 13.4446$ (1) Å	Cu Ka radiation, l = 1.54184 Å
$b = 6.3240$ (1) Å	m = 7.40 mm^{-1}
$c = 39.1635$ (4) Å	$T = 299$ K
$V = 3329.82$ (7) Å^3	0.34 × 0.16 × 0.09 mm
66138 measured reflections	$q_{max} = 79.5°$, $q_{min} = 2.3°$
6913 independent reflections	$h = -17 \rightarrow 17$
5828 reflections with $I > 2s(I)$	$k = -8 \rightarrow 7$
$R_{int} = 0.060$	$l = -47 \rightarrow 49$
Refinement on F^2	Primary atom site location: dual
Least-squares matrix: full	Hydrogen site location: mixed
$R[F^2 > 2s(F^2)] = 0.083$	H atoms treated by a mixture of independent and constrained refinement
$wR(F^2) = 0.222$	$w = 1/[s^2(F_o^2) + (0.1806P)^2 + 0.4663P]$ where $P = (F_o^2 + 2F_c^2)/3$
$S = 1.03$	$(D/s)_{max} < 0.001$
6913 reflections	$D\rho_{max} = 3.55$ e Å^{-3}
423 parameters	$D\rho_{min} = -0.53$ e Å^{-3}
2 restraints	Absolute structure: Flack x determined using 2334 quotients [(I+)-(I-)]/[(I+)+(I-)] (Parsons, Flack and Wagner, Acta Cryst. B69 (2013) 249-259).
	Absolute structure parameter: 0.260 (5)

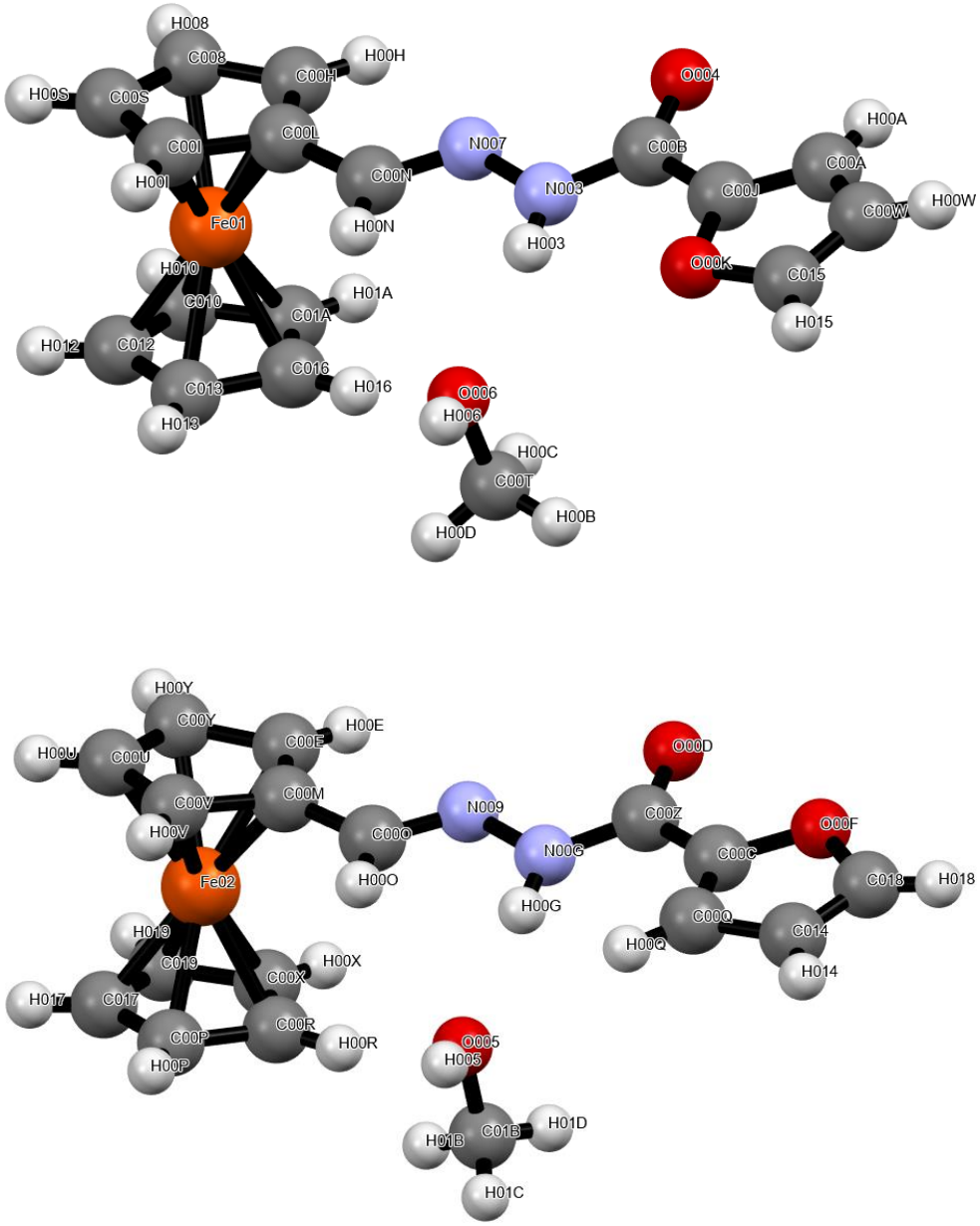

Figure A2. Representation in two different perspectives of both crystallographic distinct unit structures of **Ferfurone** with atoms labelled as in crystallographic geometric parameters in Table A4.

Table A8. Geometric parameters for **Ferfurone** (continues).

Bond distances (Å)			
Fe01—C008	2.033 (8)	C00I—H00I	0.9800
Fe01—C00H	2.061 (8)	C00I—C00L	1.418 (12)

Table A9. Geometric parameters for **Ferfurone** (continuation).

Fe01—C00I	2.027 (7)	C00I—C00S	1.414 (13)
Fe01—C00L	2.027 (7)	C00J—O00K	1.360 (12)
Fe01—C00S	2.052 (9)	O00K—C015	1.407 (18)
Fe01—C010	2.038 (9)	C00L—C00N	1.460 (10)
Fe01—C012	2.025 (10)	C00M—C00O	1.441 (10)
Fe01—C013	2.047 (10)	C00M—C00V	1.437 (11)
Fe01—C016	2.021 (9)	C00N—H00N	0.9300
Fe01—C01A	2.035 (9)	C00O—H00O	0.9300
Fe02—C00E	2.057 (8)	C00P—H00P	0.9300
Fe02—C00M	2.033 (8)	C00P—C00R	1.42 (2)
Fe02—C00P	2.025 (9)	C00P—C017	1.393 (19)
Fe02—C00R	2.033 (10)	C00Q—H00Q	0.9300
Fe02—C00U	2.045 (8)	C00Q—C014	1.439 (14)
Fe02—C00V	2.032 (7)	C00R—H00R	0.9300
Fe02—C00X	2.047 (10)	C00R—C00X	1.40 (2)
Fe02—C00Y	2.065 (8)	C00S—H00S	0.9800
Fe02—C017	2.025 (9)	C00T—H00B	0.9600
Fe02—C019	2.028 (9)	C00T—H00C	0.9600
N003—H003	0.8600	C00T—H00D	0.9600
N003—N007	1.389 (9)	C00U—H00U	0.9300
N003—C00B	1.335 (10)	C00U—C00V	1.410 (13)
O004—C00B	1.227 (8)	C00U—C00Y	1.403 (15)
O005—H005	0.8200	C00V—H00V	0.9300
O005—C01B	1.372 (16)	C00W—H00W	0.9300
O006—H006	0.8200	C00W—C015	1.27 (2)
O006—C00T	1.408 (19)	C00X—H00X	0.9300
N007—C00N	1.267 (10)	C00X—C019	1.36 (2)
C008—H008	0.9300	C00Y—H00Y	0.9300
C008—C00H	1.399 (13)	C010—H010	0.9300
C008—C00S	1.411 (14)	C010—C012	1.37 (2)
N009—N00G	1.391 (9)	C010—C01A	1.36 (2)
N009—C00O	1.270 (10)	C012—H012	0.9300
C00A—H00A	0.9300	C012—C013	1.41 (2)
C00A—C00J	1.322 (12)	C013—H013	0.9300
C00A—C00W	1.381 (18)	C013—C016	1.36 (2)

Table A10. Geometric parameters for **Ferfurone** (continuation).

C00B—C00J	1.470 (11)	C014—H014	0.9300
C00C—O00F	1.347 (10)	C014—C018	1.29 (2)
C00C—C00Q	1.312 (13)	C015—H015	0.9300
C00C—C00Z	1.436 (12)	C016—H016	0.9300
O00D—C00Z	1.236 (9)	C016—C01A	1.40 (2)
C00E—H00E	0.9300	C017—H017	0.9300
C00E—C00M	1.442 (11)	C017—C019	1.34 (2)
C00E—C00Y	1.434 (13)	C018—H018	0.9300
O00F—C018	1.422 (18)	C019—H019	0.9300
N00G—C00Z	1.345 (10)	C01A—H01A	0.9300
N00G—H00G	0.92 (3)	C01B—H01B	0.9600
C00H—H00H	0.9800	C01B—H01C	0.9600
C00H—C00L	1.453 (10)	C01B—H01D	0.9600
Bond Angles (º)			
C008—Fe01—C00H	39.9 (4)	C00A—C00J—O00K	111.0 (8)
C008—Fe01—C00S	40.4 (4)	O00K—C00J—C00B	125.1 (7)
C008—Fe01—C010	109.2 (5)	C00J—O00K—C015	104.0 (11)
C008—Fe01—C013	163.8 (7)	C00H—C00L—Fe01	70.4 (4)
C008—Fe01—C01A	121.2 (5)	C00H—C00L—C00N	126.6 (7)
C00I—Fe01—C008	68.3 (4)	C00I—C00L—Fe01	69.5 (4)
C00I—Fe01—C00H	69.7 (4)	C00I—C00L—C00H	108.9 (7)
C00I—Fe01—C00L	40.9 (3)	C00I—C00L—C00N	124.5 (7)
C00I—Fe01—C00S	40.6 (4)	C00N—C00L—Fe01	123.7 (5)
C00I—Fe01—C010	156.4 (7)	C00E—C00M—Fe02	70.2 (5)
C00I—Fe01—C013	108.3 (4)	C00O—C00M—Fe02	124.6 (5)
C00I—Fe01—C01A	162.7 (6)	C00O—C00M—C00E	128.9 (8)
C00L—Fe01—C008	67.9 (3)	C00V—C00M—Fe02	69.3 (4)
C00L—Fe01—C00H	41.6 (3)	C00V—C00M—C00E	107.2 (7)
C00L—Fe01—C00S	68.0 (3)	C00V—C00M—C00O	123.9 (7)
C00L—Fe01—C010	161.8 (7)	N007—C00N—C00L	121.2 (6)
C00L—Fe01—C013	120.7 (5)	N007—C00N—H00N	119.4
C00L—Fe01—C01A	125.9 (6)	C00L—C00N—H00N	119.4
C00S—Fe01—C00H	68.4 (4)	N009—C00O—C00M	121.1 (7)
C010—Fe01—C00H	124.6 (6)	N009—C00O—H00O	119.5
C010—Fe01—C00S	122.3 (5)	C00M—C00O—H00O	119.5

Table A11. Geometric parameters for **Ferfurone** (continuation).

C010—Fe01—C013	67.1 (5)	Fe02—C00P—H00P	124.7
C012—Fe01—C008	126.6 (5)	C00R—C00P—Fe02	69.8 (6)
C012—Fe01—C00H	161.2 (6)	C00R—C00P—H00P	127.3
C012—Fe01—C00I	122.0 (6)	C017—C00P—Fe02	69.9 (6)
C012—Fe01—C00L	156.6 (6)	C017—C00P—H00P	127.3
C012—Fe01—C00S	109.8 (5)	C017—C00P—C00R	105.4 (11)
C012—Fe01—C010	39.3 (7)	C00C—C00Q—H00Q	127.9
C012—Fe01—C013	40.6 (7)	C00C—C00Q—C014	104.2 (9)
C012—Fe01—C01A	65.9 (6)	C014—C00Q—H00Q	127.9
C013—Fe01—C00H	155.3 (6)	Fe02—C00R—H00R	125.6
C013—Fe01—C00S	126.9 (6)	C00P—C00R—Fe02	69.1 (6)
C016—Fe01—C008	155.7 (6)	C00P—C00R—H00R	126.5
C016—Fe01—C00H	120.9 (5)	C00X—C00R—Fe02	70.4 (6)
C016—Fe01—C00I	125.4 (5)	C00X—C00R—C00P	107.1 (12)
C016—Fe01—C00L	108.1 (4)	C00X—C00R—H00R	126.5
C016—Fe01—C00S	162.5 (6)	Fe01—C00S—H00S	126.2
C016—Fe01—C010	66.6 (5)	C008—C00S—Fe01	69.1 (5)
C016—Fe01—C012	66.5 (5)	C008—C00S—C00I	107.7 (8)
C016—Fe01—C013	39.1 (6)	C008—C00S—H00S	126.2
C016—Fe01—C01A	40.2 (7)	C00I—C00S—Fe01	68.8 (5)
C01A—Fe01—C00H	107.6 (5)	C00I—C00S—H00S	126.2
C01A—Fe01—C00S	155.7 (6)	O006—C00T—H00B	109.5
C01A—Fe01—C010	38.9 (7)	O006—C00T—H00C	109.5
C01A—Fe01—C013	66.6 (6)	O006—C00T—H00D	109.5
C00E—Fe02—C00Y	40.7 (4)	H00B—C00T—H00C	109.5
C00M—Fe02—C00E	41.3 (3)	H00B—C00T—H00D	109.5
C00M—Fe02—C00R	106.8 (4)	H00C—C00T—H00D	109.5
C00M—Fe02—C00U	68.7 (3)	Fe02—C00U—H00U	126.2
C00M—Fe02—C00X	124.9 (6)	C00V—C00U—Fe02	69.3 (4)
C00M—Fe02—C00Y	68.9 (3)	C00V—C00U—H00U	125.3
C00P—Fe02—C00E	156.4 (5)	C00Y—C00U—Fe02	70.8 (5)
C00P—Fe02—C00M	120.4 (4)	C00Y—C00U—H00U	125.3
C00P—Fe02—C00R	41.1 (6)	C00Y—C00U—C00V	109.3 (8)
C00P—Fe02—C00U	125.0 (5)	Fe02—C00V—H00V	125.9
C00P—Fe02—C00V	107.2 (4)	C00M—C00V—Fe02	69.4 (4)

Table A12. Geometric parameters for **Ferfurone** (continuation).

C00P—Fe02—C00X	67.9 (5)	C00M—C00V—H00V	126.0
C00P—Fe02—C00Y	161.3 (6)	C00U—C00V—Fe02	70.3 (5)
C00P—Fe02—C017	40.2 (6)	C00U—C00V—C00M	108.0 (8)
C00P—Fe02—C019	67.2 (5)	C00U—C00V—H00V	126.0
C00R—Fe02—C00E	120.7 (5)	C00A—C00W—H00W	124.9
C00R—Fe02—C00U	162.1 (6)	C015—C00W—C00A	110.2 (12)
C00R—Fe02—C00X	40.2 (7)	C015—C00W—H00W	124.9
C00R—Fe02—C00Y	156.3 (6)	Fe02—C00X—H00X	126.5
C00U—Fe02—C00E	68.1 (4)	C00R—C00X—Fe02	69.4 (6)
C00U—Fe02—C00X	156.4 (6)	C00R—C00X—H00X	125.9
C00U—Fe02—C00Y	39.9 (4)	C019—C00X—Fe02	69.7 (7)
C00V—Fe02—C00E	69.0 (4)	C019—C00X—C00R	108.1 (13)
C00V—Fe02—C00M	41.4 (3)	C019—C00X—H00X	125.9
C00V—Fe02—C00R	124.9 (5)	Fe02—C00Y—H00Y	127.0
C00V—Fe02—C00U	40.5 (4)	C00E—C00Y—Fe02	69.3 (5)
C00V—Fe02—C00X	162.1 (6)	C00E—C00Y—H00Y	125.9
C00V—Fe02—C00Y	68.1 (4)	C00U—C00Y—Fe02	69.3 (5)
C00X—Fe02—C00E	108.2 (5)	C00U—C00Y—C00E	108.2 (7)
C00X—Fe02—C00Y	122.1 (5)	C00U—C00Y—H00Y	125.9
C017—Fe02—C00E	161.2 (5)	O00D—C00Z—C00C	121.9 (8)
C017—Fe02—C00M	157.0 (5)	O00D—C00Z—N00G	122.3 (8)
C017—Fe02—C00R	67.1 (5)	N00G—C00Z—C00C	115.8 (6)
C017—Fe02—C00U	109.9 (5)	Fe01—C010—H010	125.5
C017—Fe02—C00V	122.5 (5)	C012—C010—Fe01	69.8 (6)
C017—Fe02—C00X	65.6 (6)	C012—C010—H010	125.9
C017—Fe02—C00Y	125.8 (5)	C01A—C010—Fe01	70.4 (6)
C017—Fe02—C019	38.7 (7)	C01A—C010—H010	125.9
C019—Fe02—C00E	125.4 (5)	C01A—C010—C012	108.2 (12)
C019—Fe02—C00M	161.3 (6)	Fe01—C012—H012	124.5
C019—Fe02—C00R	66.8 (5)	C010—C012—Fe01	70.8 (6)
C019—Fe02—C00U	122.7 (5)	C010—C012—H012	125.7
C019—Fe02—C00V	156.7 (6)	C010—C012—C013	108.5 (13)
C019—Fe02—C00X	39.0 (7)	C013—C012—Fe01	70.5 (6)
C019—Fe02—C00Y	109.5 (5)	C013—C012—H012	125.7
N007—N003—H003	120.9	Fe01—C013—H013	126.4

Table A13. Geometric parameters for **Ferfurone** (continuation).

C00B—N003—H003	120.8	C012—C013—Fe01	68.9 (6)
C00B—N003—N007	118.3 (6)	C012—C013—H013	126.9
C01B—O005—H005	109.5	C016—C013—Fe01	69.4 (6)
C00T—O006—H006	109.5	C016—C013—C012	106.2 (11)
C00N—N007—N003	115.4 (5)	C016—C013—H013	126.9
Fe01—C008—H008	125.3	C00Q—C014—H014	125.4
C00H—C008—Fe01	71.1 (5)	C018—C014—C00Q	109.1 (11)
C00H—C008—H008	124.6	C018—C014—H014	125.4
C00H—C008—C00S	110.7 (7)	O00K—C015—H015	125.6
C00S—C008—Fe01	70.5 (5)	C00W—C015—O00K	108.9 (12)
C00S—C008—H008	124.6	C00W—C015—H015	125.6
C00O—N009—N00G	115.2 (6)	Fe01—C016—H016	124.1
C00J—C00A—H00A	127.2	C013—C016—Fe01	71.5 (7)
C00J—C00A—C00W	105.6 (11)	C013—C016—H016	125.6
C00W—C00A—H00A	127.2	C013—C016—C01A	108.8 (12)
N003—C00B—C00J	116.2 (6)	C01A—C016—Fe01	70.4 (6)
O004—C00B—N003	124.6 (8)	C01A—C016—H016	125.6
O004—C00B—C00J	119.2 (8)	Fe02—C017—H017	126.0
O00F—C00C—C00Z	120.0 (8)	C00P—C017—Fe02	69.9 (6)
C00Q—C00C—O00F	113.5 (8)	C00P—C017—H017	125.0
C00Q—C00C—C00Z	126.5 (7)	C019—C017—Fe02	70.8 (6)
Fe02—C00E—H00E	126.8	C019—C017—C00P	110.1 (12)
C00M—C00E—Fe02	68.5 (4)	C019—C017—H017	125.0
C00M—C00E—H00E	126.3	O00F—C018—H018	125.5
C00Y—C00E—Fe02	70.0 (5)	C014—C018—O00F	108.9 (12)
C00Y—C00E—H00E	126.3	C014—C018—H018	125.5
C00Y—C00E—C00M	107.4 (8)	Fe02—C019—H019	124.5
C00C—O00F—C018	104.1 (10)	C00X—C019—Fe02	71.2 (6)
N009—N00G—H00G	116 (6)	C00X—C019—H019	125.4
C00Z—N00G—N009	119.2 (6)	C017—C019—Fe02	70.5 (6)
C00Z—N00G—H00G	125 (6)	C017—C019—C00X	109.3 (12)
Fe01—C00H—H00H	127.4	C017—C019—H019	125.4
C008—C00H—Fe01	68.9 (5)	Fe01—C01A—H01A	125.7
C008—C00H—H00H	127.4	C010—C01A—Fe01	70.7 (6)
C008—C00H—C00L	105.3 (7)	C010—C01A—C016	108.1 (12)

Table A14. Geometric parameters for **Ferfurone** (continuation).

C00L—C00H—Fe01	67.9 (4)	C010—C01A—H01A	125.9
C00L—C00H—H00H	127.4	C016—C01A—Fe01	69.3 (6)
Fe01—C00I—H00I	126.3	C016—C01A—H01A	125.9
C00L—C00I—Fe01	69.5 (4)	O005—C01B—H01B	109.5
C00L—C00I—H00I	126.3	O005—C01B—H01C	109.5
C00S—C00I—Fe01	70.7 (5)	O005—C01B—H01D	109.5
C00S—C00I—H00I	126.3	H01B—C01B—H01C	109.5
C00S—C00I—C00L	107.4 (8)	H01B—C01B—H01D	109.5
C00A—C00J—C00B	123.8 (8)	H01C—C01B—H01D	109.5
Dihedral Angles (º)			
Fe01—C008—C00H—C00L	-58.5 (5)	C00H—C00L—C00N—N007	16.3 (12)
Fe01—C008—C00S—C00I	58.1 (6)	C00I—C00L—C00N—N007	-167.1 (8)
Fe01—C00H—C00L—C00I	-59.1 (6)	C00J—C00A—C00W—C015	7 (2)
Fe01—C00H—C00L—C00N	118.0 (8)	C00J—O00K—C015—C00W	3.7 (19)
Fe01—C00I—C00L—C00H	59.6 (6)	C00L—C00I—C00S—Fe01	60.1 (5)
Fe01—C00I—C00L—C00N	-117.5 (7)	C00L—C00I—C00S—C008	1.9 (10)
Fe01—C00I—C00S—C008	-58.3 (6)	C00M—C00E—C00Y—Fe02	-58.4 (6)
Fe01—C00L—C00N—N007	105.9 (8)	C00M—C00E—C00Y—C00U	0.1 (10)
Fe01—C010—C012—C013	-60.7 (8)	C00O—N009—N00G—C00Z	-169.2 (7)
Fe01—C010—C01A—C016	59.4 (7)	C00O—C00M—C00V—Fe02	-118.5 (7)
Fe01—C012—C013—C016	-59.6 (8)	C00O—C00M—C00V—C00U	-178.4 (7)
Fe01—C013—C016—C01A	-60.8 (7)	C00P—C00R—C00X—Fe02	59.7 (8)
Fe01—C016—C01A—C010	-60.3 (8)	C00P—C00R—C00X—C019	0.5 (13)
Fe02—C00E—C00M—C00O	119.0 (8)	C00P—C017—C019—Fe02	-58.9 (8)

Table A15. Geometric parameters for **Ferfurone** (continuation).

Fe02—C00E—C00M—C00V	-59.7 (5)	C00P—C017—C019—C00X	2.0 (13)
Fe02—C00E—C00Y—C00U	58.5 (6)	C00Q—C00C—O00F—C018	3.4 (13)
Fe02—C00M—C00O—N009	106.3 (8)	C00Q—C00C—C00Z—O00D	172.5 (9)
Fe02—C00M—C00V—C00U	-59.9 (5)	C00Q—C00C—C00Z—N00G	-5.3 (13)
Fe02—C00P—C00R—C00X	-60.5 (8)	C00Q—C014—C018—O00F	2 (2)
Fe02—C00P—C017—C019	59.5 (8)	C00R—C00P—C017—Fe02	-61.1 (7)
Fe02—C00R—C00X—C019	-59.2 (8)	C00R—C00P—C017—C019	-1.6 (12)
Fe02—C00U—C00V—C00M	59.3 (5)	C00R—C00X—C019—Fe02	59.0 (8)
Fe02—C00U—C00Y—C00E	-58.6 (6)	C00R—C00X—C019—C017	-1.5 (13)
Fe02—C00X—C019—C017	-60.5 (8)	C00S—C008—C00H—Fe01	59.6 (7)
Fe02—C017—C019—C00X	61.0 (8)	C00S—C008—C00H—C00L	1.1 (10)
N003—N007—C00N—C00L	179.3 (7)	C00S—C00I—C00L—Fe01	-60.9 (5)
N003—C00B—C00J—C00A	176.3 (9)	C00S—C00I—C00L—C00H	-1.2 (9)
N003—C00B—C00J—O00K	-7.1 (13)	C00S—C00I—C00L—C00N	-178.3 (7)
O004—C00B—C00J—C00A	-3.8 (15)	C00V—C00M—C00O—N009	-166.9 (7)
O004—C00B—C00J—O00K	172.9 (9)	C00V—C00U—C00Y—Fe02	58.7 (6)
N007—N003—C00B—O004	-4.9 (13)	C00V—C00U—C00Y—C00E	0.1 (10)
N007—N003—C00B—C00J	175.0 (7)	C00W—C00A—C00J—C00B	172.9 (10)
C008—C00H—C00L—Fe01	59.2 (6)	C00W—C00A—C00J—O00K	-4.1 (13)
C008—C00H—C00L—C00I	0.1 (9)	C00Y—C00E—C00M—Fe02	59.4 (6)

Table A16. Geometric parameters for **Ferfurone** (conclusion).

C008—C00H—C00L—C00N	177.1 (8)	C00Y—C00E—C00M—C00O	178.4 (8)
N009—N00G—C00Z—C00C	173.2 (7)	C00Y—C00E—C00M—C00V	-0.3 (9)
N009—N00G—C00Z—O00D	-4.5 (13)	C00Y—C00U—C00V—Fe02	-59.7 (6)
C00A—C00J—O00K—C015	0.5 (13)	C00Y—C00U—C00V—C00M	-0.3 (10)
C00A—C00W—C015—O00K	-6 (2)	C00Z—C00C—O00F—C018	-179.0 (10)
C00B—N003—N007—C00N	-169.7 (7)	C00Z—C00C—C00Q—C014	-179.4 (10)
C00B—C00J—O00K—C015	-176.5 (12)	C010—C012—C013—Fe01	60.9 (8)
C00C—O00F—C018—C014	-3.6 (18)	C010—C012—C013—C016	1.3 (13)
C00C—C00Q—C014—C018	-0.4 (17)	C012—C010—C01A—Fe01	-59.8 (8)
C00E—C00M—C00O—N009	14.6 (12)	C012—C010—C01A—C016	-0.4 (13)
C00E—C00M—C00V—Fe02	60.3 (6)	C012—C013—C016—Fe01	59.3 (8)
C00E—C00M—C00V—C00U	0.4 (9)	C012—C013—C016—C01A	-1.5 (13)
O00F—C00C—C00Q—C014	-2.0 (12)	C013—C016—C01A—Fe01	61.5 (8)
O00F—C00C—C00Z—O00D	-4.8 (14)	C013—C016—C01A—C010	1.2 (13)
O00F—C00C—C00Z—N00G	177.5 (8)	C017—C00P—C00R—Fe02	61.2 (7)
N00G—N009—C00O—C00M	179.5 (6)	C017—C00P—C00R—C00X	0.7 (12)
C00H—C008—C00S—Fe01	-59.9 (7)	C01A—C010—C012—Fe01	60.2 (8)
C00H—C008—C00S—C00I	-1.9 (11)	C01A—C010—C012—C013	-0.5 (13)